The evolving velocity field around protostars

PROEFSCHRIFT

ter verkrijging van
de graad van Doctor aan de Universiteit Leiden
op gezag van de Rector Magnificus prof. mr. P. F. van der Heijden
volgens besluit van het College voor Promoties
te verdedigen op woensdag 22 oktober 2008
klokke 16.15 uur

door

Christian Brinch
geboren te Rødovre (Kopenhagen), Denemarken
in 1977

Promotiecommisie

Promotor: Prof. dr. E. F. van Dishoeck

Co-promotor: Dr. M. R. Hogerheijde

Referent: Prof. dr. A. Burkert (Universitäts-Sternwarte München)

Overige leden: Dr. C. P. Dullemond (Max-Planck-Institut für Astronomie)
Prof. dr. F. P. Israel
Prof. dr. K. Kuijken
Prof. dr. H. V. J. Linnartz
Prof. dr. C. Terquem (Institut d´Astrophysique de Paris)

Table of contents

Chapter 1

Introduction

1.1 The birth of stars

On a clear, dark night it is possible to make out a faint nebulosity with the unaided eye in the constellation of Orion. This is the Orion Nebula, part of the giant Orion Molecular Cloud, and it is a vast reservoir of cold molecular gas and interstellar dust. Although the Orion Nebula is the only molecular cloud visible to the naked eye, similar clouds are numerously scattered throughout the Milky Way and some of them are close enough to Earth, so that they can be studied in great detail using telescopes. Stars are known to form inside these clouds and therefore moleclar clouds have been the subject of intense study during the last 30 years, in the pursuit of a complete understanding of the various processes leading from the relatively simple cloud material into a solar-type star, complete with a planetary system, moons, comets and possibly biology.

While the conceptual outline of what is known as low-mass ($\leq 1M_\odot$) star formation is generally well understood, almost every detail about how the initial conditions, i.e. the chemo-physical properties of the local cloud environment, are reflected in the emerging star and planets, if any, are not. At present it is not known why some stars form as doubles or even multiples while others do not. It is also not known why some stars are found to have planetary systems while others seem to have none. There is no doubt that the variation found in stars and their planetary systems are somehow linked to the variation in the molecular clouds out of which they formed. However, it is an open question whether the dependence is predictable or whether the end product of star formation is governed by random (and unpredictable) external effects.

The development of the theory of low-mass star formation began more than 30 years ago. In the early days, the formation of a star was described by an inside-out collapse of a spherical cloud (Shu 1977). As the cloud gets gravitationally unstable, gas and dust start to fall toward the center reaching free-fall speed

Figure 1.1: The star forming region NGC1333 on the edge of the Taurus Molecular Cloud as imaged by the Spitzer Space Telescope at infrared wavelengths. (NASA/JPL-Caltech/R. A. Gutermuth (Harvard-Smithsonian CfA))

and the collapse front expands outward with the local sound speed. This theory, known as the Shu collapse, was not able to treat angular momentum however, as it was spherical symmetric in nature, and therefore no stellar rotation, binary star systems, or disks could be formed. Throughout the 1980's, the collapse theory of Shu was modified to include angular momentum in a series of papers (e.g., Cassen & Moosman 1981; Bodenheimer 1981; Terebey et al. 1984; Lin & Pringle 1990). During the same period, observational evidence for rotational motions in the parental cloud cores were found (Benson & Myers 1989; Goodman et al. 1993) and it became clear that this rotation would lead to the formation of a disk as the centrifugal force would break the spherical symmetry. Eventually, all the cloud material ends up in either the star or the disk (disregarding winds and jets which are still not well understood), which would now be in stable Keplerian rotation. At present, no analytical model exists which can reproduce this entire scenario, but numerical simulations have been successful in producing disks out of collapsing rotating clouds (e.g., Boss 1993; Burkert et al. 1997; Yorke & Bodenheimer 1999).

On the observational side, young stellar objects were found to have different

a	b	c	d
$\tau=0\,$yr 1 pc	$\tau\simeq10^4\,$yr 10^4AU	$\tau\simeq10^5\,$yr 10^3AU	$\tau\simeq10^6\,$yr 10^2AU
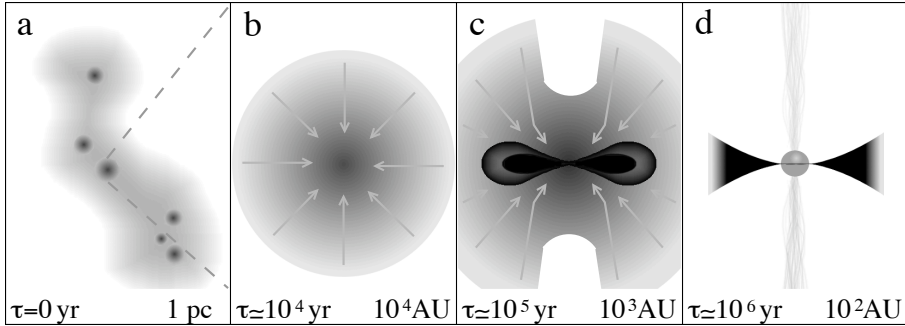
Figure 1.2: A cartoon depiction of the stages of low-mass star formation. **a)** An inhomogenous molecular cloud with several overdense regions, so called cloud cores. **b)** A cloud core is triggered into gravitational collapse when it reaches its Jeans mass. Material moves radially toward the center of the core under the influence of gravity. **c)** Due to turbulence and shear motions of the molecular cloud, the core has a net angular momentum which makes the material spin up as the core contracts. The result is a rotating disk of material onto which material is accreted from the still collapsing molecular envelope. **d)** A T Tauri star emerges when all of the envelope has either been accreted or blown away by the bipolar outflow that characterizes these objects. The remaining material is located in a protoplanetary disk.

spectral energy distributions. Indeed, Lada & Wilking (1984) showed that the slope of the distribution between 10 μm and 20 μm would divide a sample of protostars into two distinct categories giving rise to the Class I/II/III classification scheme. Later on, a Class 0 was added by André et al. (1993) for protostars with a strong far-infrared excess. The interpretation of this classification is that the more infrared excess a star shows, the more embedded in dust it is. Class 0 stars are therefore thought to be deeply embedded protostars, shown as panel b in Fig. 1.2, the Class I stars less embedded (panel c, Fig. 1.2), and Class II stars unobscured T Tauri stars as shown in panel d, Fig. 1.2. As suggested by Fig. 1.2, these classes represent a linear time evolution, going from Class 0 to Class II over time. Whether this is really true or not and whether all stellar spectral energy distributions will appear in all three classes over time is not clear. It is also not well-understood if these classes really represent physically distinct populations or whether there is an overlap.

The long time scales on which star formation takes place ($> 10^6$ years) make

it impossible to follow a single star through the various stages of the formation process. Indeed, in almost all circumstances, any given young star will be seen as a snapshot representing its present evolutionary stage, even throughout the entire life of an astronomer. However, by observing a number of young stars on different evolutionary stages, a chronological sequence can be pieced together. If young stars can be placed reliably in an evolutionary sequence, various physical properties, such as dust grain sizes, chemical abundances, etc., can be followed in time and the influence of the cloud environment can be followed throughout the entire star formation process.

The challenging part is to disentangle evolutionary differences between a number of objects from intrinsic differences because of the degeneracies between the two. An example of this is the stellar mass. One could think of using the stellar mass as tracer of evolution, assuming that the mass of the star grows during its formation. In that case a more massive star would be considered a more evolved star than a less massive one. However, stars end up with a wide range in masses and therefore the more massive star could simply be an intrinsically more massive star at the same evolutionary stage as one which is intrinsically less massive.

Consequently, a lot of research in the field of low-mass star formation is concerned with finding reliable tracers of evolution (basically a tracer of the age of an object, although the time scale is almost certainly an object dependent variable itself). Attempts are made to use the ongoing chemistry as a tracer of evolution. Charnley et al. (1992) have suggested to use abundance ratios, whereas Jørgensen et al. (2004) use the abundance profiles, as a "chemical clock". Various attempts are also made to constrain the classification scheme of Lada & Wilking (1984) with better time-scale estimates (e.g., Adams et al. 1987; André & Montmerle 1994; Allen et al. 2004; Luhman et al. 2008). This thesis revolves around the topic of low-mass protostellar evolution with special emphasis on the feasibility of using the gas kinematics as a tracer of evolution.

1.2 The study of molecular emission lines

The gas-phase molecular material which is present in protostellar environments is the main diagnostic tool used in this thesis. It is typically observed in the (sub)millimeter regime of the electromagnetic spectrum, because the conditions of the circum-(proto)stellar environment are such that material located there will radiate at those frequencies (10-1000 GHz). In particular, we study emission associated with rotational transitions since the rotational bands are dominant at temperatures between 10 and 100 K, typical for the gas surrounding protostars. We

study molecular line emission rather than thermal continuum radiation, associated with the dust grains, because the motion of the gas is directly reflected in the line position through the velocity induced Doppler shift. Hence, by studying emission lines, we can derive information about the velocity field around protostars.

1.2.1 Line formation

Line emission is the result of spontaneous or induced de-excitation of a molecule according to the famous relation

$$h\nu = E_1 - E_2. \tag{1.1}$$

The energy eigenstates E_i are molecule dependent and the allowed transitions between states are described by selection rules, resulting in a unique set of possible photon frequencies for each molecular species. The reverse process, excitation of energy states, depends on the physical environment, in particular the temperature and density, which thus controls the relative population of the energy levels E_i. The emergence of a line spectrum occurs when the photons from an ensemble of molecules, which are being continuously excited and de-excited, are measured over a period of time.

Although Eq. 1.1 suggests that the transition occurs at a single well-defined frequency, every transition in general results in a spread of the emission over a range of frequencies. Several mechanisms can cause this so-called line broadening, of which the most fundamental is called natural line broadening. This effect is due to the quantum mechanical uncertainty relation that allows variation in the transition energy given a sufficiently well-defined period of time. For rotational transitions, this effect is small however, compared to the Doppler broadening which is a temperature dependent effect. The motion of the molecule relative to the observer causes a Doppler shift of the line center, proportional to the velocity difference between the molecule and the observer. In a gas consisting of many molecules, the velocities are given by a Maxwellian velocity distribution resulting in a continuous line center shift over the corresponding velocities. When adding the contribution of all molecules along the line of sight, this results in a continuous Gaussian line profile.

Under interstellar conditions, where temperatures typically are relatively low (< 100 K), the thermal Doppler broadening has a small effect on the spectral line width ($\sim$0.1 km s^{-1} for CO at 10 K). If however, a systematic velocity field is present in the emitting medium, a non-thermal Doppler broadening occurs, which can be substantial. The exact shape of the resulting line profile depends on the

composition of the velocity field and it is this effect that we rely on, when we characterize the motion of the circumstellar material using spectral line profiles. Figure 1.3 shows an illustration of how different line profiles result from different velocity fields. The figure shows a protostellar envelope with an inner region with a high excitation temperature and an outer region with a low excitation temperature. The velocity vectors show the direction of the flow as well as the projected line-of-sight velocity. Two dashed ovals are also plotted in the figure. These ovals are loci of constant projected velocity, so that at the two points where the line-of-sight intersects these loci the projected velocity is the same. The bulk of the emission originates from the high excitation temperature region. This is true for both the red-shifted and blue-shifted side. In the infall case (panel a), however, only the red-shifted emission passes through the locus intersection in the low excitation temperature region, where part of the emission is absorbed. In the case of pure rotation (panel b), the red-shifted and blue-shifted sides are equally absorbed.

1.2.2   Modeling of line profiles

When observing an emission line of interstellar origin, the line will in most cases originate from a large number of molecules (i.e., a cloud of gas) which is distributed over a range in densities and temperature. Moreover, the distribution is in general not homogenous, resulting in a variation of the relative abundance over the region being studied. This makes forward solving of the physical structure of the cloud impossible. Instead, a physical model is adopted and the radiation field escaping the model cloud is predicted, from which a model line spectrum can be calculated. This line model can then be compared to the measured line, and in case of a good match, the adopted model is likely to give a good description of the cloud.

In a cloud of gas, a photon emitted from a decaying state of one molecule can either escape the cloud and contribute to the emission line or, depending on the optical depth, excite the same state of another molecule on its way toward the cloud surface. In the latter case, the newly excited molecule decays after a while and the photon is reemitted in a random direction and can possibly excite another molecule again. The more molecules that exist in the excited state, the smaller the chance of the photon getting absorbed on its way out. However, the chance of a radiative de-excitation is increased, which will thus lower the number of excited molecules and increase the number of absorptions again.

This coupled dependency between the radiation field and the level excitation makes the problem of predicting the emerging emission line difficult and it needs to be solved iteratively. The emission and absorption probabilities does not just
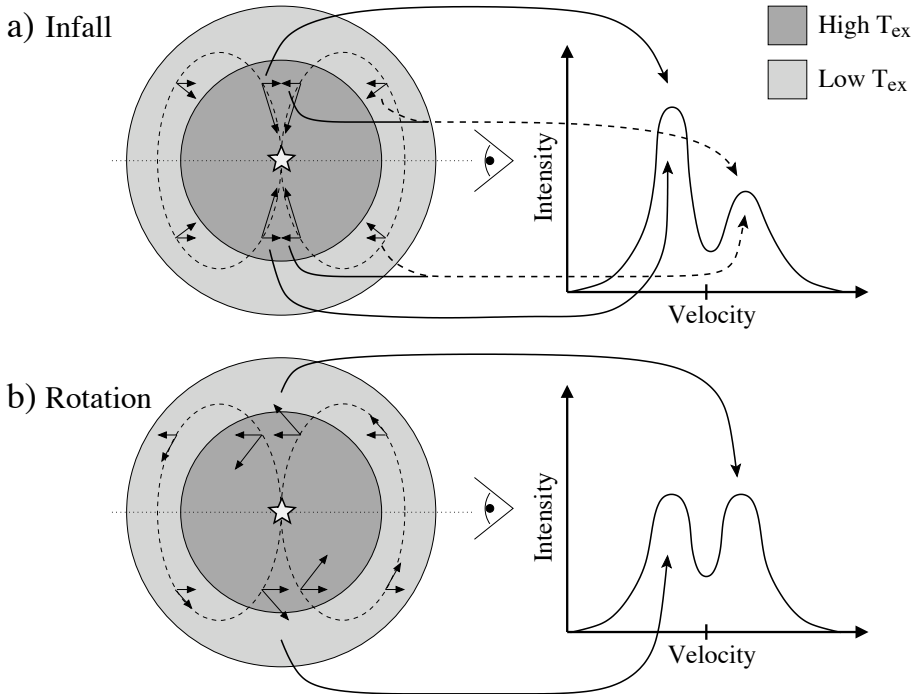
Figure 1.3: A schematic depiction of the influence of the velocity field in a gaseous envelope on the line profile. The dashed ovals are loci of constant projected velocity. Any line of sight will intersect these loci at two different excitation temperatures T_{ex}. In panel **a)**, blue-shifted emission from the high T_{ex} region travels unobscured toward the observer, while red-shifted emission from the high T_{ex} region is obscured by the material with the same velocity in the low T_{ex} region. In panel **b)**, both the red and the blue sides are equally affected. Figure inspired by Zhou & Evans (1994).

depend on the level populations, but also on the local temperature and density which adds to the complexity of the computational task. Furthermore, the velocity field, which causes a Doppler shift of the photons, ensures that only molecules with a small relative velocity can interact through an exchange of photons. Obviously, this cannot be solved analytically except for the simplest cases and therefore radiation transfer codes are employed to make predictions of the emission lines. In this thesis we make extensive use of one such code, known as *RATRAN* (Hogerheijde & van der Tak 2000), but we have also developed our own code, which we

present in a later chapter.

In order to reach a match between the observed lines and the lines predicted by the model, several adjustable parameters are included. Most of these can be constrained by other observables than emission lines; for example, the temperature and density profiles are fixed from measurements of the dust continuum brightness profiles at different frequencies. The velocity field however, is only constrainable through comparison of spectral lines, because these are the only observables which directly reflect the velocity of the emitting medium. Throughout this thesis we use a two dimensional parameterization of the velocity field,

$$\mathbf{v} = \begin{pmatrix} v_r \\ v_\phi \end{pmatrix} = \sqrt{\frac{GM_*}{r}} \begin{pmatrix} -\sqrt{2}\sin\alpha \\ \cos\alpha \end{pmatrix}, \tag{1.2}$$

where the two free parameters M_* and α represent the protostellar mass and the ratio of infall speed to rotation speed, respectively. These two numbers describe the velocity field and, as we show in a later chapter, they can be used to characterize the evolutionary state of a protostellar object. This parameterization gives us a smooth transition from pure infall to pure rotation and we can therefore use it to determine when an object is dominated by one or the other.

1.2.3 Submillimeter observations

Our primary diagnostic tool is formed by the emission lines associated with rotational transitions of various molecular species and these bands lie in the radio wave part of the electromagnetic spectrum. Radio telescopes are used to measure these frequencies and in this thesis, we use a variety of such observations.

As with all telescopes, the spatial resolution of radio wave observations is proportional to the wavelength and inversely proportional to the telescope dish diameter. Because radio waves lie in the low-frequency (long wavelength) domain of the electromagnetic spectrum, the telescopes have to be huge in order to reach a decent angular resolution. However, the dish surface smoothness has to be of the order of a fraction of the wavelength, which, for submillimeter observations, therefore requires very smooth surfaces. One of the biggest telescopes that fulfill this criterion is the James Clerk Maxwell Telescope in Hawaii with a mirror diameter of 15 meters. This telescope is able to observe most low-J rotational transitions between 0.5 mm and 1.0 mm at a resolution of $10''$–$20''$, depending on the wavelength. At this resolution, young stellar objects, at a typical distance of the order of 100 pc, are only marginally resolved if resolved at all. The fact that the sources are not well resolved, however, can be useful to us in some cases.

Because our velocity model (Eq. 1.2) has no spatial dependency, it is suited to fit observations where the velocity field has been spatially averaged in a large beam that covers the entire object. Studying objects in more detail, however, require observations of much higher resolution and this is needed when we investigate the velocity field on disk scales.

In order to achieve higher resolution we need to do interferometric observations rather than the more traditional single-dish observations. The technique is to link several telescopes together and letting the signal from each antenna interfere with the signal from each of the other antennas, while measuring the phase and amplitude of the interference. Interferometry becomes increasingly difficult going toward higher frequencies because the wavelength becomes small and hence better timing accuracy is needed. In the last ten years several millimeter interferometry facilities have become operational around the world, but, only one of them, the Submillimeter Array in Hawaii, operates at shorter wavelengths than 1mm. For this thesis, interferometric data have been obtained from the Submillimeter Array. Images can be reconstructed with a resolution that is an order of magnitude higher than the best obtainable single-dish resolution. With the increased resolution, we are not only able to probe the velocity field in distinct regions of an object, but we can also constrain global properties such as the shape of the gaseous envelope, system inclination, etc. The interferometric observations are very well complimented by the single-dish observations, because by using both types of observations to constrain the models simultaneously, we make sure that our model is consistent with the data on all probed spatial scales.

1.3 Thesis outline

A comprehensive study of the young stellar object L1489 IRS is presented in **chapter 2**. In this chapter we introduce several of the tools and techniques which we employ throughout this thesis. We take a physical model from the literature of L1489 IRS, which we customize so that we can accommodate observational features such as the envelope geometry and we introduce a parameterized description of the velocity field. The reason why we study this particular object is because of its unusual properties. First of all it has a very large size and an elongated disk-like appearance. Secondly, both infall and rotational velocity components are measured, and therefore this source is a good candidate for testing our velocity model. Our model is compared to single-dish spectra and because we have a large number of free parameters, we use a stochastic search algorithm to obtain the best fit. The minimization technique used in this chapter is based on Voronoi

tessellation of the parameter space. In **chapter 3** we use a similar, but more advanced search algorithm, whereas the Voronoi tessellation is revisited in **chapter 7**, this time as a mean of radiation transfer gridding.

Our velocity model is elaborated upon in **chapter 3**. The scope of this chapter is to evaluate general applicability of the velocity model and to test how well the best fit parameters of our model describe the actual velocity field of a particular source. A hydrodynamical simulation of the formation of a star and a circumstellar disk provides a continuous velocity field, temperature and density distribution. Synthetic observations are then calculated from our hydrodynamical solution and the velocity model which was introduced in **chapter 2** is fitted to these in a similar way as we did for L1489 IRS. We show that the best-fit parameters describe a velocity field which is in reasonable agreement with the velocity field in the simulation. In this chapter we use a genetic optimization algorithm to obtain the best fit. This algorithm proves to be very reliable and works well for our purpose.

In **chapter 4** we return to L1489 IRS, for a more detailed study. High-resolution interferometric data were acquired with the Submillimeter Array of the central, dense parts of this source. The aim of this chapter is to investigate whether it is possible to separate a possible protoplanetary disk from the envelope using kinematic arguments. We use the model derived in **chapter 2** but with the addition of a Keplerian disk model on scales smaller than 300 AU. The submillimeter data are consistent with such a model, but cannot constrain any disk properties. Simultaneous modeling of the mid-infrared fluxes from the Spitzer Space Telescope complements the submillimeter data well, however, and with these data, additional constraints strongly support the disk model.

Until this point, variations in the molecular abundance distribution have been disregarded. However, chemical depletion, which is known to exist in protostellar environments, may mask out kinematically distinct regions, in which case our velocity model gives a false result. **Chapter 5** contains a treatment of the CO depletion in the circumstellar disk and envelope. We use the same hydrodynamical simulation as used in **chapter 3** to describe the star formation and we populate the simulation with molecules that can freeze-out and desorb according to the physical environment. The resulting abundance patterns are used to calculate synthetic CO spectra. We show that the importance of taking chemical depletion into account is most important for young sources and less important for more evolved objects. Also optically thin lines are significantly more affected than their optically thick counterparts.

In **chapter 6** we employ all techniques used so far in this thesis, by modeling both single-dish and interferometric submillimeter data of the young protostel-

lar source NGC1333–IRAS2A, a source in which depletion is significant. Again we use our parameterized velocity model together with a literature model of the physical and chemical structure. Our result confirms that this is indeed a young source, by favoring a solution with a low central mass and strong infall motions (very little rotation). A particularly puzzling result is that no kinematic evidence for Keplerian rotation on 100 AU scales is found, despite the evidence for the presence of a mass condensation on these scales from the dust continuum data. This makes IRAS2A a very different kind of object, compared to L1489 IRS, from a kinematical point of view.

The last part of this thesis, **chapter 7**, is a presentation of a new radiation transfer code, based on the work of Ritzerveld & Icke (2006), which we have developed in parallel to the research presented in the previous chapters. This code is designed to improve on several shortcomings of the radiation transfer code used so far, by changing the gridding and transport algorithms fundamentally. A new gridding subroutine based on Voronoi tessellation of the model is implemented, making the code truly three dimensional, very fast, and able to resolve a much wider range of scales.

1.4 Conclusions

Several conclusions can be drawn from this thesis. We will here briefly summarize the main conclusions, not necessarily in the order in which they appear in the following chapters.

- The velocity field transits smoothly from infall to rotation during a gravitational collapse and the formation of a circumstellar disk. The velocity field can be characterized uniquely by the model parameters α and M_*.

- The mass of the protostar is highly object dependent. However, the ratio of protostellar mass to envelope mass M_*/M_{env} is likely to be the same for all low-mass stars at any given fraction of their total formation time. Along with the α parameter, this ratio traces time evolution and can be used to order objects into an evolutionary sequence.

- Depletion occurs in the envelope, especially in the early stages of the collapse. Later on depletion becomes significant in the protoplanetary disk. It is important to model depletion as it may affect the appearance of the velocity field in the spectral lines.

- If depletion is modeled properly, it may provide a way to calibrate the evolution sequence of M_* and α with an absolute time scale. This would effectively give us a kinematical clock of evolution.

- Circumstellar disks seem to form almost immediately after the initial collapse of the prestellar core. Whether or not it is reasonable to use the word disk at the very earliest point is questionable, since the rotation pattern only shows up at somewhat later stages of the collapse.

- While high-resolution observations, provided by interferometers, reveal an enormous amount of detail, it is actually preferable to combine both high and low resolution observations in order to pin down the velocity field. α is by definition an average of the ratio of infall to rotation, and the spatial averaging in the large beam of single-dish telescopes gives a good boundary condition, when fitting the velocity field.

- The geometrical properties of disks are better constrained by near-infrared imaging and mid-infrared spectroscopy due to the improved resolution and its high sensitivity to the dust column along the line of sight. While infrared continuum emission does not reveal anything about the velocity field, it can fix a number of parameters which are hard to constrain using submillimeter radiation. Furthermore, it is important that the models are consistent with the emission in all frequency bands and not just in one particular part of the spectrum.

- Often, young stellar objects are described in a very idealized way; completely spherical or axi-symmetric. L1489 IRS is evidence of that this is not always the case. Envelopes may be elongated, asymmetric, warped, and the same is true for the disks. The angular momentum of disk and envelope may not be well aligned either. These asymmetries are likely caused by stellar binarity and interactions with the local environment, such as neighboring clouds and outflows from other protostars.

- As angular resolution is improved by bigger and better telescopes, structural details in young stellar objects are revealed, which cannot be modeled with existing two dimensional radiation transfer codes. However, alongside the development of flexible high dimensional radiation transfer codes, physical models need to be improved as well in order to describe these details.

References

Adams, F. C., Lada, C. J., & Shu, F. H. 1987, ApJ, 312, 788

Allen, L. E., Calvet, N., D'Alessio, P., et al. 2004, ApJS, 154, 363

André, P. & Montmerle, T. 1994, ApJ, 420, 837

André, P., Ward-Thompson, D., & Barsony, M. 1993, ApJ, 406, 122

Benson, P. J. & Myers, P. C. 1989, ApJS, 71, 89

Bodenheimer, P. 1981, in IAU Symposium, Vol. 93, Fundamental Problems in the Theory of Stellar Evolution, ed. D. Sugimoto, D. Q. Lamb, & D. N. Schramm, 5–24

Boss, A. P. 1993, ApJ, 417, 351

Burkert, A., Bate, M. R., & Bodenheimer, P. 1997, MNRAS, 289, 497

Cassen, P. & Moosman, A. 1981, Icarus, 48, 353

Charnley, S. B., Tielens, A. G. G. M., & Millar, T. J. 1992, ApJ, 399, L71

Goodman, A. A., Benson, P. J., Fuller, G. A., & Myers, P. C. 1993, ApJ, 406, 528

Hogerheijde, M. R. & van der Tak, F. F. S. 2000, A&A, 362, 697

Jørgensen, J. K., Schöier, F. L., & van Dishoeck, E. F. 2004, A&A, 416, 603

Lada, C. J. & Wilking, B. A. 1984, ApJ, 287, 610

Lin, D. N. C. & Pringle, J. E. 1990, ApJ, 358, 515

Luhman, K. L., Allen, L. E., Allen, P. R., et al. 2008, ApJ, 675, 1375

Ritzerveld, J. & Icke, V. 2006, Phys. Rev. E, 74, 026704

Shu, F. H. 1977, ApJ, 214, 488

Terebey, S., Shu, F. H., & Cassen, P. 1984, ApJ, 286, 529

Yorke, H. W. & Bodenheimer, P. 1999, ApJ, 525, 330

Zhou, S. & Evans, II, N. J. 1994, in Astronomical Society of the Pacific Conference Series, Vol. 65, Clouds, Cores, and Low Mass Stars, ed. D. P. Clemens & R. Barvainis, 183

Chapter 2

Structure and dynamics of the Class I young stellar object L1489 IRS

Abstract

During protostellar collapse, conservation of angular momentum leads to the formation of an accretion disk. Little is known observationally about how and when the velocity field around the protostar shifts from infall-dominated to rotation-dominated. We investigate this transition in the low-mass protostar L1489 IRS, which is known to be embedded in a flattened, disk-like structure that shows both infall and rotation. We aim to accurately characterize the structure and composition of the envelope and its velocity field, and find clues to its nature. We construct a model for L1489 IRS consisting of an flattened envelope and a velocity field that can vary from pure infall to pure rotation. We obtain best-fit parameters by comparison to 24 molecular transitions from the literature, and using a molecular excitation code and a Voronoi optimization algorithm. We test the model against existing millimeter interferometric observations, near-infrared scattered light imaging, and ^{12}CO ro-vibrational lines. We find that L1489 IRS is well described by a central stellar mass of 1.3 ± 0.4 $M_\odot$ surrounded by a 0.10 $M_\odot$ flattened envelope with approximate scale height $h \approx 0.57R$, inclined at $74°^{+16°}_{-17°}$. The velocity field is strongly dominated by rotation, with the velocity vector making an angle of $15° \pm 6°$ with the azimuthal direction. Reproducing low-excitation transitions requires that the emission and absorption by the starless core $1'$ (8400 AU) east of L1489 IRS is included properly, implying that L1489 IRS is located partially behind this core. We speculate that L1489 IRS was originally formed closer to the center of this core, but has migrated to its current position over the past few times 10^5 years, consistent with their radial velocity difference of 0.4 km s^{-1}. This suggests that L1489 IRS' unusual appearance may be result of its migration, and that it would appear as a 'normal' embedded protostar if it were still surrounded by an extended cloud core. Conversely, we hypothesize that the inner envelopes of embedded protostars resemble the rotating structure seen around L1489 IRS.

Christian Brinch, Antonio Crapsi, Michiel R. Hogerheijde, and Jes K. Jørgensen

2.1   Introduction

The last three decades has provided a detailed understanding of the process of low-mass star formation through theoretical work and advancements in the observational facilities (see for example the review by André et al. 2000; or several reviews in Reipurth et al. 2007). These achievements have given us a detailed view on infant stars through their various stages of formation. Low-mass stars form out of dark molecular clouds when dense regions can collapse under the influence of their own gravity. When sufficient density is reached, a protostellar object is formed, still deeply embedded in a surrounding envelope. Conservation of angular momentum leads to the formation of a disk around the protostar onto which the surrounding dust and gas is accreted, although little details are known of how exactly disks grow. As the stellar wind starts to clear out the envelope, the star and the disk becomes visible in the optical and infrared and the object enters the classical T Tauri stage which then later evolves into a main sequence star (Shu 1977; Lizano & Shu 1989; Adams et al. 1988). Most observed young stellar objects (YSOs) are usually classified based on the shape of their spectral energy distribution (SED) as either a Class I, II, or III (Lada & Wilking 1984). Class I objects are deeply embedded in dense cores, while Class II objects are surrounded by actively accreting disks. Class III objects have little material left in a disk, but are still descending to the main sequence. Sometimes, however, a YSO does not clearly fit into one of these categories. Those objects are most likely the ones that can shed light on some of the missing pieces of the picture. In this chapter we study one such transitional object, L1489 IRS, and investigate the structure, dynamics, and composition of its circumstellar material.

L1489 IRS (IRAS 04016+2610) is classified as a Class I object based on its SED and visibility at near-infrared wavelengths (Myers et al. 1987). Like many embedded YSOs, line profiles of dense gas tracers like HCO^+ J=3–2 and 4–3 show red-shifted absorption dips usually interpreted as indications of inward motions in the envelopes (Gregersen & Evans 2000; Mardones et al. 1997). However, Hogerheijde (2001) shows that the spatially resolved HCO^+ J=1–0 emission exhibits a flattened, 2000 AU radius structure dominated by Keplerian rotation. In this aspect, L1489 IRS more closely resembles a T Tauri star with a circumstellar disk (Koerner & Sargent 1995; Guilloteau & Dutrey 1998; Simon et al. 2000). T Tauri disks, however, are in general much smaller than the disk structure seen in L1489 IRS with radii of several hundreds of AU. Scattered light imaging by Padgett et al. (1999) shows the central stellar object and the presence of a slightly flaring dark lane, consistent with the disk-like configuration inferred from the HCO^+ J=1–0 observations. Careful analysis of the circumstellar velocity field

by Hogerheijde (2001) revealed that infalling motions are present at $\sim 10\%$ of the Keplerian velocities. Hogerheijde hypothesized that L1489 IRS is in a short-lived transitional stage between a collapsing envelope (Class I) and a rotationally supported, Keplerian disk that may be viscously evolving (Class II). Observations of ro-vibrational CO absorption lines at 4.7μm showed that the inward motions continue to within 1 AU from the central star (Boogert et al. 2002).

In this chapter we address a number of questions about L1489 IRS. We construct a model for the circumstellar structure that accommodates *all* available observations, ranging from an extensive set of single-dish molecular line measurements to the interferometric observations, the scattered light imaging, and the CO ro-vibrational absorption lines. Hogerheijde (2001) adopted a flared disk model with a fixed scale height for the structure inspired by the interferometric imaging. In this chapter we choose a description for the circumstellar structure that can be smoothly varied from spherical to highly flattened, and investigate if the full data set requires a disk-like configuration. In this chapter we also introduce a velocity field that can range from purely Keplerian to completely free-fall, or any combination of the two. By considering the full data set, stronger constraints can be set on the velocity field and the dynamical state of L1489 IRS than possible before. We perform a rigorous optimization of the model for L1489 IRS using all available single-dish line data, and test the model by comparing the interferometric observations, the scattered light imaging, and the CO ro-vibrational absorption lines to predictions from the model. Once we have established a satisfactory model, also taking into account the immediate cloud environment, we explore the nature of L1489 IRS. Does it represent a transitional state between Class I and II? Do all YSOs go through this stage? Or is L1489 IRS in some way special?

2.2   Observations and model description

2.2.1   Single-dish observations

The primary data set on L1489 IRS used in this chapter was published by Hogerheijde et al. (1997) and Jørgensen et al. (2004), and consists of 24 transitions among 12 molecular species. Figure 2.1 shows all 24 spectra. Table 2.1 lists the transitions, integrated line strengths, line widths, and relevant beam sizes of the single-dish telescopes. In all cases, line intensities are on the main-beam antenna temperature scale, using the appropriate beam efficiencies. The integrated intensities are obtained by fitting a Gaussian to the line. In some cases, no lines are visible above the noise level, and 3σ upper limits are given. The signal-to-noise ratio

of the HNC J=4–3 and H_2CO J=5_{15}–4_{14} spectra were insufficient for a proper Gaussian fit; instead the spectra are simply integrated from −4 to +4 km s^{-1} with respect to the systemic velocity of +7.2 km s^{-1}. In addition to these molecular line data, we also use the total mass derived from the 850 μm continuum observations by JCMT/SCUBA (Hogerheijde & Sandell 2000).

Apart from the single dish data which we use for the model optimization, we compare predictions by the model to other previously published observations: a HCO$^+$ J=1–0 interferometer map from the BIMA and OVRO arrays (Hogerheijde et al. 1998), CO ro-vibrational absorption spectra from the Keck Telescope (Boogert et al. 2002), and the near-infrared scattered light imaging from HST/NICMOS (Padgett et al. 1999).

2.2.2   The model

Previous studies of L1489 IRS clearly indicate that a non-spherical axis-symmetric description of its circumstellar structure is required. In the following subsections we construct a description of the density $n(r, \theta)$, gas temperature $T(r, \theta)$, and velocity field $\mathbf{v}(r, \theta)$=(v_R, v_z, v_ϕ). Throughout we attempt to keep the number of free parameters at a minimum. In the end we arrive at four free parameters, in addition to the eight molecular abundances which we fit but assume constant throughout the source, and seven parameters that we hold fixed (Table 2.2).

Density

We adopt an axi-symmetric description of the gas density $n(r, \theta)$ consistent with the spherical model from Jørgensen et al. (2002). These authors deduce a total mass of 0.097 $M_\odot$ and a density following a radial power law with slope −1.8 between radii of 7.8 and 9360 AU. We truncate this model at the observed outer radius of L1489 IRS of 2000 AU, but keep the power-law slope and mass conserved. Instead of a simple radial power law, $n \propto r^{-p}$ with $p = 1.8$, we adopt a Plummer-like profile, $n \propto [1+(r/r_0)^2]^{-p/2}$ with r_0=4.0 AU. This description keeps the density finite at all radii, but since r_0 is much smaller than the scales of interest here, the resulting density distribution is identical to that used by Jørgensen et al. (2002).

From this spherically symmetric density distribution we construct an axi-symmetric, flattened configuration by multiplying by a factor $\sin^f \theta$, where f can take any value ≥ 0 (see Stamatellos et al. 2004, where this approach was used for

Table 2.1: Single-dish molecular line data set

Molecule	Transition	$\int T_{mb} dv$ (K km s^{-1})	FWHM (km s^{-1})	Beam ($''$)
C^{17}O	1–0	0.5^a ± 0.04	2.9	22
	2–1	1.2^a ± 0.03	2.6	11
	3–2	0.7 ± 0.1	2.7	15
C^{18}O	1–0	1.8 ± 0.04	1.1	34
	2–1	2.8 ± 0.1	1.6	23
	3–2	3.4 ± 0.1	2.5	15
HCO$^+$	1–0	6.7 ± 0.2	2.1	28
	3–2	6.9 ± 0.2	2.2	19
	4–3	10.0 ± 0.3	2.5	14
H^{13}CO$^+$	1–0	0.8 ± 0.1	0.8	43
	3–2	0.8 ± 0.1	1.8	19
H$_2$CO	5_{15}–4_{14}	0.61 ± 0.07	4.0	14
CS	2–1	1.2 ± 0.02	0.9	38
	5–4	0.6 ± 0.04	0.8	22
	7–6	0.7 ± 0.1	3.6	15
C^{34}S	2–1	<0.3^b	–	39
	5–4	<0.3^b	–	21
HCN	1–0	2.4^a ± 0.1	2.3	43
	4–3	1.3 ± 0.1	5.8	14
H^{13}CN	1–0	<0.5^b	–	44
CN	1_{023}–0_{012}	0.63 ± 0.12	–	33
	3–2	0.67^a ± 0.09	3.9	15
HNC	4–3	1.5 ± 0.3	6.4	14
SO	2_3–1_2	0.3 ± 0.03	0.8	38

^{a} Intensity integrated over multiple hyperfine components.
^{b} No line detected. 3σ upper limit, based on an assumed line width of 1.5 km s^{-1}.
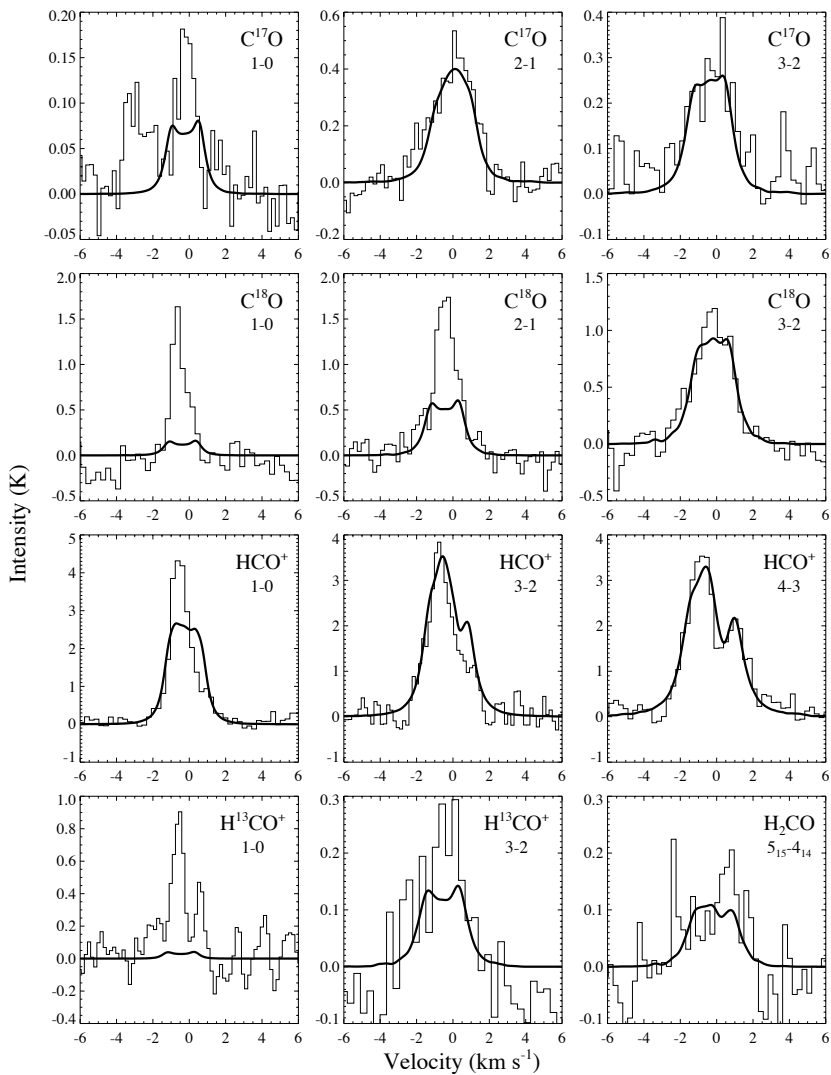The error bars on the intensity does not include the 20% calibration error.

Figure 2.1: The 24 single-dish molecular line spectra used for the model optimization (histograms). The solid lines show the best-fit results for the model of L1489 IRS (See also following page and Fig. 2.5).
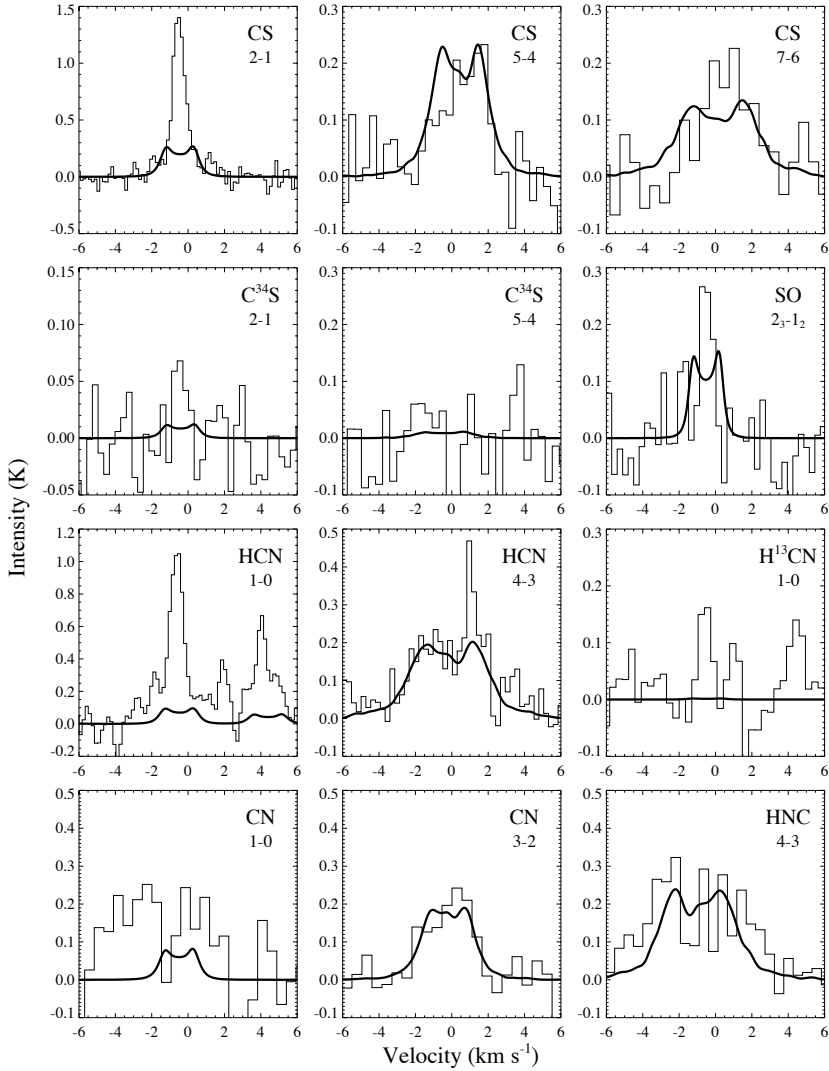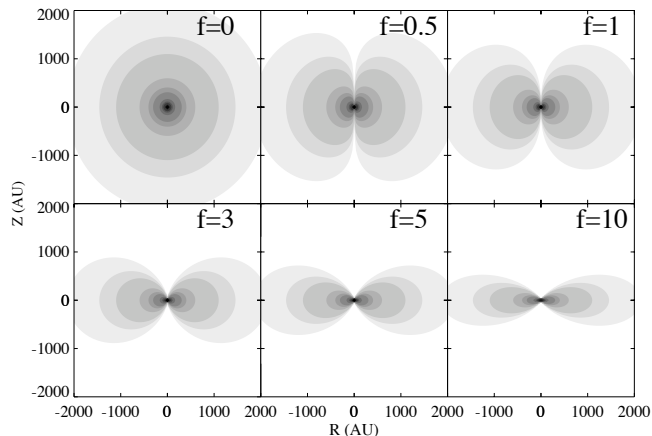
Figure 2.1: Cont'd.

Figure 2.2: Progression of flattening of the adopted density structure as f is increased from 0 (purely spherical) to 10 in Eq. (2.1).

modeling starless cores). The adopted density distribution now becomes,

$$n(r, \theta) = n_0 \left(1 + \left(\frac{r}{r_0} \right)^2 \right)^{-p/2} \sin^f \theta. \qquad (2.1)$$

For $f = 0$, this reduces to a spherically symmetric structure, while for $f > 10$ the resulting profiles becomes largely indistinguishable as the sine term in Eq. 2.1 approaches a step function (Fig. 2.2). The mass contained in the structure is kept constant at 0.097 $M_\odot$ by adjusting n_0 as f is varied. The only free parameter in the density description is the flattening parameter f.

Temperature

The temperature of the gas and the dust (which we assume to be identical) in the circumstellar structure of L1489 IRS is dependent on the stellar luminosity which is ~3.7 $L_\odot$ (Kenyon et al. 1993a) and the infrared radiative transfer through the structure. Since most of the circumstellar material is optically thin to far-infrared radiation, the deviations introduced by the flattening on the temperature structure are minor. Furthermore, the line excitation does not depend strongly on small temperature differences. A spherically symmetric description of the temperature therefore suffices. Using the continuum radiation transfer code *DUSTY* (Nenkova

et al. 1999) and the density structure of Eq. (2.1) with $p = 1.8$ and $f = 0$, we find that the temperature is well described by,

$$T(r) = 19.42 \, \text{K} \left(\frac{r}{1000 \, \text{AU}} \right)^{-0.35}. \tag{2.2}$$

There are no free parameters in this description of the temperature.

Velocity field

The velocity field is parameterized by a central, stellar mass $M_\star$ and an angle α in such a way that,

$$v_r = -\sqrt{2} \sqrt{\frac{GM_\star}{r}} \sin \alpha, \tag{2.3}$$

$$v_\phi = \sqrt{\frac{GM_\star}{r}} \cos \alpha. \tag{2.4}$$

For $\alpha = 0$ this reduces to pure Keplerian rotation around a mass $M_\star$ without any inward motions; for $\alpha = \frac{\pi}{2}$ the velocity field is that of free fall toward a mass $M_\star$. Intermediate values of α produce a velocity field where material spirals inward. The implicit assumption in this description is that both components of the velocity field vary inversely proportional with $\sqrt{r}$.

In this description there are two free parameters, the stellar mass $M_\star$ and the angle α which is kept constant with radius. In addition to this ordered velocity field, we add a turbulent velocity field with FWHM 0.2 km s^{-1}.

2.2.3 Molecular excitation and line radiative transfer

The excitation of the molecules and the line radiative transfer is calculated using the accelerated Monte Carlo code *RATRAN* (Hogerheijde & van der Tak 2000). Collisional excitation rates are taken from the Leiden Atomic and Molecular Database *LAMDA* (Schöier et al. 2005). We lay out the model onto three nested 8×6 grids (Fig. 2.3). The innermost grid cell is subdivided four times, so that the innermost cell is resolved down to 4 AU. All properties are calculated as cell averages, by numerically integration over the cell and divided by its volume. To reduce computing time, cells with H$_2$ densities below 10^3 cm^{-3} are dropped. Such cells do not contribute significantly to the line emission or absorption. Dust continuum emission is included through a standard gas-to-dust ratio of 100:1 and dust emissivity from Ossenkopf & Henning (1994) for thin ice mantles which has been accreted and coagulated for about 10^5 years.
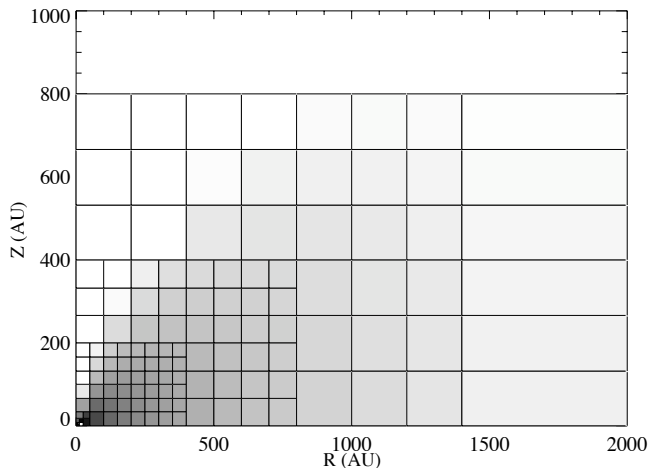
Figure 2.3: Layout of the grid cells for a model with $f = 3.8$.

Synthetic observations are created from the molecular excitation by performing ray-tracing after placing the object at a distance of 140 pc and an inclination i (a free parameter). The resulting spectra are convolved with the appropriate Gaussian beams. Figure 2.1 shows the best-fit model spectra (the best fit is discussed in section 2.3).

2.2.4 Modeling the neighboring cloud core

During the optimization of the fit (Sect. 2.2.5) it became obvious that several lines, and especially those of lower-lying rotational transitions taken in large beams, were contaminated by emission with small line width. This emission component is especially clear in the $C^{18}O$ J=1–0 and 2–1 lines, the CS J=2–1 line, the HCN J=1–0 line, and, to some extent, the HCO^+ J=1–0 line (Fig. 2.1). The emission has a V_{LSR} of 6.8 km s^{-1}, slightly lower than that of L1489 IRS of 7.2 km s^{-1}. Cold fore- or background gas with small turbulent velocity is the likely cause for this component. The 850 μm SCUBA map from Hogerheijde & Sandell (2000) reveals that L1489 IRS sits at the edge of an extended, probably starless, cloud core with a radius of 60$''$ (8400 AU). Cold gas in this core therefore contributes to the low-J emission lines, and especially in spectra taken with large beams.

We construct a simple description for the neighboring core, so that we can take its emission into account in our optimization of the model for L1489 IRS, as well

as its absorption if this source is located behind the core. We approximate the core as spherical with a radius of $60''$, which is roughly the distance of L1489 IRS to its centre. We assume that it is isothermal at 10 K and that it has abundances typical for starless cores (Jørgensen et al. 2004). For the species which does not show any cloud core emission, the abundances are unconstrained and we just set the abundances sufficiently low. In the case of CO we use an abundance of 5×10^{-5}. The CS abundance is set to 2×10^{-9}, and the HCO$^+$ and HCN abundances are 27×10^{-9} and 4×10^{-9} respectively. We derive its density distribution by fitting the 850 μm emission from Hogerheijde & Sandell (2000). We find an adequate fit for a radial power-law with slope -2 and a density of 4×10^6 cm^{-3} at $r = 1000$ AU resulting in a cloud mass of 2.9 M$_\odot$. This is consistent with the drop off in density found in many starless cores on scales ($r > 1000$ AU) that are relevant to us (André et al. 1996). Because it falls outside even our largest beam on L1489 IRS we do not investigate if the density in the neighboring core levels off at the center, as is seen for many starless cores. The relative smoothness of the 850 μm emission suggest that this is the case, however.

Using *RATRAN* we calculate the expected emission and the optical depth of each of the observed transitions. In our model optimization procedure (see below), the emission from L1489 IRS and the neighboring core are added on a channel-by-channel basis, with the appropriate spatial offset for the core. We find that we can only make a fit that is reasonable if L1489 IRS is located behind the core; we need both the emission and the opacity of the cloud. This is taken into account by first attenuating the emission from L1489 IRS by the core's opacity, again on a channel-by-channel basis, and subsequently adding the core's emission in each channel, followed by beam convolution.

In this section we derived only an approximate model for the neighboring core. Its effects are taken into account in the model spectra, but the description of the core is not accurate enough to include in the model optimization. This would require a much more detailed analysis than possible here. In the procedure outlined in the next section, we therefore mask out those regions in the spectra strongly affected by the emission and absorption of the core.

2.2.5 Optimizing the fit

Our model has four free parameters: the inclination i, the flatness parameter f, the stellar mass $M_\star$, and the angle of the velocity field α. In addition, the abundances of the molecules are unknown. All other parameters are kept fixed. Table 2.2 lists the parameters.

Considering the size of the parameter space and the time it takes to calculate

a single spectrum[1] the task of finding the parameter vector resulting in the best fit is non-trivial. This is further complicated by the degeneracy of the model results to different parameters. For example, increasing the abundance can have the same effect on the line intensity as increasing the inclination or the flatness, but these will have very different effects on the line profile shape.

Instead of calculating all possible models in the allowed parameter space, we use Voronoi tessellation of the parameter cube (see e.g. Kiang 1966, for details on Voronoi tessellation). A random set of n points p_n in the parameter cube is picked and model spectra are calculated for each of these. Then the parameter cube is divided into Voronoi cells, defined as the volume around a point p_i in the parameter cube containing all points q closer to p_i than to any other of the points p_n ($n \neq i$). The parameter cube is scaled in arbitrary units, so that the allowed parameter ranges falls between 0 and 1. On this dimensionless unit cube a simple metric in d dimensions is used to define the cells,

$$s^2 = \sum_{i=1}^{d} (q_i - p_i)^2 \, , \qquad (2.5)$$

assuming that the solution depends linearly on all parameters. This assumption is not true especially for large values of s, but because we have no knowledge of the geometry of the parameter space, we use the simplest possible measure. In order to minimize the effect this has on our final solution we can increase the initial sample rate so that the average distance between the points becomes smaller. After one or two iterations, the volume of each cell is small enough so that the assumption of linear dependency is good. By scaling the parameters to the same range we make sure that each parameter is weighted equally in the distance measure.

The cell which contains the point p_i resulting in the best fit is chosen, and a new set of random points are picked within this cell, and the procedure is iterated until sufficient convergence has been achieved. This method is only guaranteed to reach the true best fit if only one global minimum exist and if there are no (or few) local minima. To check whether we find the true optimum, we make several runs, with different randomly distributed initial points. We find that we always reach the same minimum, and conclude that local minima are few and not very deep.

For every calculated model spectrum, the fitness is evaluated by regridding the model spectrum to the channel width of the corresponding observed spectrum, centering it on the LSR velocity of 7.2 km s^{-1}, and calculating the χ^2 between the

---

[1]Depending on the species and the optical thickness, we can calculate a spectrum in between five minutes and half of an hour, on a standard desktop processor.

model and the observed spectrum,

$$\chi^2 = \frac{1}{M} \sum_m \frac{1}{N_m} \sum_n \frac{(I(n)_{obs} - I(n)_{model})^2}{\sigma_m^2},$$ (2.6)

where M is the number of spectra and N is the number of velocity channels in the m'th spectrum. This way we give an equal weight to all spectra even though the number of channels vary in each spectrum. Those channels affected by the neighboring core are not included in the χ^2 measure. Every spectra has a fixed passband of 14 km s^{-1} so that an equal amount of baseline is included for each spectrum.

Using this method, with a set of 24 random points per iteration, we converge on an optimal solution after four to five iterations, corresponding to 10 to 12 days of CPU time. For practical reasons we initially chose only to consider the most structured lines (CO, HCO$^+$ and CS), lowering the computational time to about a single day and getting a quick but rough handle on the initial parameter cube. We then included the other lines to obtain the overall best solution.

2.2.6 Error estimates

Getting a handle on the uncertainties in the obtained parameter values is a difficult matter due to the size and complexity of the parameter space. As mentioned above, we have no knowledge of the overall geometry of the parameter space and given the long computation time of the optimization algorithm, we cannot make a correlation analysis of each pair of parameters and neither can we make χ^2 surfaces. Still, it is very important to get an estimate on the stability and reliability of our solution.

A simple error analysis is done for the four model dependent parameters, the flatness, the velocity angle, the stellar mass, and the inclination, by fixing three of the parameters at their best fit values, and calculating models in which the fourth parameter is gradually increased from its lower boundary to the upper boundary. Plots of the resulting (inverse) χ^2 values are shown in Fig. 2.4. The χ^2 values are approximately normally distributed, with the main discrepancy in the high values of the inclination, velocity field, and the flatness. This relates to the non-linear nature of the trigonometric functions associated with these three parameters.

A Gaussian has been fitted to each of the histograms in Fig 2.4. The centre of the Gaussian is fixed on the best fit value and the height is fixed by the χ^2 value of the best fit so that only the variance, σ^2, is free. Reasonable fits are achieved for each parameter with the σ value given in each panel. These values
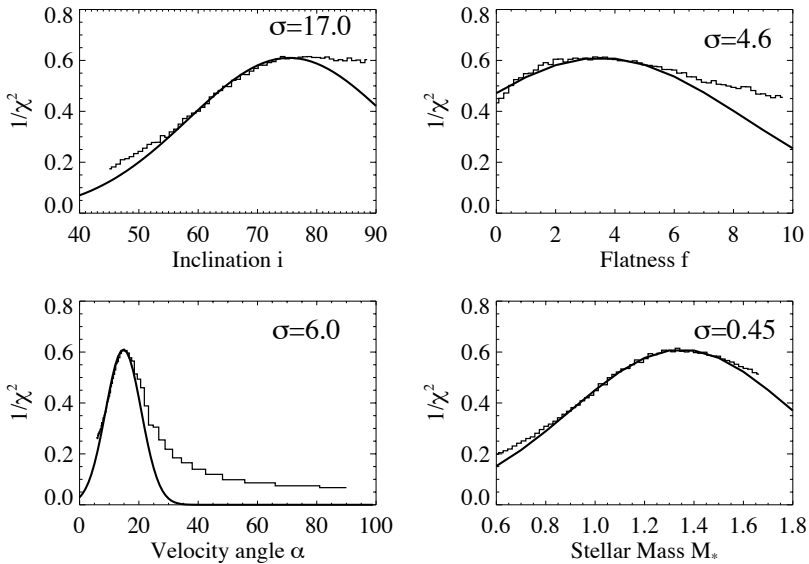
Figure 2.4: These graphs show the $1/\chi^2$ distributions of models around the best fit position where only one parameter is varied at each time. A Gaussian, centered on the best fit in each panel, is fitted to the distributions. The dispersion of the Gaussians are given in each panel.

are taken to be a rough estimate of the magnitude of the error in each of the four parameters. For the inclination and flatness, where the error is greater than the allowed parameter range, the error is of course determined by the physical constrains on the parameter value (e.g., the inclination cannot be greater than 90°). Note that the error bars are typically smaller than the explored range in each parameter by a factor of 2–10.

With this kind of one dimensional error analysis we do not take into account the fact that the parameters are likely to be highly correlated. A few exploratory calculations, where one parameter was held fixed at its best fit value while the other three where randomly pertubed around their best fit values, indicated that there exist a strong correlation between the parameters. Indeed, a degeneracy exists between the central mass and the inclination, which again is degenerate with the flattening. Only a full parameter space study can fully disentangle this and is beyond the scope of this chapter.

Because the abundance parameter mainly serves to scale the intensity in every

channel of the spectrum, and does not change the shape of the profile much, this kind of error analysis is of little use. For any combination of the four free parameters that reproduces the observations, a corresponding abundance is found from the optically thin isotopic lines. These abundances are relatively insensitive to the exact geometry because of their optically thin nature. Therefore we assume that the error in the abundance values obtained here is entirely dominated by the 20% calibration error of the observed spectra.

Throughout this work we have assumed constant abundance for all the molecular species. In reality, abundances will depend on the chemistry and molecules will freeze out below a certain temperature. This gives rise to a drop in the abundances at a certain radius and it will affect, to some extent, the shape of the profiles but more prominently, the line ratios. Specifically, by removing low temperature material from the gas phase, low excitation lines become relatively weaker. Our model does not suffer from the problem of over-producing the low J lines, except for the case of HCO$^+$; a more complex abundance model would likely provide a better fit to the $J= 1$–0 and 3–2 lines. However, this would require a careful chemical analysis which is beyond the scope of this chapter. A few tests showed that letting CO freeze out at 20 K does not change the best fit parameters significantly, except for the abundance which will then have to be re-optimized. We return to the topic of chemical depletion in the envelopes of YSOs in later chapters of this thesis where we explore the effect of depletion on the velocity field parameters.

2.3   Results

Figure 2.1 compares the data to the synthetic spectra based on the best fit model obtained with the optimization procedure described above. The results for the combined emission of L1489 IRS and the neighbor core is shown in Fig. 2.5. Because the emission from the core only contributes to the low J-lines, this figure only shows the species in which the combined spectrum show any difference from the L1489 IRS spectrum alone. For all species not shown in Fig. 2.5, the combined spectra is indistinguishable from the one shown in Fig. 2.1. Table 2.2 lists the parameters of the best fit.

The inclination angle of 74° falls within the range of 60° to 90° which is inferred from the scattered light image of Padgett et al. (1999) and the modeling of the infrared spectral energy distribution (Kenyon et al. 1993b). Section 2.3.2 shows that this inclination and the flattening parameter f = 3.8 reproduce the scattered light image, including the detectability of the central star. The resulting density distribution can be well approximated by a disk with a vertical density dis-
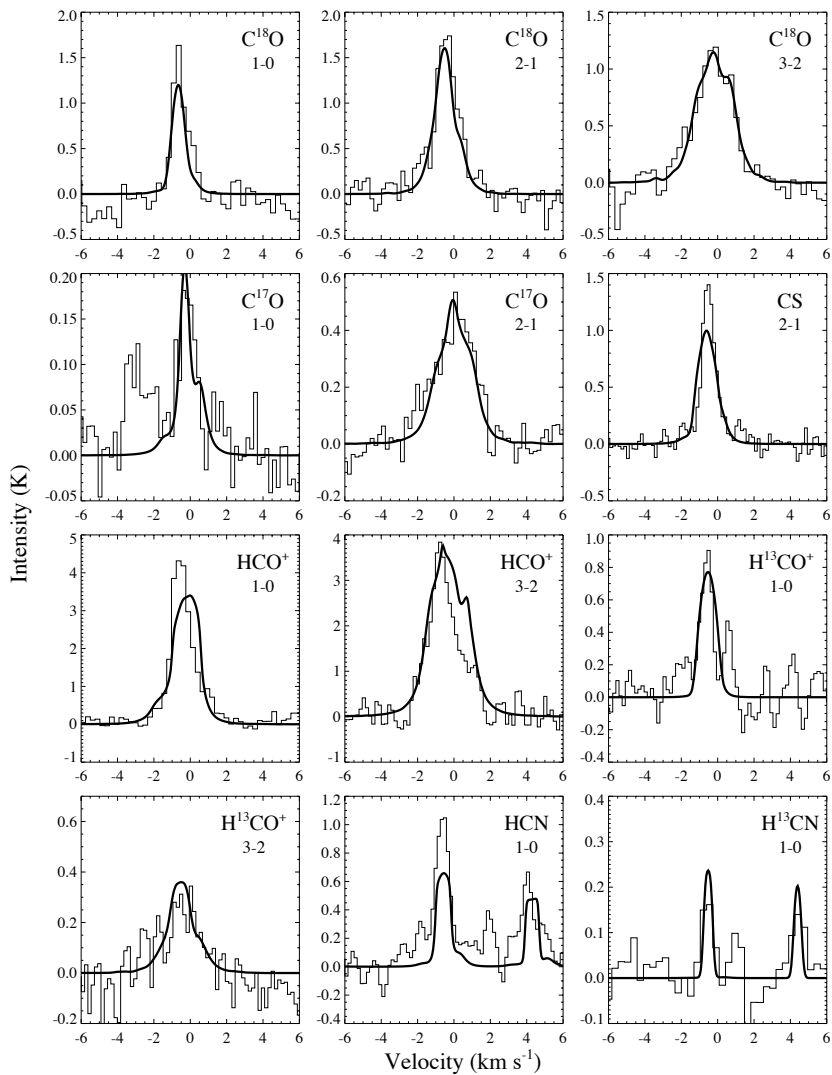
Figure 2.5: The combined emission from the L1489 IRS model and the neighbor cloud core. Only spectra which are affected significantly by the cloud core emission are shown here.

Table 2.2: Best fit parameters

Free Parameters	Value
Inclination of disk, i	$74°$
Flatness of disk, $\sin^f(\theta)$	3.8
Central mass, M_*	1.35 $M_\odot$
Velocity angle, α	$15°$
Abundance of CO[a]	3.5×10^{-5}
Abundance of CS	0.5×10^{-9}
Abundance of SO	2.0×10^{-9}
Abundance of HCO$^+$	1.9×10^{-9}
Abundance of HCN	0.2×10^{-9}
Abundance of HNC	0.2×10^{-9}
Abundance of CN	0.2×10^{-9}
Abundance of H_2CO	0.7×10^{-9}
Fixed parameters	
Disk mass	0.097 $M_\odot$
Temperature slope	-0.35
Temperature at 1000 AU	19.42 K
Density slope	-1.8
Turbulent velocity, FWHM	0.2 km s^{-1}
Outer radius	2000 AU
Distance	140 pc

[a] The main isotopic abundance has been derived from the $C^{18}O$ abundance using a $^{16}O/^{18}O$ ratio of 560 (Wilson & Rood 1994).

tribution $\propto e^{-z^2/2h^2}$ and a scale height of $h \approx 0.57R$. The maximum deviation of this approximation is only 4%, up to an angle of 60° above the midplane. Hogerheijde (2001) described L1489 IRS using a flared disk with an adopted density scale height of $h = 0.5R$, so our best fit model is consistent with the flat structure might assumed by Hogerheijde (2001). They, however, used an inclination of 90° for the flared disk (a flat disk at $i = 60°$ was also tried), but the projected column density distribution are quite similar in both cases.

The best fitting velocity vector makes an angle of only 15° with respect to the azimuthal direction, consistent with Hogerheijde (2001) who shows that rotation is the primary component in the velocity field. However, our central stellar mass of 1.35 $M_\odot$ is considerably higher than the 0.65 $M_\odot$ derived by Hogerheijde. Part of this is due to different definitions of the velocity field. Hogerheijde reports a mass expected for Keplerian motion based on the azimuthal component of the velocity field alone, while the mass derived here results in $\cos\alpha$ times the Keplerian velocity (Eq. 2.3 and 2.4). In addition, a different inclination is found. These two factors together would give a mass of 1.2 $M_\odot$ for our model. This mass is still 80% higher than that from Hogerheijde but our best fit has a χ^2 value of 1.69. This is nearly half of that of the best model of Hogerheijde of ~3. We ascribe this difference to a more thorough search of the parameter space.

The best fitting abundances are consistent with the abundances obtained for L1489 IRS by Jørgensen et al. (2004) to within a factor of 2–3 although the values obtained here are all higher. This may be due to higher line opacities in our model as a result of the different adopted velocity fields; Jørgensen et al. do not include a systematic velocity field and only a single turbulent line width. Consistent with this previous work, we find no evidence for depletion of CO, in accord with the relatively high temperatures exceeding the 20 K evaporation temperature of CO throughout most of the disk. Another interesting finding is the CN/HCN abundance ratio of 1.0, which is more reminiscent of dark clouds than of circumstellar disks, suggesting that chemically, L1489 IRS is close to its original cloud core and that photo-dissociation does not play a major role yet (Thi et al. 2004).

2.3.1   Quality of the best fit

The overall correspondence of our model to the data is good and most of the spectra are well reproduced. The line widths of $C^{18}O$ and $C^{17}O$ are well reproduced, and the $C^{17}O$ J=2–1 and 3–2 lines are found to exclusively trace L1489 IRS and to be uncontaminated by the neighboring core. All three $C^{18}O$ lines and the $C^{17}O$ J=1–0 line have narrow line peaks that originate in the neighbor core; some $C^{18}O$ $J = 1$–0 emission that is not reproduced can either be caused by additional mate-

rial along the line of sight, or be due to the approximate nature of our description of the core.

The sulfur bearing lines are not very intense and show little structure. Again we see a narrow peak in the CS $J = 2–1$ almost entirely accounted for by the neighboring core and perhaps also in the SO line. The non-detection of $C^{34}S$ $J = 2–1$ places an upper limit on the CS abundance in the neighboring cloud of 2×10^{-9}. The CS $J = 7–6$ line is poorly fit, but on the other hand, the observed spectrum has a low signal-to-noise ratio.

The HCO^+ lines are the strongest among our sample and show most structure in their profiles. It was important to be able to reproduce the double peak in the HCO^+ $J = 4–3$ line because this feature is a very clear tracer of the velocity structure in L1489 IRS. Our model is able to reproduce this feature. However, we do not observe the double peak in the HCO^+ $J = 3–2$ line but only a slight asymmetry. This provided a major constraint on the velocity field. The neighbor core does not contribute in the $J = 4–3$ line but it makes up for almost all of the excess emission seen in the $J = 1–0$ and $3–2$ lines of HCO^+.

Of the nitrogen bearing species, HCN $J = 1–0$ with its three hyperfine components shows very narrow lines, which are well reproduced by the neighbor core model which dominates the emission. The HCN $J = 4–3$ line is much broader and uncontaminated by the neighboring core. A narrow peak in the spectrum at 8 km s^{-1} cannot be due to the neighbor core and we assume it is noise. The HNC $J = 4–3$ line has a rather low signal to noise ratio and can only provide a reliable estimate within a factor of a few. CN $J = 1–0$ also has a low signal-to-noise ratio, but in the case of CN, the abundance is well constrained by the $J = 3–2$ line.

All spectra discussed above have been obtained with single-dish telescopes that do not resolve the 2000 AU radius source. One can wonder if it is justifiable to use a non-spherical model when the single-dish observations does not contain any spatial information. Although the scattered-light and interferometer images show that the structure is non-spherical, one could argue that introducing the flattening is simply a way to improve the fit by adding a free parameter. However, this is not the case. Figure 2.6 shows the best fit to the HCO^+ $J = 4–3$ line, with a spherical model ($f = 0$) and a model where the flattening and inclination are free parameters. The flattened model provides a considerably better fit with lower χ^2 value, and, more importantly, the spherical model shows too much self absorption. Our optimization algorithm returns the model which minimises the difference between data and model for each velocity channel. In a spherical model the column simply becomes too high. By flattening the model and adjusting the inclination, we can exactly reproduce the right amount of self absorption seen in the data while
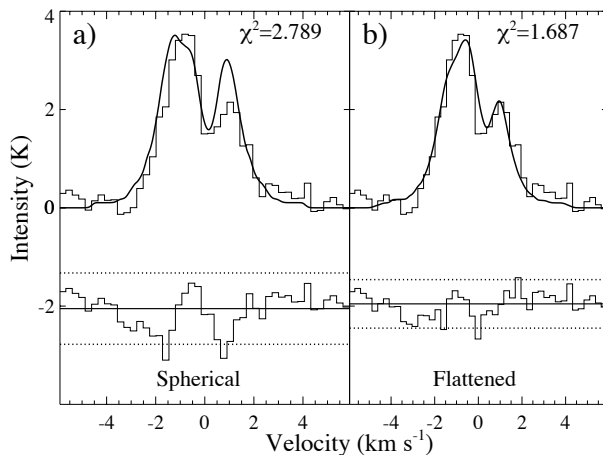
Figure 2.6: **a)** Best possible fit with a spherical model to the HCO$^+$ $J= 4$–3 line. **b)** The best fit to the same line where the flattening f and the inclination i are kept as free parameters. Below, the residuals are shown with the mean and two standard deviations indicated.

keeping the total column density high enough to produce the right line strength. The degeneracy between these two parameters are resolved by the velocity field, and thus it turns out that it is actually possible to retrieve spatial information from single-dish observations.

Ward-Thompson & Buckley (2001) have argued that the amount of self absorption can also be regulated by adjusting the turbulent velocity dispersion. We can indeed change the quality of the spherical fit by changing the amount of turbulence. We cannot, however, do that without also changing the velocity distance between the two peaks. Thus in order to fit the line width we must decrease the mass and thereby the magnitude of the velocity field, which no longer reproduces the observed infall asymmetry. We therefore find that varying the turbulent velocity width in a spherical model does not reproduce the observations.

2.3.2 Comparison to other observations

With the best fit parameters derived above, we can now test our model by comparing it with other observations of L1489 IRS not used in the fit. The neighboring cloud is not considered in the following.

Interferometer image of HCO$^+$ $J = 1$–0

We have used our model to produce a synthetic interferometer map of the HCO$^+$ $J=1$–0 emission which can be directly compared to the data presented by Hogerheijde (2001). Figure 2.7 compares the model predictions of the integrated intensity and velocity centroid maps to the observations reproduced from Hogerheijde (2001). We also show a model with $f = 1$ and on with $f = 8$ for comparison. The model images were made by taking the unconvolved image cubes from *RATRAN* and then, using the (u, v) settings from the original data set, making synthetic visibilities with the 'uvmodel' task from the *MIRIAD* software package. This is what we would get if the interferometer observed our model object. Then we applied the usual deconvolution with the invert, clean, and restore routines in order to reconstruct an image from the visibilities.

The resulting synthetic image of our best fit model resembles the observations closely within the uncertainty of the abundance which strongly affects the apparent size, when it is taken into account that the observations also partially recover the neighboring core that is ignored in the model (Fig. 2.7, panel b). However, the $f = 8$ model in panel d) is also in good agreement with the data which partially can be explained by the fact that, due to the non-linearity of the sine function, the difference between an $f = 3$ and $f = 10$ model is much less than the difference between an $f = 1$ and $f = 3$ model. This is also reflected in Fig 2.2. In any case, panel c) is obviously in poor agreement with the data, which shows that in order to fit the interferometer data, a flattened structure is needed.

This kind of analysis is very useful to investigate the spatial distribution of the emission which is lacking in the single dish data. Importantly, we see that the flattening which we introduced and the amount of which we determined from the line profile results in a projected shape that is very close to what we see in the data image. Also, because the cuts are the same in both panels, the extent of the emission and therefore the physical size scale of the model is consistent.

Near-infrared image

We subsequently test our best-fit model through a comparison with the near-infrared scattered light image of Padgett et al. (1999). A reproduction of this image is shown in the top left panel of Fig. 2.8. Using the density structure and inclination found in Sect. 2.3 and the properties of the central star as described in the introduction as input, we calculated the scattering light emission with *RADMC*, a two-dimensional radiation transfer code (Dullemond & Dominik 2004). Then, using the ray-tracing code *RADICAL* (Dullemond & Turolla 2000), we extract the
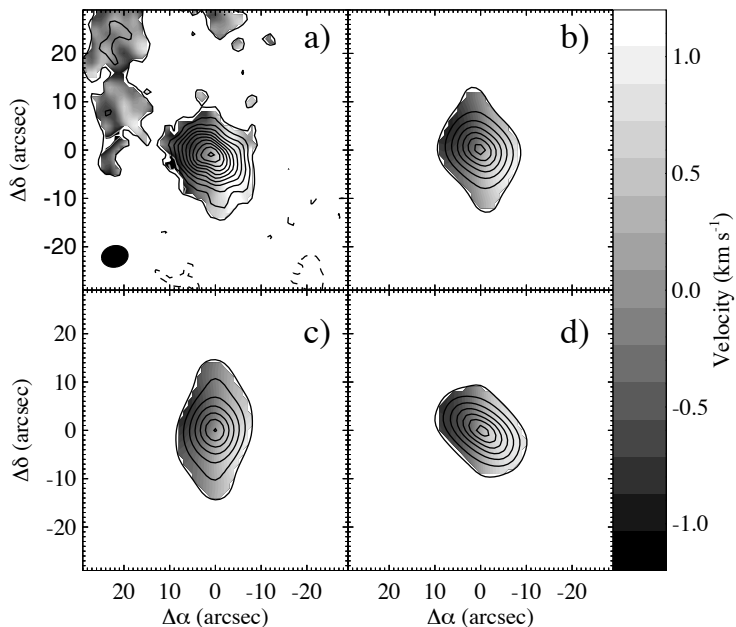
Figure 2.7: **a)** Interferometer map in HCO$^+$ $J= 1$–0. **b)** The corresponding synthesised map based on our best model. **c)** and **d)** Models with $f = 1$ and $f = 8$ respectively. The black contour lines show the integrated intensity (zeroth moment), starting at 0.25 Jy beam^{-1} and increasing in steps of 0.5 Jy beam^{-1}. The colour scale shows the velocity centroid (first moment).

fluxes over the full spectral range of 1 to 850 μm and image our model in the $F110W$, $F160W$, $F210W$ NICMOS bands.

Our best fit model of Sect. 2.3 automatically provides a good fit to the sub-millimeter part of the spectral energy distribution, confirming that our model is consistent with the results of Jørgensen et al. (2002). The near-infrared observations are more difficult to match. The column density in the inner part is too high to provide the clear view of the central star that shows prominently in NIC-MOS images. However, if we reduce the scale height in the inner 250 AU to $h = 0.15R$, the column density is reduced and the central star becomes detectable
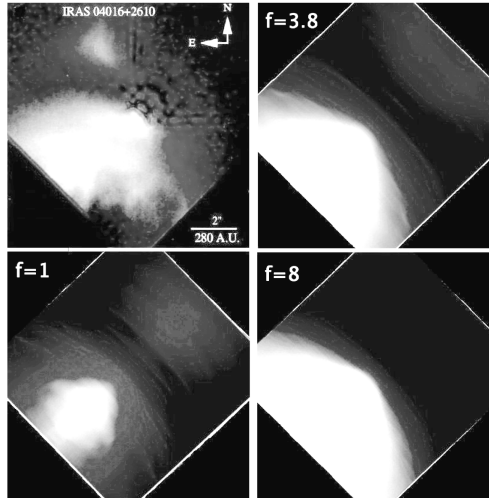
Figure 2.8: The top left panel shows the false color NICMOS image of L1489 IRS from Padgett et al. (1999). In the three remaining panels are shown synthetic three-color composite images based on our model.

in the near-infrared. This adaptation does not affect the sub-millimeter emission or the molecular line intensities viewed in the much larger single-dish beams.

The resulting three-color composite images of our best fit model as well as a f=1 and f=8 model, are shown in Fig. 2.8. Although this can only be a qualitative comparison, our model is able to reproduce most of the striking features evidenced by the observations. The opening angle of the dust cavity is found to be somewhat dependent on the flattening parameter f in our model. Although it is difficult to judge the agreement, this result seems to favor a relatively low value of f as opposed to what we found above for the interferometric map. The non-monotonic behaviour along the axis in the $f = 1$ model is a combination of the finite gridding of the density structure and the effect of scattering. It has a very narrow cavity and so the base of the scattering nebula is actually absorbed by the high density material in the inner part. In the other models the cavity is large enough to allow all the scattered photons to escape.

We also reproduce the near-infrared colors, confirming our adopted density distribution between ~100 AU and ~2000 AU. Each of the NICMOS fluxes are reproduced to within ~40%. Although a detailed modeling of L1489 IRS on these scales where most of the near-infrared emission is coming from was beyond the

scope of this chapter, we present this prediction to demonstrate that it is possible to combine the information contained in near-infrared images and sub-millimeter single-dish measurements to obtain a self-consistent model on scales ranging from within a few AU up to several thousand AU.

The cavity seen in the NICMOS image is likely associated with a molecular outflow. However, Hogerheijde et al. (1998) show that L1489 IRS only drives a modest ^{12}CO outflow, and little or no impact on the line profiles is expected. Therefore, an outflow has not been incorporated into the model described in this chapter.

^{12}CO 4.7μm absorption bands

Finally we apply our model to fit the CO ro-vibrational absorption bands, again by using *RATRAN*. Here we assume that initially all CO molecules are in the vibrational ground state (v=0) but can be excited to a v=1 state by absorption of a photon from the central star, producing the absorption lines in the P and R branches corresponding to $\Delta J = \pm 1$ transitions. Observations of these bands from the Keck/NIRSPEC instrument have been presented by Boogert et al. (2002). The spectrally resolved absorption lines revealed inward motions up to 100 km s^{-1}. Using the same method as Boogert et al. we calculated the ro-vibrational absorption lines in our model, and plot the average of the P(6)-P(15) lines in Fig. 2.9.

We find that our model fits the data as well as the results from Boogert et al., who use a contracting flared disk with power laws for the temperature, density, and infall velocity. This means that the amount of inward velocity that we obtained from the fit to the single dish lines together with the adopted density profile can explain the observed infall, even at radii much smaller than probed with the single dish lines. In Fig. 2.9 we see that absorption is present all the way up to at least 100 km s^{-1}. In our model, this velocity translates into a radius of 0.02 AU. Material absorbing at 50 and 20 km s^{-1} is located at 0.06 and 0.4 AU respectively.

2.4   Discussion

In this chapter we have derived an accurate model for the circumstellar material of L1489 IRS. We find that it is well described by a flattened structure with a radius of 2000 AU in sub-Keplerian motion around a 1.35 M$_\odot$ central star. While the structure resembles disks found around T Tauri stars (e.g. Simon et al. 2000), its 2000 AU radius is much larger than T Tauri disks (typically several hundred
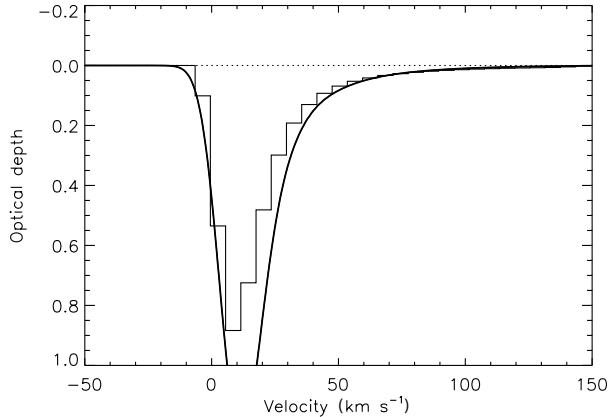
Figure 2.9: An average of the observed ^{12}CO P(6)-P(15) lines with a similarly averaged model result (thick line) plotted on top.

AU). Also, disks around T Tauri stars are often well described by pure Keplerian motions except for a few cases, e.g. AB Aur, in which outwards non-Keplerian motions are measured (Piétu et al. 2005; Lin et al. 2006). In this section we discuss the evolutionary state of L1489 IRS, and particularly whether it represents a unique case or if other forming stars may go through a similar stage. We start by deriving the life span of the current configuration. We then explore the relation of L1489 IRS to its neighboring core. Finally, we discuss a number of open questions that only new observations can answer.

By integrating the trajectory of a particle at 2000 AU we find the infall time scale to be 2.3×10^4 years. Dividing the 0.097 $M_\odot$ of the circumstellar material yields a mass accretion rate of 4.3×10^{-6} $M_\odot$ yr^{-1}. Estimating the radius of the central star from the mass-radius relation (Stahler 1988) to be 4 $R_\odot$ results of an accretion luminosity of $L_{acc} = GM_* \dot{M}/R_* \approx 46$ $L_\odot$ corresponding to about ten times the observed bolometric luminosity from the YSO (Kenyon et al. 1993a). This suggest that not all inspiraling material falls directly onto the star. The result is somewhat higher than the one found by Hogerheijde (2001), although the modeling approach used in that paper was completely different.

In our model we also assume a constant angle α for the direction of the velocity vector. In reality, this direction could vary with radius as the angular momentum distribution changes. For example, at smaller radii, α could be smaller as the

velocity field more closely resembles pure Keplerian rotation. The inspiral time, and mass accretion rate, can therefore be very different. Only higher resolution observations can investigate this further.

Is L1489 IRS in any way special? No objects like it are reported in the literature. Since its life time is of the order of a few 10^4 yr, roughly 5–10% of the embedded phase, more objects like it would be expected. It is possible that L1489 IRS was formed out of a core with unusually large angular momentum, which led to the formation of an untypically large disk. We cannot exclude that possibility, but hydrodynamical simulations are required to investigate how much angular momentum would be required, and if turbulent cloud cores can contain such amounts of rotation.

An intriguing possibility is that the proximity of the neighboring core is in some way related to L1489 IRS' special nature. The core is 60″ (8400 AU) away in projection, and located in front of L1489 IRS, likely by a distance of comparable magnitude. Its systemic velocity is 0.4 km s^{-1} lower than that of L1489 IRS itself, indicating that L1489 IRS and the core currently are moving away from one another, at least in the direction along the line of sight. Could the neighboring core be feeding material onto the disk of L1489 IRS? The velocity gradient is such that it merges smoothly with the velocities in the core (see Fig. 2.7). This suggests that a physical link between the core and the disk may exist. If the core feeds material onto the disk, this could be a significant source of angular momentum, thus keeping the disk large. It is, however, not easy to understand why gas in the core would be gravitationally bound to the L1489 IRS star, because of the significant mass reservoir in the core itself of 2.9 M$_\odot$.

Another hypothesis is that L1489 IRS actually originated inside the core, but has since migrated away. Its current velocity offset of 0.4 km s^{-1} is sufficient to move it to its current location 60″ away in a few times 10^5 yr, the typical life time of an embedded YSO. We of course do not know how far its offset along the line of sight is, or what its three-dimensional velocity vector is like. Its line-of-sight velocity of 0.4 km s^{-1} is not very different from the velocity dispersion of T Tauri stars and the turbulent motions in cloud complexes. One could propose that L1489 IRS' natal core was a turbulent, transient structure, and that, once formed, the YSO migrated with its gravitationally bound disk-like environment to a location outside the surrounding cloud core, in effect 'stripping' the Class I object from most of its envelope. In this scenario we would now be seeing the inner, rotating Class I envelope around L1489 IRS unobscured by the outer envelope. This might account for the different appearance of L1489 IRS.

This hypothesis can be tested in two ways. First, 'normal' Class I objects can

be studied at high spatial resolution and in dense gas tracers to explore if the inner envelope is dominated by rotation on 1000 AU scales. Second, hydrodynamical calculations can be used to explore on what time scales newly formed YSOs can migrate away from their nascent cloud core. Searching for other objects like L1489 IRS would also be very useful. Potential targets would appear compact in sub-millimeter continuum images, but show strong emission lines in dense gas tracers. L1489 IRS shows HCO^+ lines with intensities of several K, while a few tenths of K is more typical for T Tauri disks (Thi et al. 2004).

2.5 Summary

We have made a two-dimensional axi-symmetric disk-like model of the young stellar object L1489 IRS. Line radiation transfer calculations produce synthetic spectra which can be directly compared to observations. We show that a flattened model gives a better description than a spherical one. Our model also reproduces millimeter interferometric imaging, near-infrared scattered light images, and CO ro-vibrational absorption spectroscopy.

We conclude further that the central star has a mass of 1.35 $M_\odot$. The velocity vectors make an angle of 15° with the azimuthal direction. The velocity field is dominated by rotation, while small but significant amount of infall are present.

A neighouring cloud core is present next to L1489 IRS. This cloud is well modeled by generic dark cloud parameters and we argue that it is likely situated in front of L1489 IRS. We speculate that this core could be feeding high angular-momentum material onto the L1489 IRS disk, explaining the unusual size of this object. Another explanation could be that L1489 IRS is an ordinary Class I object which has migrated away from its parental core, leaving it surrounded by only its gravitationally bound inner envelope. If this is true, L1489 IRS may provide valuable insight on the formation of protoplanetary disks.

In this chapter we show that it is possible to construct a global model of a young stellar object that is able to fit observations on a wide range of spatial scales. Single-dish line observations provide enough information to make highly detailed models of circumstellar structures, even on scales that are unresolved. However, on scales as small as 100 AU, the description may no longer be accurate, as evidenced by the near-infrared scattered light which suggest additional flattening of the disk-like structure. In chapter 4 we investigate this scenario further by extending the L1489 IRS model to smaller scales and comparing it to high resolution interferometric observations obtained with the Submillimeter Array.

Acknowledgements

References

Adams, F. C., Shu, F. H., & Lada, C. J. 1988, ApJ, 326, 865

André, P., Ward-Thompson, D., & Barsony, M. 2000, Protostars and Planets IV, 59

André, P., Ward-Thompson, D., & Motte, F. 1996, A&A, 314, 625

Boogert, A. C. A., Hogerheijde, M. R., & Blake, G. A. 2002, ApJ, 568, 761

Dullemond, C. P. & Dominik, C. 2004, A&A, 417, 159

Dullemond, C. P. & Turolla, R. 2000, A&A, 360, 1187

Gregersen, E. M. & Evans, N. J. 2000, ApJ, 538, 260

Guilloteau, S. & Dutrey, A. 1998, A&A, 339, 467

Hogerheijde, M. R. 2001, ApJ, 553, 618

Hogerheijde, M. R. & Sandell, G. 2000, ApJ, 534, 880

Hogerheijde, M. R. & van der Tak, F. F. S. 2000, A&A, 362, 697

Hogerheijde, M. R., van Dishoeck, E. F., Blake, G. A., & van Langevelde, H. J. 1997, ApJ, 489, 293

Hogerheijde, M. R., van Dishoeck, E. F., Blake, G. A., & van Langevelde, H. J. 1998, ApJ, 502, 315

Jørgensen, J. K., Schöier, F. L., & van Dishoeck, E. F. 2002, A&A, 389, 908

Jørgensen, J. K., Schöier, F. L., & van Dishoeck, E. F. 2004, A&A, 416, 603

Kenyon, S. J., Calvet, N., & Hartmann, L. 1993a, ApJ, 414, 676

Kenyon, S. J., Whitney, B. A., Gomez, M., & Hartmann, L. 1993b, ApJ, 414, 773

Kiang, T. 1966, Zeitschrift fur Astrophysik, 64, 433

Koerner, D. W. & Sargent, A. I. 1995, AJ, 109, 2138

Lada, C. J. & Wilking, B. A. 1984, ApJ, 287, 610

Lin, S.-Y., Ohashi, N., Lim, J., et al. 2006, ApJ, 645, 1297

Lizano, S. & Shu, F. H. 1989, ApJ, 342, 834

Mardones, D., Myers, P. C., Tafalla, M., et al. 1997, ApJ, 489, 719

Myers, P. C., Fuller, G. A., Mathieu, R. D., et al. 1987, ApJ, 319, 340

Nenkova, M., Ivezic, Z., & Elitzur, M. 1999, LPI Contributions, 969, 20

Ossenkopf, V. & Henning, T. 1994, A&A, 291, 943

Padgett, D. L., Brandner, W., Stapelfeldt, K. R., et al. 1999, AJ, 117, 1490

Piétu, V., Guilloteau, S., & Dutrey, A. 2005, A&A, 443, 945

Reipurth, B., Jewitt, D., & Keil, K., eds. 2007, Protostars and Planets V (University of Arizona Press)

Schöier, F. L., van der Tak, F. F. S., van Dishoeck, E. F., & Black, J. H. 2005,

A&A, 432, 369

Shu, F. H. 1977, ApJ, 214, 488

Simon, M., Dutrey, A., & Guilloteau, S. 2000, ApJ, 545, 1034

Stahler, S. W. 1988, ApJ, 332, 804

Stamatellos, D., Whitworth, A. P., André, P., & Ward-Thompson, D. 2004, A&A, 420, 1009

Thi, W.-F., van Zadelhoff, G.-J., & van Dishoeck, E. F. 2004, A&A, 425, 955

Ward-Thompson, D. & Buckley, H. D. 2001, MNRAS, 327, 955

Wilson, T. L. & Rood, R. 1994, ARA&A, 32, 191

Chapter **3**

Characterizing the velocity field in a hydrodynamical simulation of low-mass star formation using spectral line profiles

Abstract

When low-mass stars form, the collapsing cloud of gas and dust goes through several stages which are usually characterized by the shape of their spectral energy distributions. Such classification is based on the cloud morphology only and does not address the dynamical state of the object. In this chapter we investigate the initial cloud collapse and subsequent disk formation through the dynamical behavior as reflected in the submillimeter spectral emission line profiles. If a young stellar object is to be characterized by its dynamical structure it is important to know how accurately information about the velocity field can be extracted and which observables provide the best description of the kinematics. Of particular interest is the transition from infalling envelope to rotating disk, because this provides the initial conditions for the protoplanetary disk, such as mass and size. We use a hydrodynamical model, describing the collapse of a core and formation of a disk, to produce synthetic observables which we compare to calculated line profiles of a simple parameterized model. Because we know the velocity field from the hydrodynamical simulation we can determine in a quantitative way how well our best-fit parameterized velocity field reproduces the original. We use a molecular line excitation and radiation transfer code to produce spectra of both our hydrodynamical simulation as well as our parameterized model. We find that information about the velocity field can reasonably well be derived by fitting a simple model to either single-dish (15″ resolution) lines or interferometric data (1″ resolution), but preferentially by using a combination of the two. The method does not rely on a specific set of tracers, but we show that some tracers work better than others. Our result shows that it is possible to establish relative ages of a sample of young stellar objects using this method, independently of the details of the hydrodynamics.

3.1   Introduction

Low-mass young stellar objects (YSOs) are well-studied phenomena. Observationally, these objects have been measured in many different wavelength regimes in order to determine intrinsic properties such as their mass, luminosity, mass accretion rate, etc. YSOs are traditionally classified by the shape of their spectral energy distribution (SED) (Lada & Wilking 1984), which reflects their general morphology. Subsequently, the envelope and disk densities, temperatures and chemistry can be studied using millimeter continuum and molecular line measurements. All of these derived quantities have been used to piece together a consistent chronology of the process of star formation and to establish a reference from which the age of a YSO can be reliably obtained (Mardones et al. 1997; Gregersen & Evans 2000).

   A theoretical evolution scenario of YSOs has been established for many years (e.g., Ulrich 1976; Shu 1977; Cassen & Moosman 1981; Terebey et al. 1984; Bodenheimer et al. 1990; Basu 1998; Yorke & Bodenheimer 1999). In these models (with the exception of the Shu model, which is spherically symmetric) a circumstellar disk is formed, after the collapse of the initial cloud sets in, due to conservation of angular momentum. It is therefore natural to use the kinematic properties of the models to characterize the evolutionary stage of the object, because the distribution of angular momentum changes in a monotonous way as the cloud contracts and matter spins up. Unfortunately, measuring the velocity field observationally is not such a simple matter. Kinematic information can only be derived from spectral emission lines and there is no way to directly solve for the velocity field from measurements of such lines. The reason for this is that the spectral profile depends on a range of physical parameters, including the local density, temperature, molecular abundance, and turbulence in the region where the particular transition is excited. All of this can be taken into consideration and self-consistent models, including a general parameterized velocity field, can be built and fitted to the observed spectra. The question is, however, how reliable the derived velocity field is given the input model, and to what extent the derived velocity fields are consistent with the prediction of the models.

   The velocity field of YSOs has been well studied observationally in the last 20 years. At first, mainly infall was observed (e.g., Calvet & Hartmann 1992; van Langevelde et al. 1994), but soon afterward, objects showing a mix of infall and rotation were discovered (Saito et al. 1996; Ohashi et al. 1997; Hogerheijde 2001; Belloche et al. 2002). More recently, protoplanetary disks have been studied at very high resolution using sub-millimeter interferometry and they have velocity fields with rotation only (e.g., Lommen et al. 2008). The common interpretation

of these observations is that the objects showing infall only are early-type embedded objects, the rotating disks are the end product of the collapse, and the objects showing both infall and rotation are in some kind of transition. Initial modeling work using a parameterization for the velocity field has been done by Myers et al. (1996) for low-mass star formation and by Keto (1990) for the formation of high-mass stars. However, it has never been attempted to quantify the degree of the transition, how far the object has passed from the embedded phase to the protoplanetary disk phase.

In this chapter we will address this question by comparing synthetic spectra, calculated from a hydrodynamical simulation of a collapsing cloud, to a model with a simple parameterized velocity field. Because we know the physical conditions in the simulation, we can evaluate how well our parameterized model describes the simulated object. The assumption is that *if* our model can describe the velocity field of the hyordynamical simulation reasonably well, we can apply our model to real observed objects and achieve a similarly good description of their velocity fields. The comparison is done in spectral space in the same way as one would compare a model to real observations. By considering different transitions of different molecules in two different resolution settings, we investigate how to obtain the most reliable characterization of the velocity field. The importance of being able to reliably model the observations of YSOs using a simple generic model becomes evident when considering the capabilities of the upcoming ALMA (Atacama Large Millimeter Array). While it is possible to build sophisticated custom models, or even directly use the hydrodynamical simulation as a template model to describe single objects, this is a very time-consuming process. ALMA will produce very high resolution observations ($\sim 0.01''$) in snapshot mode and in order to deal with such vast samples of YSOs, simple yet reliable models are needed.

3.2 Simulations and models

3.2.1 Hydrodynamical collapse

For the description of the gravitational collapse, we use the hydrodynamical framework of Yorke & Bodenheimer (1999). In particular we use the model which simulates the formation of an J-type star given an initial cloud mass of 1 $M_\odot$ and radius of 6667 AU (1×10^{15} m). The cloud is initially isothermal at 10 K and is given a constant solid body rotation of 1×10^{-13} s^{-1}. In this model, an equilibrium disk is formed after about 75000 years after the onset of the collapse, which

then grows up to several thousands of AU as angular momentum is transported outwards. The disk which is formed resembles a thin, flaring disk with a pressure scale height at 500 AU from the star of $h = 0.15R$ and $h = 0.19R$ at 1000 AU from the star.

The code used to calculate the collapse is described in detail by Różyczka (1985), Yorke et al. (1993), Yorke et al. (1995), and Yorke & Bodenheimer (1999), but a brief overview is provided here as well. The standard equations of hydrodynamics including radiative transfer and the Poisson equation for the gravitational potential are solved on five regular nested grids of 68 by 68 cells. The grid does not resolve the central star, but the centermost grid cell is treated as a sink into which mass and angular momentum can flow. The stellar luminosity is calculated from the mass and mass accretion of this cell and the luminosity is used as a boundary condition for the radiative transfer calculations. The radiative transfer is solved using the frequency dependent flux-limited diffusion method (see Yorke & Bodenheimer 1999, for the details), in order to obtain a self-consistent temperature distribution. Artificial viscosity is included in order to deal with shocked regions and physical viscosity is provided by an α-prescription (Shakura & Sunyaev 1973) to include angular momentum transport in the disk.

We use the initial free fall time scale to describe the age of the simulated YSO. Free fall time is given as

$$t_{ff} = \sqrt{\frac{\pi^2 R^3}{8GM}}, \tag{3.1}$$

which for this particular model is approximately 1×10^5 years. The simulation can roughly be divided into three parts, namely the infall dominated pre-disk stage at 0.5 t_{ff}, the disk formation stage at about 1.0 t_{ff} in which both infall and rotation are important, and the rotation dominated disk growth stage at 2.0 t_{ff}. The entire simulation runs for about 2.5 t_{ff} at which point it halts. Representative snapshots of the density, temperature, and velocity structure at these three stages are shown in Fig. 3.1. In the three panels, the temperature and density contours are kept at the same values for comparison.

We have selected a number of snapshots throughout the simulation, 13 in total evenly spaced by about 0.2 in free-fall time, as input for our molecular excitation and frequency dependent radiation transfer code *RATRAN* (Hogerheijde & van der Tak 2000). This code runs on a similar, but coarser grid, so the density, temperature and velocities of the hydrodynamical simulation can directly be remapped onto a *RATRAN* grid. The level population in each cell is then solved iteratively by propagating photons randomly through the grid until the level populations are in equilibrium with the radiation field.
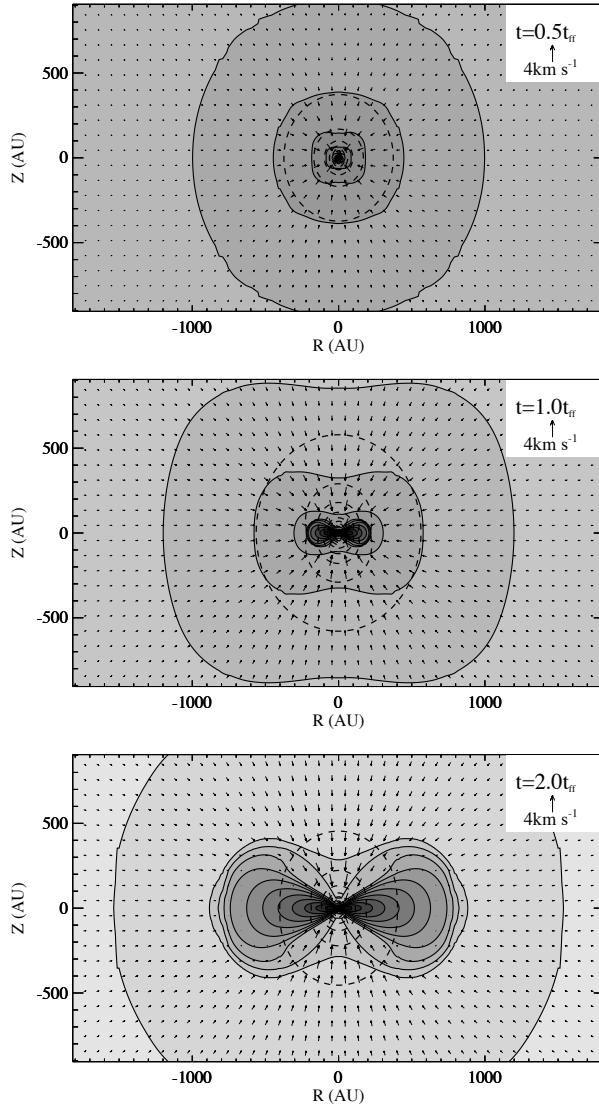
Figure 3.1: Model structure at three different ages. Full contours are the density starting at 3×10^5 cm^{-3} and increasing with $\log\rho = 0.5$. The temperature is shown as dashed contours, starting at 20 K and increasing with 10 K. The arrows show the infall component of the velocity field.

The reason why we do not use every snapshot (several hundreds, depending on the time resolution in the output) is that the molecular excitation calculations are quite time consuming. The CPU time required to determine the level populations for a single snapshot is comparable to the CPU time it takes to run the entire hydrodynamical simulation, which is the reason why such accurate radiation transfer methods are not included in the simulation itself. However, the level populations and hence the line profiles do not change dramatically from one time step to the next, so there is actually no need, for our purpose, to use more than one snapshot per $0.1 - 0.2$ t$_{ff}$.

In *RATRAN*, a molecular abundance is added to the model reflecting the chemical abundance of the molecule in question. The simplest possible abundance description uses a constant average abundance relative to the H$_2$ density which is how we populate the models with molecules in this work. More realistic abundance profiles, based on temperature and density dependent freeze-out and desorption rates, have been discussed by, e.g., Lee et al. (2004) and Jørgensen et al. (2004). In Sect. 3.5 we discuss the effects on our results, if a more realistic abundance distribution is added to the synthetic observations. We return to the subject of the inclusion of freeze-out in the hydrodynamical simulation and its effect on the resulting spectra in Chapter 5.

We execute separate *RATRAN* calculations for different molecular species. As mentioned above, these calculations are relatively time consuming, so we have chosen to focus on only three commonly observed molecules, CO, HCO$^+$, and CS, and their isotopologues. These three species probe different densities and have different optical depth and therefore the spectral profiles come out very different even for the same underlying snapshot. We can of course repeat the entire exercise for any molecule for which collisional rate coefficients are available and this makes our method very flexible. The collisional rate coefficients used in this thesis come from the *LAMDA* database[1] (Schöier et al. 2005). When the level populations have converged, the model is ray-traced in frequency bands around the desired transitions to obtain spectral image cubes from which spectral lines can be extracted. In the following we consider increasingly higher transitions for the three species, so that these not only probe increasingly higher densities but also increasingly higher temperatures.

We do not claim that this hydrodynamical collapse model provides a particularly realistic description of nature. Neither do we try to fit this model to observation, although in principle, the method presented in this chapter can be used to compare and constrain hydrodynamical models with molecular line observa-

---

[1]available at http://www.strw.leidenuniv.nl/~moldata

tions. Instead, we employ the simulation to provide a time resolved velocity field topology going from an infall dominated field to a rotation dominated field. The scope of this chapter is to show how the velocity field is reflected in the emission line profiles and to see to what extent the velocity field can be reconstructed from these lines. As long as the hydrodynamical simulation approximates reality, our method is valid. The two main caveats of our simulation are the lack of any kind of mass loss through either a wind or an outflow and the unknown initial condition for the angular momentum distribution. The lack of mass loss means that all the mass that is initially in the model ends up in either the disk or the star, and especially the disk ends up being very large and massive. An outflow would not only carry away mass but also angular momentum and the result of this would be a smaller, less massive disk. The effect of the second item, the initial angular momentum distribution is somewhat more uncertain and a point of further study, which however is beyond the scope of this study.

3.2.2 Parameterized model

We have chosen a particularly simple parameterization for the model which we use to derive the velocity field. This model is a simplified version of the one used in Chapter 2 to interpret single dish observations of the YSO L1489 IRS.

In this chapter we use a spherical version of this model, where both the density and the temperature are given by power-laws

$$n = n_0(r/r_0)^{-p}, \tag{3.2}$$
$$T = T_0(r/r_0)^{-q}, \tag{3.3}$$

which means that our parameterized model neglects the flattening of the disk. We assume that the inclination is known to at least 10-20%. Although our model is spherically symmetric, it still has a rotation axis, which may be inclined with respect to our line of sight. For the remainder of this chapter we adopt an edge-on view of the simulation (i=90°). The velocity field is described by two free parameters, the central mass M_* and an angle α, that is defined as,

$$\alpha = \arctan\left(\frac{v_r}{v_\phi}\right), \tag{3.4}$$

where v_r and v_ϕ are the free-fall and Keplerian velocity components, respectively, given by

$$v_\phi \cos(\alpha) = -\frac{v_r}{\sqrt{2}} \sin(\alpha) = \sqrt{\frac{GM_*}{r}}. \tag{3.5}$$

The angle α is thus the angle of the resulting velocity field vectors with respect to the azimuthal direction, and therefore the ratio of infall to rotation. In other words, if $\alpha = 0$ the cloud is in pure Keplerian motion whereas if $\alpha = \pi/2$ the cloud is collapsing in free fall. This parameterization is allowed because both rotation and infall have a $\sqrt{M_*/r}$ dependency.

The advantage of this simple parameterization is that it has few free parameters and, more importantly, for a large part of the hydrodynamical simulation the density and temperature are actually very well described by power-laws. The disadvantage is of course that it cannot describe the disk structure at all. However, since we are aiming at characterizing the velocity field, the exact shape and distribution of disk material is less important and it turns out that it has little impact on our result as long as we fit our density model to the mid-plane density of the hydrodynamical output.

The α parameter has no direct equivalent in the hydrodynamical simulation because the ratio of infall to rotation is not generally constant with radius. In the remainder of this chapter we do however use an averaged value for α where we have radially averaged the individual α values along the mid-plane in order to evaluate the quality of our results.

We assume that the inclination is known (we consider only the edge-on case, but our result holds true except for inclinations very close to face-on). In the beginning of the simulation, where rotation is less important, the inclination is harder to constrain observationally, but on the other hand, it does not really matter since the object is mostly spherical anyway. As soon as a disk has formed, the inclination can be constrained by modeling the SED or from near-infrared imaging. In any case, if the inclination is not known, it can in principle be included as a free parameter at the cost of computation time.

A final caveat of this simple model is the flat abundance distribution. As discussed above, the abundance distribution will evolve dynamically with the evolution of the temperature and density, and this will have an effect on the spectral lines. This effect can be taken into account in the modeling using the approach of Jørgensen et al. (2004), but for the sake of clarity we will disregard the chemistry in the main part of this chapter (see Chapter 5).

3.2.3   Obtaining the best fit

When fitting the parameterized model to the hydrodynamical solution, we do so in a sequence of comparisons between different synthetic observables. First we constrain the five parameters n_0, T_0, p, q, and R_{out} (R_{out} is the outer radius of the model beyond which the power-laws are truncated) in the density and temperature

model by fitting radial continuum profiles at 450 and 850 μm. A synthetic continuum image is calculated by *RATRAN* at each wavelength based on the hydrodynamical solution. Similarly we calculate images for the parameterized model that is then evaluated with respect to the image from the hydrodynamical solution by calculating the χ^2 measure. In other words, we obtain the set of parameters which gives the best representation of the hydrodynamical structure in the image space. The wavelengths and image resolution are chosen so that the images mimic real observations by instruments such as SCUBA on the James Clerk Maxwell Telescope (15 meter single dish, with a typical resolution of 15″, corresponding to ~2000 AU at the distance of the Taurus star forming region).

When the physical structure has been determined we fix the molecular abundance by fitting an emission line of an optically thin isotope. In the case of HCO$^+$, this isotope would for example be H^{13}CO$^+$, whereas for CO we could use C^{17}O. An optically thin line traces the total column density and can as such be used to derive the average abundance. Since we have not yet determined the velocity field, we aim at fitting the integrated intensity rather than the peak intensity or the line profile itself. The procedure is the same as before: A single spectrum towards the center is calculated by *RATRAN* based on the hydrodynamical solution which is then used as a synthetic observation to fit the same spectrum based on the parameterized model. Again, we use a spectral and spatial resolution which is typical for existing single dish telescopes (15″).

Finally, when the abundance is fixed, we fit the velocity field parameters. This is done by comparing optically thick lines. In the case where we simulate single dish observations, we use only a single spectrum towards the center of the object, in which case we fit only the central mass and a single angle α. If we use simulated interferometric observations, where there are typically several resolution elements across the object, we fit spectra which are separated by one synthesized beam, with as many corresponding angles α_i.

In order to fully explore the parameter space to reach the optimal solution, we use the genetic algorithm *PIKAIA* (Charbonneau 1995) which is a stochastic optimizer. This algorithm is applied in each step described above and is very successful in finding the true minimum of the search space. The benefit of using this algorithm for this purpose is that it takes a relative low number of model calculations to reach the optimal solution compared to the more traditional "brute force" method where a grid of models is calculated. Since calculating a model spectrum takes of the order of minutes to complete the applicability of our method is highly dependent of the number of models which are required to be calculated. Another benefit of using a code such as *PIKAIA* is that the entire parameter space gets well

sampled which enables us to determine the χ^2 distribution along each parameter axis. The resulting distributions are approximated by Gaussians, and the FWHM of these are used to get a handle on the robustness of the fit. It should be noted that this is not an error bar in the sense that our model fit is consistent with the synthetic data if it falls within the range of the FWHM of the Gaussian approximation to the χ^2 distribution. These numbers only show how sharply defined the minimum of the parameter space is for a specific optimization.

Figure 3.2 shows how well we are able to approximate the hydrodynamical solution by our simple parameterized model. The example shown is just a randomly chosen snapshot (t=1.0 t_{ff}).

3.3   Line profiles and the velocity field

Initially the cloud collapse model is given a solid body rotation. As gravitation sets in and infall velocity builds up towards free fall, matter is redistributed and so is the angular momentum. Material ends up in the plane of rotation, where it spins up, approaching the Keplerian velocity. At this point, the matter cannot be given a higher angular momentum, so as matter continuously moves inward from outside of the disk, angular momentum is transported outwards through the disk resulting in growth of the disk.

In Fig. 3.3 the radial and the azimuthal components of the velocity field in the disk mid-plane at a radius of 500 AU are plotted. Also shown in this plot are the free-fall and Keplerian velocities calculated as a function of the central core mass which grows in time as mass is being accreted onto the star. Initially, the radial velocity builds up faster than the azimuthal velocity component, but at an age of t=1.5 t_{ff} the disk expansion shock wave passes 500 AU and afterward the region is completely dominated by rotational velocity close to the Keplerian. Indeed the velocity is seen to be slightly super-Keplerian after the expansion wave passes because of the outwards angular momentum transport. Similarly, Fig. 3.4 shows again the infall and rotation velocity profiles, but for a single time slice (t=1.0 t_{ff}). In this figure, the velocities are plotted against the mid-plane radius and also shown are the free-fall and Keplarian profiles, indicated by thin lines. The disk radius is clearly seen by the break in the infall profile around 200 AU. It is also seen that the velocity field is very well approximated by free-fall outside of the disk radius, whereas the inside of the disk radius is well described by Keplerian motion.

The velocity of the gas is reflected in the shape of the emission line profiles. This includes both the random particle motion and the systematic motion due to
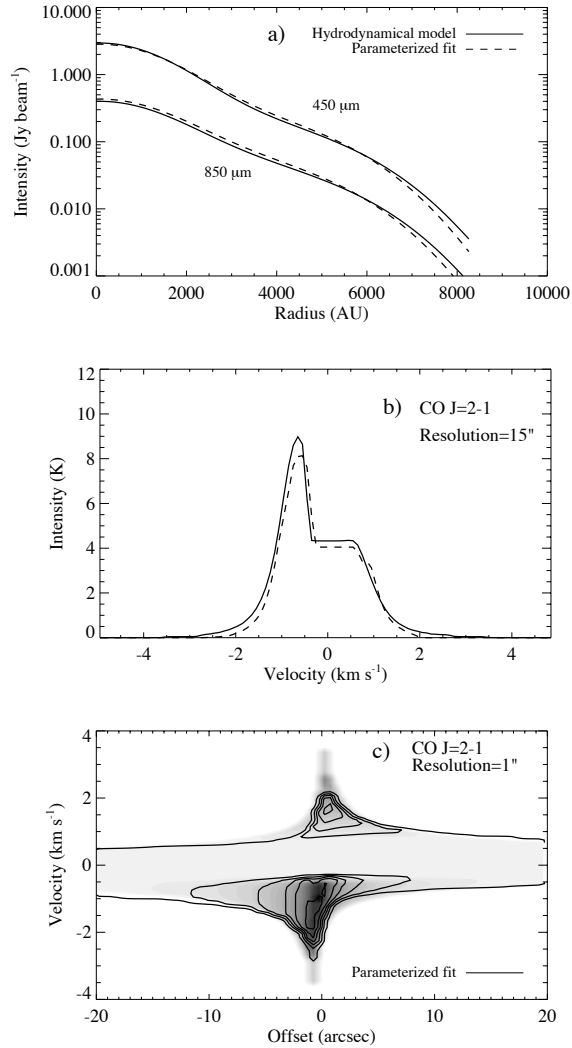
Figure 3.2: Example of a fit by our parameterized model to the hydrodynamical solution at t=1.0 t$_{ff}$ for the case of CO. The full lines are the output of the hydrodynamical simulation and the dashed lines are the fit by our parameterized model. In panel **c)**, the hydrodynamical output is shown by the grey scale and the model fit by contour lines.
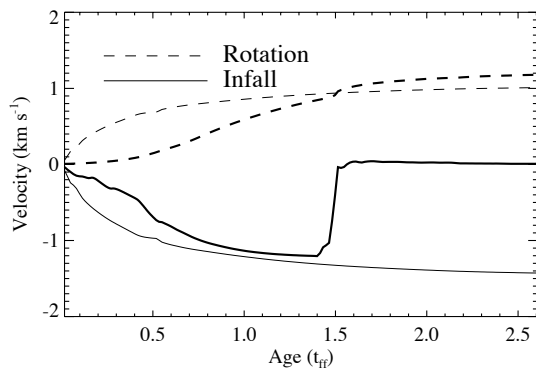
Figure 3.3: The rotation and infall velocities of the collapse simulation in the midplane at a radius of 500 AU plotted as a function of free-fall time. The velocities of the simulation are shown in thick lines. In this figure we also show the Keplerian and free-fall velocities which are both functions of the central mass. These are shown as thin lines.
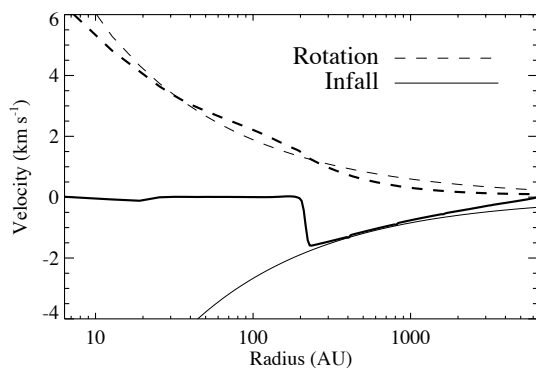
Figure 3.4: The rotation and infall velocities in the simulation along the midplane at an age of t=1.0 t_{ff}. As in Fig. 3.3, the thin lines correspond to free-fall and Keplerian velocity profiles.

potential gradients. For the model cloud considered here, the former is of minor importance although we do include a microturbulent field with a Gaussian FWHM of 0.2 km s^{-1} in our calculations. The systematic motion is of course our main interest here, because this is what governs the dynamics of the cloud.

Initially, the cloud is collapsing in a nearly spherically symmetric way which is entirely dominated by radial motions. This should be reflected in the line profiles as the characteristic infall asymmetry. In the case of optically thick lines, the difference in temperature of the red shifted and the blue shifted peaks provides a measure of the optical depths (e.g., Evans 1999). In the latest stage, when most of the gas has been accreted onto the disk which is dominated by rotation, the line profiles are expected to be double peaked, with both peaks having the same intensity. At this point, gas has reached such a low density outside of the disk, that we do not expect to see any contribution to the line from radial motions. In the intermediate stage however, where the disk is still accreting significantly, both velocity components, radial and azimuthal, will contribute to the spectral line profile. The exact shape of such a profile is hard to predict because it is critically dependent on the exact optical depth, the critical density of the transition, the spatial resolution, and the system inclination. This is further complicated by the fact that no analytical model exists of the transition from a collapsing envelope to a viscously supported protoplanetary disk.

As an illustration, we show model spectra in Fig. 3.5 which have been calculated with a model which is either in free fall (with no azimuthal velocity component at all) or in Keplerian rotation (no radial components). The top-most panels in this figure show the infalling models in which the infall-asymmetry (Evans 1999) is clearly seen. The corresponding position-velocity (PV) diagram also resembles the CO 2–1 at t=0.5t$_{ff}$ panel in Fig. 3.8. Similarly, the PV-diagram in the lower row of Fig. 3.5 resembles the late stage PV-diagram in Fig. 3.8 and the low-resolution spectrum shows the double-peak feature which is associated with rotation. Therefore, if the gas has the particular density in which an observed transition is strongly dominated by one or the other type of motion, it is possible to tell the difference from the shape of the line or the intensity distribution of the PV-diagram. This, however is rarely the case because the velocity field in general changes with increasing density (due to angular momentum conservation) and in most cases, the gas has non-vanishing velocity components in all three spatial directions.
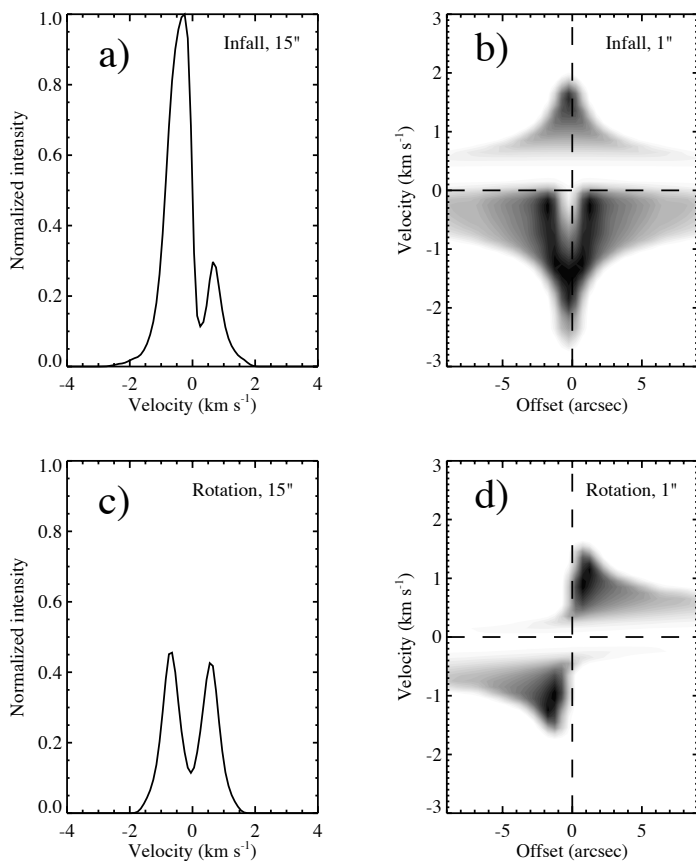
Figure 3.5: Low-resolution spectra and high-resolution position-velocity diagrams of a purely (free) infalling model and a purely (Keplerian) rotating model.
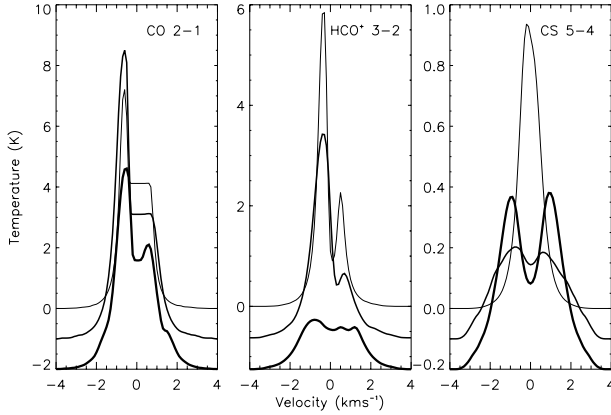
Figure 3.6: Spectral line profiles of the hydrodynamical simulation of three different tracers at t=0.5 t_{ff}, 1.0 t_{ff}, and 2.0 t_{ff} with increasing line thickness. 1.0 t_{ff} and 2.0 t_{ff} are offset by −10% and −20% respectively. These spectra have been convolved with a 15″ Gaussian beam to resemble typical single-dish telescope observations.

3.3.1   Low resolution spectra

Using our hydrodynamical simulation as input model we can calculate spectra of any disk and envelope configuration ranging from purely collapsing to entirely rotating. Figure 3.6 shows the result of such a calculation. These spectra are convolved with a 15″ FWHM Gaussian beam so that they are comparable to observed spectra obtained with a typical large single dish telescope. The system inclination has been chosen to be exactly edge-on so that the viewing angle is the same as in Fig. 3.1.

In the leftmost panel of Fig. 3.6 are shown CO J = 2–1 spectra based on the three time snapshots from Fig. 3.1. The CO lines are seen to be very optically thick throughout the simulation which is a result of the relatively high CO abundance. Actually, the optical depth of the CO lines is so high that we do not even see the rotating disk in the last snapshot, where the profile still bears the typical infall signature also seen in the two earlier snapshots. Even though the densities are very low (< 10^4 cm^{-3}) outside of the disk at t=2.0 t_{ff}, there is still enough column to entirely mask the disk. In the middle panel, HCO$^+$ J = 3–2 spectra are shown. These are optically thick too, but not as much as the CO lines. The infall

asymmetry is very pronounced in the t=0.5 t_{ff} spectrum and is still visible in the t=1.0 t_{ff}. In the last snapshot, the infall signature is gone, and we only see a flattened Gaussian-like spectrum. In the right-most panel of Fig. 3.6 we have plotted CS $J = 5$–4. This line traces very high densities ($> 10^6$ cm^{-3}). Notice that the intensities of these lines are about an order of magnitude lower than the intensity of the CO lines. In the earliest snapshot, this transition is actually optically thin and only a hint of asymmetry is seen here. As we go to later stages, the CS lines also start to become optically thick. This line, however, clearly displays a double peaked profile in the late stage. We also see, contrary to the CO and HCO$^+$ lines that the width of the CS spectra increases with time.

To illustrate how the shape of the line profile is a reflection of the underlying velocity field, we have quantified the line asymmetry by measuring the intensity difference between the two peaks, normalized with the peak intensity of the line. This gives us a dimensionless number between 0 and 1, where 0 corresponds to the extreme asymmetric line and 1 is a perfectly symmetric line. We have plotted this quantity for the whole time series of model spectra of CO, HCO$^+$, and CS in Fig. 3.7. These line asymmetries are plotted as dotted lines. The full line in Fig. 3.7 is the radially averaged angle α from the hydrodynamical simulation as calculated by Eq. 3.4. The Pearson correlation coefficients between α and line profile asymmetry are 22%, 61%, and 83% for CO, HCO$^+$, and CS, respectively, meaning that the asymmetry of the CS lines is a quite well correlated with the ratio of infall to rotation. Similarly, the central stellar mass (as given by the hydrodynamical simulation) can be correlated with the FWHM of the lines, resulting in correlation coefficients of 96%, 63%, and 89% respectively; also a very high degree of correlation.

3.3.2 High resolution spectra

With the use of present day and future sub-millimeter interferometers, it is possible to obtain spatially resolved observations of protostellar cores and protoplanetary disks. Using these kind of instruments, resolutions of 1″ or better are possible. When a resolved spectral image cube is available, it is possible to plot the velocity off-set as a function of projected radius by contouring the measured intensity in position-velocity space. Figure 3.8 shows PV-diagrams of three time snapshots of each of the three transitions: CO 2–1, HCO$^+$ 3–2, and CS 5–4. As in Fig. 3.6 we see a clear evolution in these diagrams, both in time and with increasing excitation energy. In the earliest snapshot, there is emission in almost equal amounts in all four quadrants, whereas in the latest snapshot, and most pronounced in the CS transition, the emission contours are butterfly-shaped and
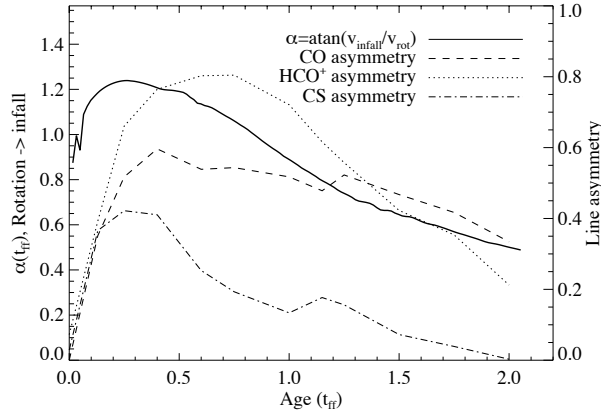
Figure 3.7: The averaged α from the hydrodynamical simulation plotted against free-fall time (thick solid line). The punctured lines show the dimensionless asymmetry of the single-dish spectral lines as a function of time.

confined to the first and third quadrants. The former is typical for radial motion only while the latter is associated with rotation.

Although it is to some extent possible to characterize the velocity field that results in a particular PV-diagram, it is clear from the $t=1.0t_{ff}$ panels in Fig. 3.8 that the answer one gets depends on the molecule in consideration. At $t=1.0t_{ff}$ one would conclude from the CO transition that the cloud is contracting whereas from CS the conclusion would be more or less pure rotation. The reason for this is that these two transitions are excited at different densities and therefore, the PV-diagram shows the dominating velocity structure in different regions. This is of course no different from the single-dish spectra (Fig. 3.6), except that the effect is much clearer in PV-space.

3.4 Results

3.4.1 Single-dish simulations

In Fig. 3.9 we present the results of our model fit to the spectra from the hydrodynamical simulation using a single spectrum obtained towards the center of the source in a resolution of 15″. This figure shows the best fit mass (top) and α (bottom) parameters for the three chosen transitions separately, and for a joint fit to all
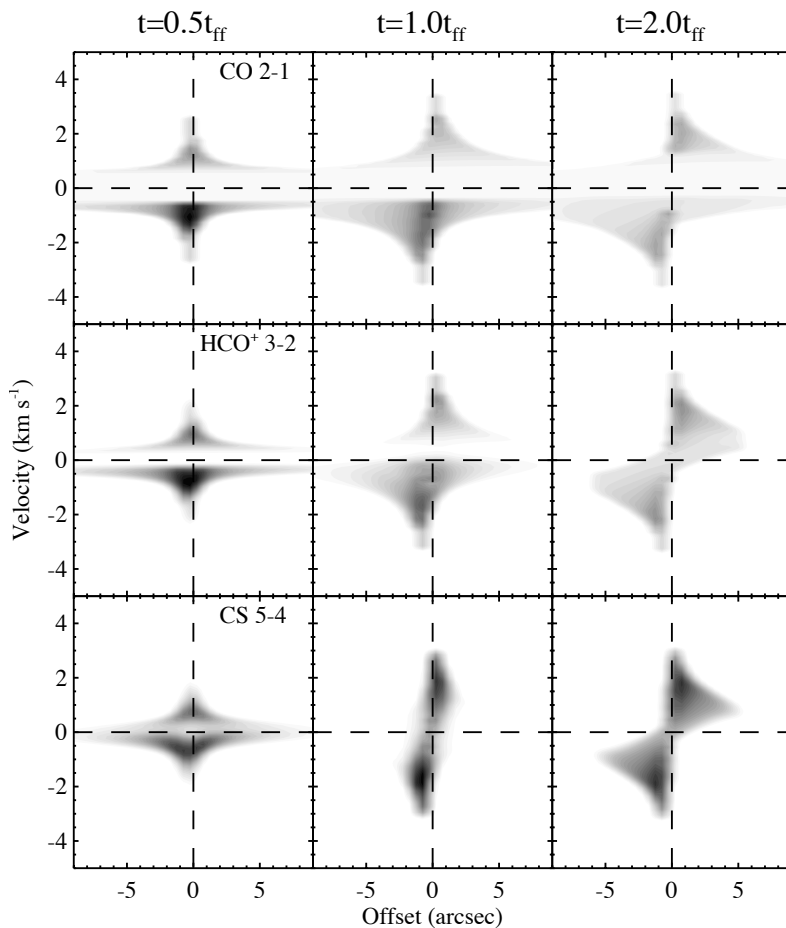
Figure 3.8: High resolution position-velocity diagrams of CO 2–1, HCO$^+$ 3–2, and CS 5–4 at three different stages of the collapse simulation. These spectra have been convolved with a 1$''$ FWHM Gaussian beam so that the resolution in these diagrams is comparable to the typical sub-millimeter interferometer resolution.

three lines simultaneously. First of all we notice that after about 1.0 free-fall time, HCO$^+$ and CS fail to converge, that is, the model line profile carries no resemblance to the line calculated from the hydrodynamical snapshot. However, in the case of the mass parameter, for the snapshots earlier than the 1.0 free-fall time as well as for the entire sequence of CO spectra, we actually get rather accurate parameter values, although we do consistently underestimate the mass for t<1.0 t_{ff}. The error bars or robustness of the fit becomes significantly worse towards the end of the sequence for the mass determination using CO, but the actual best fit value is close to the correct value. The situation is more complicated if we consider the α parameter. Here the CS does not show any consistency at any point throughout the sequence. CO and HCO$^+$ are considerably better, but the best overall fit is provided by the case where all three lines are fit at the same time.

Generally we see that fitting all three lines at the same time does not give a much better fit than the best single transition provides, in this case the CO line. The fact that CO seems to be the best choice in order to accurately describe the velocity field using single-dish observations is somewhat contradictory to the result of the correlation calculations in sect. 3.3.1, where the CO profile was seen to be the least correlated with the velocity field. According to those numbers, HCO$^+$ and CS should be able to give much more accurate results the CO.

The problem is that when using tracers that probe much deeper into the envelope we start to probe into the regions where our simplified spherical model no longer gives an accurate description. Because we use an average density profile in order to reproduce the total cloud mass, we automatically get lower column densities in the disk region, and this means that lines can get optically thick in the hydrodynamical simulation but not in our parameterized model. This is the reason why the CS and HCO$^+$ lines are no longer reproducible at t>1.0 t_{ff}. Furthermore, in the early snapshots, CS is optically thin and the line has thus little structure, which makes it difficult to accurately fix α.

Interestingly, it seems that a low density tracer such as CO gives the most accurate description of the velocity field even though the CO line never actually shows any rotational characteristics (e.g., compare the CO profile at t=2.0t_{ff} in Fig. 3.6 to the lower left panel of Fig. 3.5), mainly because CO gets optically thick at radii larger than the outer disk radius. Another advantage of using CO as tracer is that it is less affected by the depletion that occurs in the high density (disk) regions because it gets optically thick further out. High density tracers such as HCO$^+$ and especially CS probe into the region where freeze-out is significant which makes the whole process considerably more complicated. On the other hand, because CO is excited at low densities and temperatures, the spectrum has
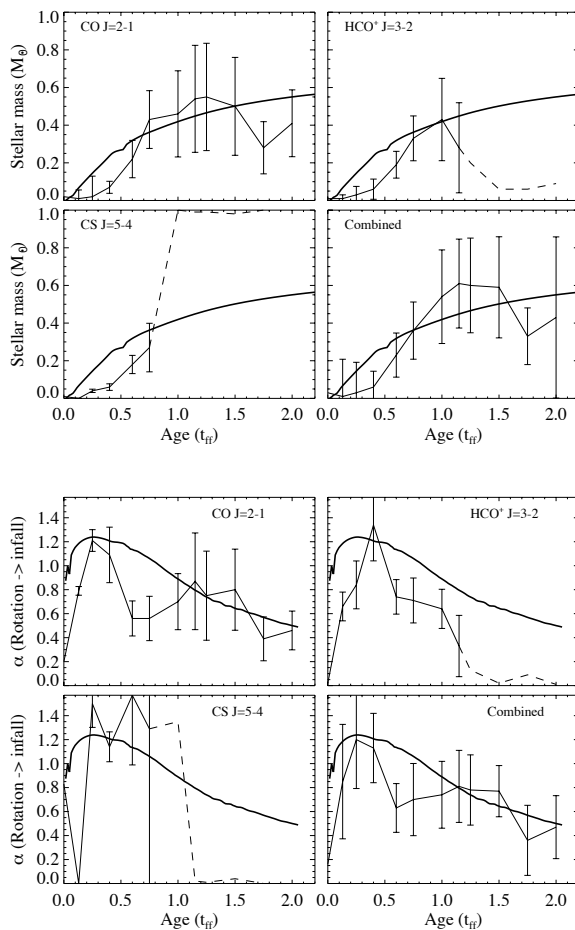
Figure 3.9: The result of low-resolution model fits to spectra based on the hydrodynamical simulation. The four upper panels show the best fit value for the central mass based on CO, HCO$^+$, and CS spectra as well as a fit using all three lines simultaneously. The thick solid line is the value from the hydrodynamical simulation and the thin lines connect the best fit values. The error bars are the width of the χ^2 distributions as discussed in sect. 3.2.3. Dashed lines denote unconverged models, i.e., cases where the line profile cannot be reproduced by our model. The four panels below are similar, but for the velocity angle α in radians as defined by Eq. 3.4.

a much higher chance of being polluted by emission from ambient material and outflows. This can be hard to identify and if present must be accounted for in the modeling. Also, although CO is the best candidate of the three tracers shown here, the correlation between the derived velocity field and the real velocity field is actually not very high, with most of the points lying between 0.6 and 0.8 ($\approx 45°$).

3.4.2 Interferometric simulations

We now turn to the high-resolution situation, where we use the PV-diagram to constrain the velocity field parameters. Because the PV-diagram is a two dimensional intensity distribution, comparing model to data is not as straight-forward as in the case of using a single spectrum, because there are several ways to evaluate a fit in PV-space.

The obvious method is to evaluate the fit by comparing the model PV-diagram to the data, pixel by pixel. While this works reasonably well when using synthetic, noiseless data which are perfectly aligned with the coordinate axes, it may prove very difficult and unreliable using real data, where the position angle may not be perfectly well determined. Also, if the model is not describing the source geometry very well, especially on small scales, a pixel by pixel comparison can easily result in a poor fit, although the velocity model is actually quite accurate. Nevertheless, we have tried using this method, just to see how well it works, when noise is not present.

Another way to obtain a fit is to determine the position of the two maxima of the intensity distribution (the blue peak and the red peak) and then use the straight line between these two points as a measure. This line is characterized by three numbers: its length, slope, and orientation in PV-space. This method is better when using real data because it works even if the data are quite noisy. Unfortunately, the minimum in χ^2-space is less well-defined (the fitness landscape is more shallow) using this method, because of the degeneracies occurring when using just a linear gradient to evaluate the fit and therefore, in most cases, the error bars are quite large.

A third method that we have tried to use is the asymmetry in the PV-diagram as a constraint. We do this by summing up the emission in each of the four quadrants and then evaluate the fit by comparing the ratio of emission in quadrant 1 and 4 to the emission in quadrant 2 and 3 as well as the ratio of emission in 1 and 2 to 3 and 4. In other words, we measure the left/right and top/bottom asymmetry in the PV-diagram. This method has the disadvantage that it results in a diagonal ridge in χ^2-space, and thus a further constraint is needed. To solve this degeneracy, we use a single-dish line. However, using the entire single-dish line profile together
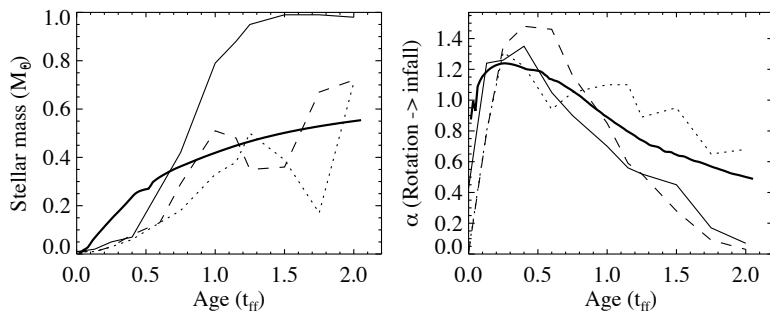
Figure 3.10: Similar to Fig. 3.9, but for HCO$^+$ 3–2 at a resolution of 1″, using the PV-diagram to evaluate the χ^2. The three thin line styles correspond to three different methods to evaluate the χ^2. The full line corresponds to fitting the PV-diagram pixel by pixel, the dashed line is the fit obtained from a linear gradient in PV-space, and the dotted line is the combination of using the PV-diagram and a single-dish line.

with the PV-diagram results again in a shallow fitness landscape which we are not interested in. On the other hand, we only need to constrain one parameter with the single-dish line to resolve the degeneracy, and therefore we mask the center part of the line and only fit the line wings. We mask out all channels which lie within the FWHM of the line and use the remainder to calculate a χ^2 value which is then added to the χ^2 value we get from the PV-diagram.

The result of these three methods is shown in Fig. 3.10. The three thin lines correspond to the three methods described above, with the pixel by pixel method plotted as the full line, the linear gradient as the dashed line and the emission asymmetry together with the single-dish line wings as the dotted line. The three methods more or less agree on the results, except for the mass parameter using the pixel by pixel comparison, which diverges after about 0.5 free-fall times. The main difference between the three methods is the size of the error bars (not shown in Fig. 3.10), which varies quite dramatically, not only from one method to the other, but also from snapshot to snapshot with the same method. Generally, the third method described above gives the smallest errors, except for a few of the earlier snapshots where the linear gradient has a better defined minimum in χ^2-space.

Because each of our methods comes with an estimate of how well defined the fit is, for each snapshot we can select the method that is most discriminating. This
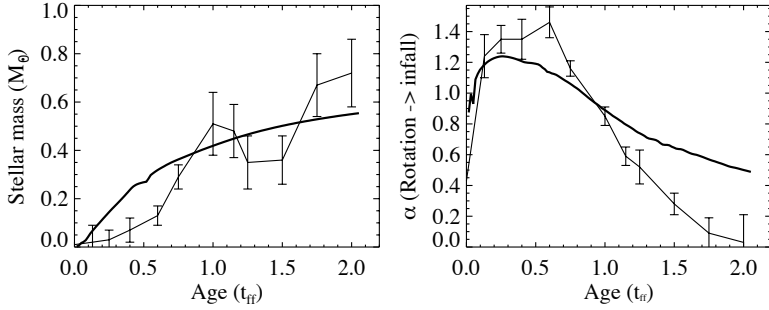
Figure 3.11: High-resolution model fit, similar to that of Fig. 3.10. Each point shown here together with its associated error bar has been picked among the three different solutions shown in Fig. 3.10 using the smallest error bar as selection criterion.

is shown in Fig. 3.11, together with the corresponding error bars. The resulting curve describes the parameters of the hydrodynamical simulation far better than the case of the single-dish result and also better than any of the three methods individually shown in Fig. 3.10. The error bars are also very small in almost all of the snapshots which means that the fits are very robust or in other words, we can always find a method that gives us acceptable small error bars. The main deviation in Fig. 3.11 is the α-parameter in the later part of the collapse. Here, our model overestimates the amount of rotation, near the end by a factor of 10. However, the graph has a very smooth behavior compared to the best result of the single-dish lines, where the solution fluctuates around the correct values. Also, the error bars are very small, compared to those of the single-dish result, and this means that it should be possible to determine relative ages in a sample of objects using the same approach as the one we used to obtain the result in Fig. 3.11, even though the actual absolute value derived for α is incorrect.

3.5 Discussion

The above analysis has been made using synthetic data which in many respects are unrealistic in the sense that they are noiseless and uncontaminated by fore- or background material. Furthermore we have disregarded the chemistry, using a constant abundance distribution instead. In the following we will discuss the effect on our result that using real data will have.

As mentioned in Sect 3.2, freeze-out chemistry is important in YSOs (Aikawa & Herbst 2001; Bacmann et al. 2002) and this is likely what causes the most concern with respect to our results. Freeze-out occurs in regions of high density and low temperature, a condition which is present in the outer parts of the disk and inner parts of the envelope before the protostar begins to heat up. As the molecules freeze out onto grain surfaces, they no longer contribute to the radiation field of the rotational transitions, and if the gas in the entire disk is frozen out we do not see any rotational motion at all. There is no doubt that YSOs in general are affected by some freeze-out, but the question is to what extent this freeze-out affects the spectra.

In Chapter 5 a realistic freeze-out model has been added to the hydrodynamical simulation presented in this chapter, in order to get time-resolved abundance profiles. In Chapter 5 only the CO molecule is considered, but the result may be generalized to include at least also HCO^+ because the chemistry of this molecule follows that of CO closely. The main result of Chapter 5 is that the optically thick spectra are not much affected throughout the simulation. Freeze-out occurs mainly beyond the $\tau=3$ isosurface of ^{12}CO. This is interesting since the $\tau=3$ surface is located at the same physical radius no matter whether there is freeze-out within this radius or not. This means that in our models too, we never actually probe the disk regions directly, and thus we conclude that when we seem to measure rotation, we are actually rather measuring lack of infall.

On the other hand, optically thin lines are quite strongly affected by the freeze-out zones, because these lines probe the full column density. In Sect. 3.2 we described how we use an optically thin isotopologue to determine the average abundance, and therefore a change in an optically thin line due to freeze-out will cause a wrong abundance determination which will then propagate to the optically thick lines that are used to obtain the velocity field. If freeze-out is present in the data, we can either still try to fit it with a constant abundance profile or we can add a simple parameterized freeze-out model, following the approach of Jørgensen et al. (2005b). In the former situation we derive an average abundance which is about a factor of two lower than the correct value for the undepleted zones, whereas if we allow for freeze-out in our model as well, we derive a gas-phase abundance which is about 20% lower than the correct abundance. This should be compared with the situation described in Sect. 3.2 where we had no freeze-out and we were able to derive the abundance to within 1%. However, underestimating the abundance by a factor of 2 does not make a big difference for the continued analysis and therefore it should be safe to use a flat abundance distribution in the model, even though the object in question is known to have depletion zones. It

is of course also always possible to take a non-constant abundance profile into consideration when modeling sources for which the chemistry is already known (e.g., as in the case of NGC1333-IRAS2, Jørgensen et al. 2005a).

Another source of confusion is possible contamination from foreground material (Boogert et al. 2002), ambient cloud material or outflows (Bally & Lada 1983). Because larger scale mapping can identify the former two, only the outflows are a matter of real concern. Outflow emission shows up as a broadening and enhancement of the line wings and, if present, is typically seen in tracers such as CO and HCO^+. Only single-dish lines are really affected by these effects, because interferometers typically resolve out large scale structure, such as ambient cloud material, and outflow regions are easily identifiable and can be masked when making the PV-diagram. Foreground material is less of a concern if HCO^+ is used, because this molecule is only excited at densities higher than what is typical for diffuse interstellar foreground layers. For single-dish lines, ambient material may shown up as excess emission near the line center which makes it impossible to use the line profile to trace the velocity field. If, however, only the line wings are used, ambient or foreground material should not be a problem. We are thus left with the outflow contamination of the single-dish lines, which mainly affect the line wings.

If a source is known to drive a strong outflow, or if inconsistent results are obtained when fitting the model with and without the use of a single-dish line, it is necessary to either use a different single-dish line that is less affected by the outflow or simply to avoid using single-dish lines for that particular source. This may result in a less strict result, but there is no way to reliably remove the contribution of an outflow from a spectral line unless the central mass and to some extent also the velocity field (and thus the shape of the line wing) are already known.

Finally, real data are noisy and this may cause confusion when fitting the single-dish lines. As was mentioned above, using a linear gradient or comparing the total emission in the four quadrants of the PV-diagram is little affected by the presence of noise. However, for the single-dish data it is important to use strong lines (CO and HCO^+ are almost always strong) and integrate long enough so that the line wings have good signal-to-noise. If this is not possible, it is again simply a matter of using the PV-diagram without the constraint of a single-dish line, at the price of a less certain result.

3.6   Conclusion

We have explored the possibility of placing young stellar objects in an evolutionary ordering based on their kinematical configurations by fitting a simple parameterized model to sub-millimeter observations. We have tested the feasibility of this by fitting the simple velocity model to a time series of synthetic observations with known velocity fields, generated by a hydrodynamical simulation. We find that the model reproduces the synthetic spectra reasonably well and that the best fit parameters which describe the velocity field are in agreement with the velocity field in the hydrodynamical simulation. We therefore conclude that it is possible to extract reliable information on astronomical objects if we replace the synthetic spectra with real observations.

We find that it is difficult, though not impossible, using single-dish data alone, due to the shallowness of the χ^2-space, but feasible if interferometric data are used, especially when combined with one or more single-dish lines. Using the latter option, we find that the central dynamical mass can be determined to within 20%. However, we have not been able to establish a single "best way" to obtain the parameters throughout the collapse. We find that the best result is obtained by trying several different methods to constrain the fits, and then pick the result of the one which shows the most peaked χ^2-space. That said, most of our best constrained points were obtained using a combination of low-resolution and high-resolution and this is the preferred starting point.

We further conclude that the molecular species used are not crucial for the result, as long as the line wings are clearly defined and uncontaminated in the case of the single-dish lines, and also that the transition is optically thick. For the high-resolution data, signal-to-noise is the main concern, so strong lines are preferred (CO, HCO^+, etc.).

Due to the uncertainty of the absolute time scale of the collapse calculated by our relative simple hydrodynamical simulation, we cannot yet establish an absolute age of a given object, but relative ages among a sample of objects can be obtained, provided that the velocity field of a collapsing cloud evolves similar to that of the simulation. Indeed, if an age calibration could be made, for example using the abundance profile of one or more objects, this could prove a powerful method to place a large number of young stars in an evolutionary sequence, because of the relatively straight-forward observations needed to perform the analysis. The hydrodynamical simulation presented in this chapter is not required in order to analyze real objects. However, with an improved and more realistic hydrodynamical scheme, it might be possible to calibrate the evolution of the velocity field so that an absolute time scale of star formation can be established.

Acknowledgements

References

Aikawa, Y. & Herbst, E. 2001, A&A, 371, 1107

Bacmann, A., Lefloch, B., Ceccarelli, C., et al. 2002, A&A, 389, L6

Bally, J. & Lada, C. J. 1983, ApJ, 265, 824

Basu, S. 1998, ApJ, 509, 229

Belloche, A., André, P., Despois, D., & Blinder, S. 2002, A&A, 393, 927

Bodenheimer, P., Yorke, H. W., Rozyczka, M., & Tohline, J. E. 1990, ApJ, 355, 651

Boogert, A. C. A., Hogerheijde, M. R., Ceccarelli, C., et al. 2002, ApJ, 570, 708

Calvet, N. & Hartmann, L. 1992, ApJ, 386, 239

Cassen, P. & Moosman, A. 1981, Icarus, 48, 353

Charbonneau, P. 1995, ApJS, 101, 309

Evans, II, N. J. 1999, ARA&A, 37, 311

Gregersen, E. M. & Evans, N. J. 2000, ApJ, 538, 260

Hogerheijde, M. R. 2001, ApJ, 553, 618

Hogerheijde, M. R. & van der Tak, F. F. S. 2000, A&A, 362, 697

Jørgensen, J. K., Bourke, T. L., Myers, P. C., et al. 2005a, ApJ, 632, 973

Jørgensen, J. K., Schöier, F. L., & van Dishoeck, E. F. 2004, A&A, 416, 603

Jørgensen, J. K., Schöier, F. L., & van Dishoeck, E. F. 2005b, A&A, 435, 177

Keto, E. R. 1990, ApJ, 355, 190

Lada, C. J. & Wilking, B. A. 1984, ApJ, 287, 610

Lee, J.-E., Bergin, E. A., & Evans, II, N. J. 2004, ApJ, 617, 360

Lommen, D., Jørgensen, J. K., van Dishoeck, E. F., & Crapsi, A. 2008, A&A, 481, 141

Mardones, D., Myers, P. C., Tafalla, M., et al. 1997, ApJ, 489, 719

Myers, P. C., Mardones, D., Tafalla, M., Williams, J. P., & Wilner, D. J. 1996, ApJ, 465, L133

Ohashi, N., Hayashi, M., Ho, P. T. P., & Momose, M. 1997, ApJ, 475, 211

Różyczka, M. 1985, A&A, 143, 59

Saito, M., Kawabe, R., Kitamura, Y., & Sunada, K. 1996, ApJ, 473, 464

Schöier, F. L., van der Tak, F. F. S., van Dishoeck, E. F., & Black, J. H. 2005, A&A, 432, 369

Shakura, N. I. & Sunyaev, R. A. 1973, A&A, 24, 337

Shu, F. H. 1977, ApJ, 214, 488

Terebey, S., Shu, F. H., & Cassen, P. 1984, ApJ, 286, 529

Ulrich, R. K. 1976, ApJ, 210, 377

van Langevelde, H. J., van Dishoeck, E. F., & Blake, G. A. 1994, ApJ, 425, L45

Yorke, H. W. & Bodenheimer, P. 1999, ApJ, 525, 330

Yorke, H. W., Bodenheimer, P., & Laughlin, G. 1993, ApJ, 411, 274

Yorke, H. W., Bodenheimer, P., & Laughlin, G. 1995, ApJ, 443, 199

Chapter 4

A deeply embedded young protoplanetary disk around L1489 IRS observed by the Submillimeter Array

Abstract

Circumstellar disks are expected to form early in the process that leads to the formation of a young star, during the collapse of the dense molecular cloud core. Currently, it is not well understood at what stage of the collapse the disk is formed or how it subsequently evolves. We aim to identify whether an embedded Keplerian protoplanetary disk resides in the L1489 IRS system. Given the amount of envelope material still present, such a disk would respresent a very young example of a protoplanetary disk. Using the Submillimeter Array we have observed the HCO^+ $J = 3–2$ line with a resolution of about $1''$. At this resolution a protoplanetary disk with a radius of a few hundred AUs should be detectable, if present. Radiative transfer tools are used to model the emission from both continuum and line data. We find that these data are consistent with theoretical models of a collapsing envelope and Keplerian circumstellar disk. Models reproducing both the spectral energy distribution and the interferometric continuum observations reveal that the disk is inclined by $40°$, which is significantly different to the surrounding envelope ($74°$). This misalignment of the angular momentum axes may be caused by a gradient within the angular momentum in the parental cloud, or if L1489 IRS is a binary system rather than just a single star. In the latter case, future observations looking for variability at sub-arcsecond scales may be able to constrain these dynamical variations directly. However, if stars form from turbulent cores, the accreting material will not have a constant angular momentum axis (although the average is well defined and conserved), in which case it is more likely to have a misalignment of the angular momentum axes of the disk and the envelope.

Christian Brinch, Antonio Crapsi, Jes K. Jørgensen, Michiel R. Hogerheijde, and Tracey Hill

4.1   Introduction

Circumstellar disks constitute an integral part in the formation of low-mass pro-
tostars, being a direct result of the collapse of rotating molecular cloud cores and
the likely birthplace of future planetary systems. When a molecular cloud core
collapses to form a low-mass star, its initial angular momentum causes material to
pile up to form a circumstellar disk of the size of ~ 100 AU. (Cassen & Moosman
1981; Terebey et al. 1984; Adams et al. 1987, 1988). Due to accretion processes as
the young stellar object (YSO) evolves, the disk grows in size while the envelope
dissipates (e.g., Basu 1998; Yorke & Bodenheimer 1999). In the more evolved
stages of YSOs, such disks can be imaged directly at optical and near-infrared
wavelengths (e.g., Burrows et al. 1996; Padgett et al. 1999) and their chemical
and dynamical properties can be derived from comparison to submillimeter spec-
troscopic observations (e.g., Thi et al. 2001). Still, this latter method is often not
unique, but requires *a priori* assumptions about the underlying disk structure. In
the earlier embedded stages this method is even more complex, because the disk is
still deeply embedded in cloud material so that any signature of rotation in the disk
itself, for example, is smeared out by emission that originates in the still collaps-
ing envelope. By going to higher resolution using interferometric observations, as
well as observing high density gas tracers, more reliable detections of protoplane-
tary disks can be made as direct imaging is approached (Rodríguez et al. 1998; Qi
et al. 2004; Jørgensen et al. 2005b). In this chapter we present such high-angular
resolution submillimeter wavelength observations from the Submillimeter Array
(SMA) of the embedded YSO L1489 IRS. We show how these observations place
strong constraints on its dynamical structure and evolutionary status through de-
tailed modeling.

   L1489 IRS (IRAS 04016+2610) is an intriguing protostar in the Taurus star
forming region (d = 140 pc), classified as a Class I YSO according to the classi-
fication scheme of Lada & Wilking (1984). It is still embedded in a large amount
of envelope material, in which a significant amount of both infall and rotation
has been observed on scales ranging from a few tenths of an AU out to several
thousands of AUs (Hogerheijde 2001; Boogert et al. 2002). This large degree
of rotation makes this source an interesting case study for the evolution of an-
gular momentum during the formation of low-mass stars, potentially linking the
embedded (Class 0 and I) and revealed (Class II and III) stages.

   In Chapter 2, a model of L1489 IRS was presented based on data from a
large single-dish molecular line survey (Jørgensen et al. 2004). This study was
motivated by the intriguing peculiarities seen in L1489 IRS, such as the unusual
large size and shape of the circumstellar material. The aim was to constrain the

structure of its larger-scale infalling envelope and to place it in the right context of the canonical picture of low-mass star formation (see for example several reviews in Reipurth et al. 2007).

The model presented in Chapter 2 described a flattened envelope with an inspiraling velocity field, parameterized by the stellar mass and the (constant) angle of the field lines with respect to the azimuthal direction. A spherical temperature profile was adopted and the model did not explicitly contain a disk. The mass of the envelope was 0.09 $M_{\odot}$, adopted from Jørgensen et al. (2002). The use of such a "global" model is sufficient when working with single-dish data, where the emission is dominated by the emission from the large-scale envelope. With this description it was possible to accurately reproduce all the observed single-dish lines.

What the study of Chapter 2 could not address is whether a rotationally dominated disk is present, with a size of the order of hundreds of AUs, although the amount of rotation that is inferred by the single-dish observations certainly suggests that a disk should have formed. In addition, two specific puzzles remain regarding the structure of L1489 IRS, inferred on the basis of the model when compared to other studies in the literature. First, the best fit was obtained with a central mass of 1.35 $M_{\odot}$, which is a very high value given that the luminosity of the star has been determined to be only 3.7 $L_{\odot}$ (Kenyon et al. 1993). Second, it was found that the best fit inclination of the system was 74°. This is in agreement with the result from Hogerheijde (2001), where they showed that in order to reproduce the observed aspect ratio, the inclination cannot be less than 60°. However, in a recent study, Eisner et al. (2005) modeled the spectral energy distribution (SED) of L1489 IRS and demonstrated that this required a significantly different systemic inclination of only 36°.

In this chapter, we try to address these issues through arc second scale interferometric observations of the dense gas tracer HCO^+ $J = 3 - 2$ from the SMA. These observations provide information on the gas dynamics on scales ~100 AU and reveal an embedded protoplanetary disk. We show how careful modeling of the full SED from near-infrared through millimeter wavelengths can place strong constraints on the geometry of such a disk.

4.2 Observations and data reduction

Observations were carried out at the SMA[1] located on Mauna Kea, Hawaii. Our data set consists of two separate tracks of measurements in different array configurations. The first track was obtained on December 11, 2005. This track was done in the compact configuration resulting in a spatial resolution of $\sim 2.5''$ with projected baselines ranging between 10 and 62 kλ. A second track was obtained on November 28, 2006, in the extended configuration with the resolution of about $1''$ and baselines between 18 and 200 kλ. The resolution of the two configurations corresponds to linear sizes of 350 AU and 140 AU respectively. The synthesized beam size of the combined track using uniform visibility weighting is $0.9'' \times 0.7''$ with a position angle of $78°$.

In both tracks the receiver was tuned to HCO^+ $J = 3$–2 at 267.56 GHz. We used a correlator configuration with high spectral resolution across the line, providing a channel width of 0.2 km s^{-1} over 0.104 GHz. The remainder of the 2 GHz bandwidth of the SMA correlator was used to measure the continuum. No other lines in this band are expected to contaminate the continuum. We did not encounter any technical problems during observations and the weather conditions were excellent during both tracks. For the compact configuration track, τ_{225} was 0.06 and for the extended track τ_{225} was at 0.08.

Mars was used as flux calibrator in the first track, and Uranus for the second track. The quasars 3c454.3, 3c273, and 3c279 were used for passband calibration for both tracks, while the complex gains were calibrated using the two quasars 3c111 and 3c84, located within 18 degrees from L1489 IRS. The calibrators were measured every 20 minutes throughout both tracks. Their fluxes were determined to be 3.1 and 2.6 Jy for 3c111 and 3c84 in the compact track, and 2.3 and 2.2 Jy for 3c111 and 3c84 in the extended track, respectively. For the gain calibration, a time smoothing scale of 0.7 hours was used, which ensures that the large scale variations in the phase during the track are corrected for. The data do not show any significant small scale variations (i.e., rapid fluctuations in the phases or amplitudes). The quasars appear as point sources even at the longest baselines, which means that phase decorrelation due to atmospheric turbulence is negligible. The signal-to-noise of the calibrators is >50 per integration.

The data were reduced using the MIR software package (Qi 2006)[2]. Due to the excellent weather conditions, the data quality is very high and the data

---

[1]The Submillimeter Array is a joint project between the Smithsonian Astrophysical Observatory and the Academia Sinica Institute of Astronomy and Astrophysics and is funded by the Smithsonian Institution and the Academia Sinica

[2]Available at http://cfa-www.harvard.edu/~cqi/mircook.html.

Table 4.1: Summary of the SMA observations.

Source	L1489 IRS
$\alpha, \delta(2000)^a$	04:04:42.85, +26:18:56.3
Frequency	267.55762 GHz (1.12 mm)
Integrated line intensity	41.85 Jy beam^{-1} km s^{-1}
Peak line intensity	2.04 K
Noise level (rms)	0.35 Jy beam^{-1}
Continuum flux	36.0±2.3 mJy
Noise level (rms)	3.7 mJy beam^{-1}
Synthesized beam size	$0.9'' \times 0.7''$
(Uniform weighting)	

^{a} Coordinates are given at the position where the continuum emission peaks.

reduction procedure was smooth and unproblematic. All post-processing of the data, including combining the two visibility sets, was done using the MIRIAD package (Sault et al. 1995)[3]. Relevant numbers are presented in Table 4.1.

In this chapter we also make use of continuum measurements of L1489 IRS found in the literature, ranging from the near-infrared (Kenyon et al. 1993; Eisner et al. 2005; Padgett et al. 1999; Park & Kenyon 2002; Whitney et al. 1997; Myers et al. 1987; Kessler-Silacci et al. 2005) to (sub)millimeter wavelengths (Hogerheijde & Sandell 2000; Moriarty-Schieven et al. 1994; Motte & André 2001; Hogerheijde et al. 1997; Ohashi et al. 1996; Saito et al. 2001; Lucas et al. 2000).

4.3 Results

The two tracks of observations provide us with two sets of (u, v)–points, which, when combined and Fourier transformed, samples the image (x, y) plane well from scales of 1 to 30$''$ (140 to 4200 AU). Emission on spatial scales greater than this is filtered out by the interferometer due to its finite shortest spacing. This filtering is accounted for when comparing models to the observations.

The measured continuum emission is shown as an image in Fig. 4.1. Previous attempts to measure the continuum at 1.1 mm with the BIMA interferometer were not successful (Hogerheijde 2001). The SMA however, reveals a complex and detailed, slightly elongated structure.

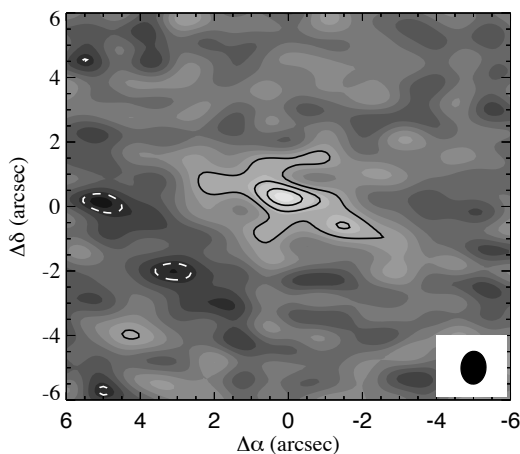[3]Available at http://bima.astro.umd.edu/miriad/miriad.html

Figure 4.1: Reconstructed image of the continuum emission at the highest resolution ($0.9'' \times 0.7''$). The contours are linearly spaced with 1σ starting at 2σ and dashed lines are negative contour levels.

Two reconstructed images of the HCO$^+$ emission are shown in Fig. 4.2 using the *natural* and *uniform* weighting schemes, optimizing the signal-to-noise and angular resolution, respectively. In the upper two panels of this figure, the zero moment map is plotted as solid contour lines and the first moment is shown as shaded contours. It is clear that both images reveal an elongated, flat structure. In the uniformly weighted image there is a large amount of asymmetry in the structure, which is less prominent in the naturally weighted image.

The velocity contours in the lower panel of Fig. 4.2 are seen to be closed around a point, which is offset by some $3''$ from the peak of the emission. There is also clearly a gradient in the velocity field along the major axis of the object. This feature was previously reported by Hogerheijde (2001) using interferometric observations of HCO$^+$ $J = 1–0$, and low signal-to noise HCO$^+$ $J = 3–2$ observations, from the BIMA and OVRO arrays. The gradient in the velocity field coincides almost perfectly with the long axis of the structure. When compared to the BIMA HCO$^+$ $J = 3–2$ observations, the SMA data give 5–10 times better resolution. Furthermore, the BIMA data had to be self-calibrated using the HCO$^+$ $J = 1–0$ image as a model and thus the resulting image was somewhat dependent on the structure of the lower excitation emission. The image we obtain from the
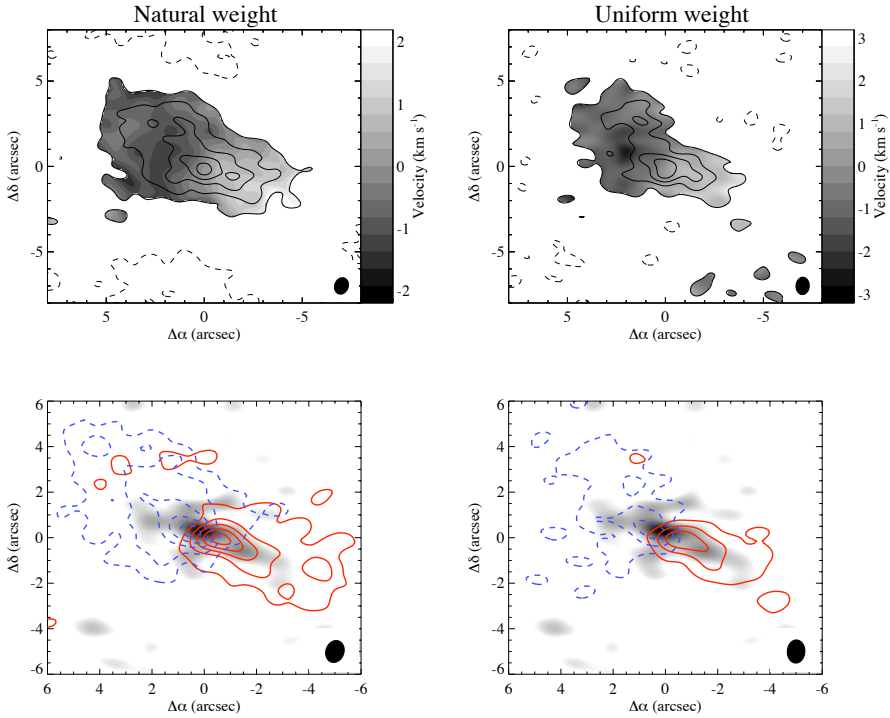
Figure 4.2: The top row shows zero and first moment plots of the HCO$^+$ J = 3–2 emission toward L1489 IRS. Contours are linearly spaced by 2σ with a clip level of 2σ. σ equals 1.1 and 2.0 Jy beam^{-1} km s^{-1} for the natural and uniform weighting schemes, respectively. Negative contours appear as dashed lines. The bottom row shows the corresponding channel maps with dashed contours marking negative velocities and full contours marking possitive velocities.

SMA data is of considerably better quality.

In Fig. 4.3, the zero moment emission contours have been superposed on the near-infrared scattered light image taken by the Hubble Space Telescope (Padgett et al. 1999). The figure shows that many of the details in the SMA image coincide with features seen in the scattered light image. The spectral map in Fig. 4.4 shows single spectra at positions offset by 2″ from each other. Each position shown here is the spectrum contained within one synthesized beam. The center most spectrum coincides with the peak of the emission in Fig. 4.2. Here we see a very broad, double peaked line. Moving outward from the center, the lines become
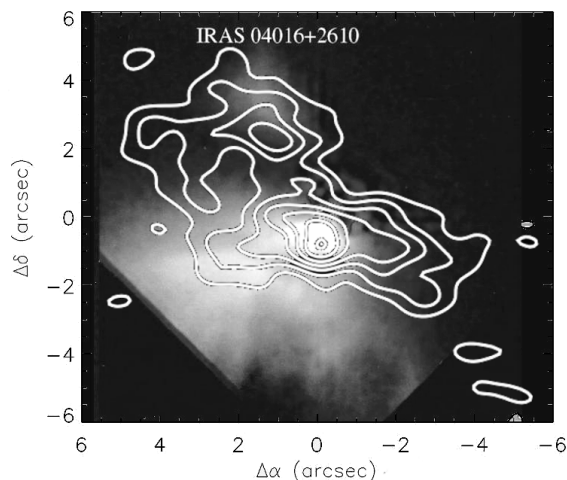
Figure 4.3: HCO$^+$ emission (1σ) contours superposed on the near-infrared scattered light image (Padgett et al. 1999).

single peaked and offset in velocity space with respect to the systemic velocity. Perpendicular to the long axis of the structure, the line intensity falls off quickly. The lines shown in Fig. 4.4 are reconstructed using the natural weighting scheme. For the remainder of this chapter we will use the uniformly weighted maps where the resolution is optimal.

Figure 4.5 shows the emission in a position-velocity (PV) diagram, where the image cube has been sliced along the major axis to produce the intensity distribution along the velocity axis. The PV–diagram shows almost no emission in the second and fourth quadrant, which is a strong indicator of rotation. The small amount of low velocity emission seen close to the center in the fourth quadrant may be accounted for by infalling gas.

4.4   Analysis

With the resolution provided by the SMA it is possible to probe the central parts of L1489 IRS on scales of ~100 AU, where the protoplanetary disk is expected to be present. Furthermore, the HCO$^+$ $J = 3$–2 transition traces H$_2$ densities of
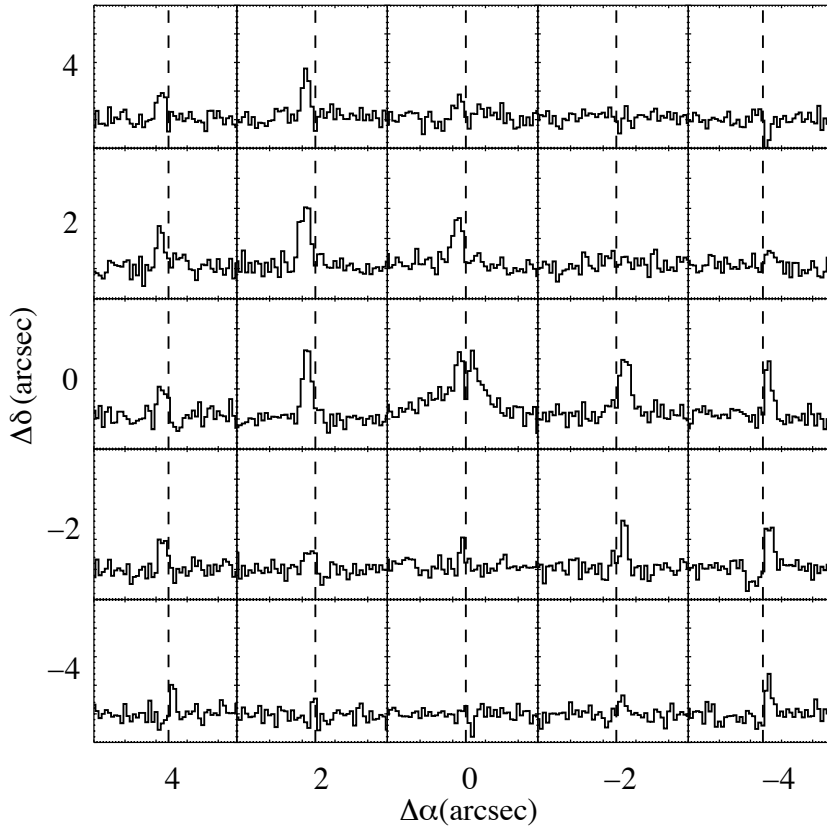
Figure 4.4: Spectral map of L1489 IRS. The spectra are evenly spaced with 2″. The bandwidth in each panel is 20 km s^{-1}. The scale on the *y*-axis goes from 0 to 2 Jy beam^{-1}.
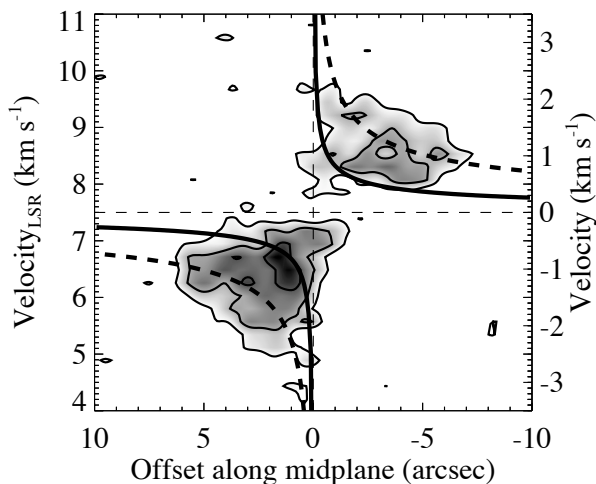
Figure 4.5: PV-diagram. This plot shows that the emission on the scales measured by the SMA is entirely dominated by rotation. The black curves show the Keplerian velocity, calculated from the dynamic mass (1.35 $M_\odot$) obtained in chapter 2. The curves have been inclination corrected with 74° for the full lines and 40° for the dashed lines. Contours start at 2σ and increase with $1\sigma = 0.12$ Jy beam^{-1}.

10^6 cm^{-3} or more (Schöier et al. 2005), which are expected in the inner envelope and disk. The model presented in Chapter 2 was not explicitly made to mimic a disk, but rather to describe the morphology of the images on large scales. Using this model, which works well on a global scale, we can explore how well it fits the SMA spectra when extrapolated to scales unconstrained by the single-dish observations.

Figure 4.6 compares the SMA observations to the predictions of this model (dashed line). For doing this comparison, the model is imaged using the (u, v)-spacings from the observations, so that directly comparable spectra are obtained. While the spectra away from the center are fairly well reproduced in terms of line width, the center position is too wide, i.e., the model produces velocities that are too extreme compared to the measured velocities.

To check that this emission does in fact originate from scales less than 200 AU, a model where HCO$^+$ is completely absent within a radius of 200 AU is also shown in Fig. 4.6 with the dotted line. In this model the wide wings disappear
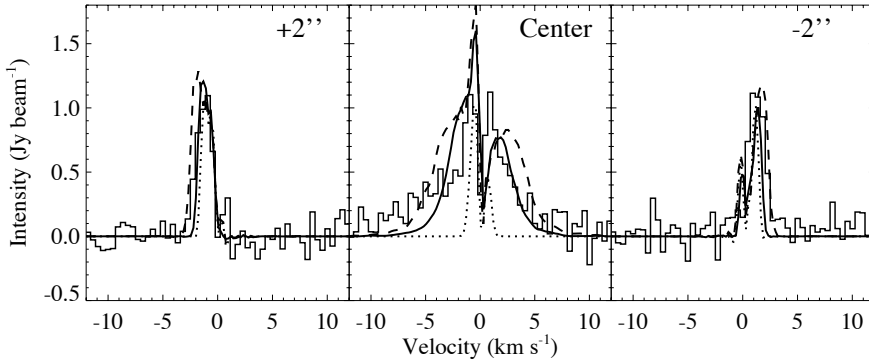
Figure 4.6: Three spectra from the SMA observations with model spectra super-posed. The two off-positions are chosen in the direction along the long axis of the object. The offsets are chosen to be a resolution element. Three models are also shown: the dashed line shows the unmodified model from Chapter 2, the full line is the model from Chapter 2, but inclined at 40°, and the dotted line shows a model where HCO^+ is absent on scales smaller than 200 AU.

and only a very narrow line is left. The two off-positions, which lie outside of the radius of 200 AU, are not affected by introducing this cavity.

Figure 4.6 also shows a spectrum that is made from the model of Chapter 2, but inclined at 40° (full line). This is a considerably better fit than the other two models (again the two off-positions are little affected). While the observations of the larger scale structure (Chapter 2, Hogerheijde 2001) demonstrate that the inclination of the flattened, collapsing envelope is ~74°, the SMA observations suggest that a change in the inclination occurs on scales of 100–200 AU, reflecting the presence of a dynamically different component. On the other hand, since the model of chapter 2 was tuned to match the single-dish observation on scales of ~1000 AU or more, and did not explicitly take the disk into account, it is not unexpected that it does not fully reproduce the SMA observations.

4.4.1   Introducing a disk model

To reproduce also the interferometric observations, we have modified the model from Chapter 2 on scales corresponding to the innermost envelope and disk. The improvements consist largely of two things: a different parameterization of the

density distribution and the explicit inclusion of a disk.

The description used in Chapter 2 has a discontinuity for small values of r and θ. Again, this is not a problem when working with the large scale emission, but becomes a problem when interfaced with a disk where a continuous transition from envelope to disk is preferred. The new parameterization we use for the envelope is adopted from Ulrich (1976). In this representation the envelope density is given by,

$$
\begin{aligned}
\rho_{env}(r,\theta) \;=\; & \rho_0 \left(\frac{r}{R_{rot}}\right)^{-1.5} \left(1 + \frac{\cos\theta}{\cos\theta_0}\right)^{-1/2} \\
& \times \left(\frac{\cos\theta}{2\cos\theta_0} + \frac{R_{rot}}{r}\cos 2\theta_0\right)^{-1},
\end{aligned}
\tag{4.1}
$$

where θ_0 is the solution of the parabolic motion of an infalling particle given by $r/R_{rot}(\cos\theta_0 - \cos\theta)/(\cos\theta_0 \sin 2\theta_0) = 1$, $R_{rot} = 150$ AU is the centrifugal radius of the envelope, and ρ_0 is the density on the equatorial plane and at the centrifugal radius. Since the outer radius, total mass, aspect ratio, and peak density are held fixed, the new parameterization is qualitatively similar to the Plummer-like profile used in Chapter 2. The numerical value of R_{rot} is chosen so that the maximum deviation in density in the (r,θ)-plane only reaches 20% in the most dense parts (outside of the disk cavity) and has an average deviation of less than 5%.

In addition to this envelope, a generic disk is also introduced in the model. The density of the disk is given by,

$$
\rho_{disk}(r,\theta) = \frac{\Sigma_0\,(r/R_0)^{-1}}{\sqrt{2\pi}\,H_0}\,\exp\left\{-\frac{1}{2}\left[\frac{r\cos\theta}{H_0}\right]^2\right\},
\tag{4.2}
$$

where θ is the angle from the axis of symmetry, R_0 is the disk outer radius, and H_0 is the scale height of the disk. The model thus has four free parameters: disk radius, pressure scale height, mass (taken as a fraction of the total mass of the circumstellar material), and inclination. In order to maximize the mid-infrared flux, we use a flat disk, i.e., with no increase in scale height with radius and fix the scale height to 0.25. The outer radius is fixed to 200 AU, the distance from the center of the emission in Fig. 4.2 to the position of the closed velocity contour, thereby effectively reducing the number of free parameters to two. This outer disk radius is not a strongly constrained parameter since neither the SED nor the model spectra are strongly influenced by changes in this value. It is only possible to rule out the extreme cases, where the disk either gets so small that it is no longer influencing the SED or where it gets so big that it holds a significant
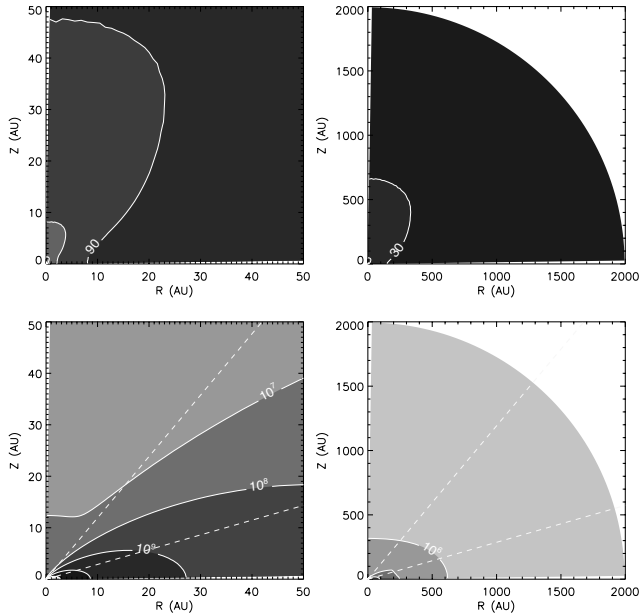
Figure 4.7: A slice through the model of L1489 IRS: the top panels show the temperature (K) on different scales and the bottom panels show the corresponding density (cm^{-2}) profiles. The dashed lines marks the 40° and 74° line-of-sight.

fraction of the total mass. We find that the best fit is provided by a disk mass of $M_{disk} = 4 \times 10^{-3}$ M$_\odot$. A cross section of the model is shown in Fig. 4.7.

The velocity field in the envelope is similar to the one used in Chapter 2 and 3, where the velocity field was parameterized in terms of a central mass and an angle between the velocity vector and the azimuthal direction, so that the ratio of infall to rotation could be controlled by adjusting this angle. The best fit parameter values obtained in Chapter 2 of 1.35M$_\odot$ for the central mass and flow lines inclined with 15° with respect to the azimuthal direction, are used. No radial motions are allowed in the disk: only full Keplerian motion is present in the region of the model occupied by the disk.

In order to produce synthetic observations that can be directly compared to the data, we use numerical radiative transfer tools. The three-dimensional continuum radiative transfer code RADMC (Dullemond & Dominik 2004) is used to calculate the scattering function and the temperature structure in the analytical

axisymmetric density distribution. In these calculations, the luminosity measurement by Kenyon et al. (1993) of 3.7 $L_\odot$ is used for the central source. The solution is then ray–traced using RADICAL (Dullemond & Turolla 2000) to produce the spectral energy distribution and the continuum maps at the observed frequencies. In both RADMC and RADICAL we assume certain properties of the dust. We use the dust opacities that give the best fit to extinction measurements in dense cores (Pontoppidan et al. in prep).

The same density and temperature structure are afterward given as input to the excitation and line radiative transfer code RATRAN (Hogerheijde & van der Tak 2000), which is used to calculate the spatial and frequency dependent HCO^+ $J = 3$–2 emission. The HCO^+ models are post-processed with the MIRIAD tasks *uvmodel, invert, clean,* and *restore* to simulate the actual SMA observations.

4.4.2 Modeling the continuum emission

In Fig. 4.8, we compare our model to the continuum observations. We calculate (u, v)–amplitudes at 1.1 mm, which we plot on top of the observed amplitudes. The result is in good agreement with the data, suggesting that the dust emission is well-described by our parameterization down to scales of ~ 100 AU. This comparison is not very dependent on the inclination, since the continuum emission is quite compact. For this particular figure, an inclination of 40° is assumed.

Recently, Eisner et al. (2005) modeled the SEDs of a number of Class I objects in Taurus, including L1489 IRS. The model used in their work is parameterized differently from ours, but it essentially describes a similar structure. As pointed out above, Eisner et al. find a best fit inclination of 36° in contrast to the inclination of 74° found in Chapter 2.

To test the result of Eisner et al. (2005) we calculated the SED using the described model with only the system inclination as a free parameter (Fig. 4.9). The best fit is found for an inclination of about 40°, in good agreement with the result of Eisner et al. (2005). The models with inclinations of 50° and 74° are also plotted in Fig. 4.9 in order to show how the SED depends on inclination.

Note that the quality of our best fit to the SED is comparable to the fit presented by Eisner et al. (2005), whereas the fit becomes rapidly worse with increasing inclinations larger than 40°, thus resulting in disagreements with the results from Hogerheijde (2001) and Chapter 2. The three different models plotted in Fig. 4.9 cannot be distinguished for wavelengths above $\sim$60 μm, which corresponds to a temperature of about 40 K using Wiens displacement law. This temperature occurs on radial distances of approximately 100 AU from the central object, which means that outside of this radius, the SED is no longer sensitive to
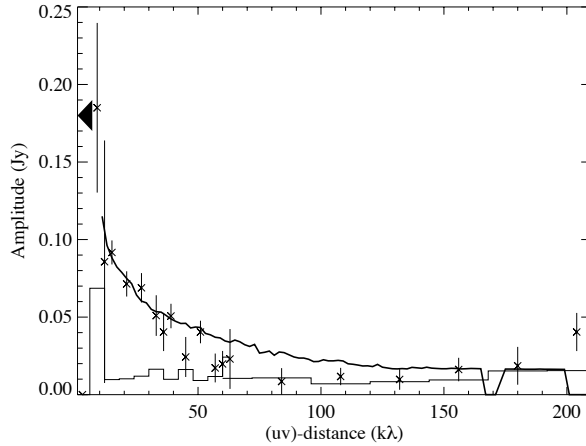
Figure 4.8: The averaged (u, v)–amplitudes of the continuum at 1 mm in both compact and extended configurations. The full line show our model. The compact configuration visibilities cover the (u, v)–distance up to 60 kλ. The black triangle marks the total flux at 1 mm (Moriarty-Schieven et al. 1994). The histogram indicates the zero-signal expectation values.

the inclination. We interpret this behavior as a change in the angular momentum axis on disk scales, causing the disk to be inclined with respect to the envelope.

4.4.3 Modeling the HCO$^+$ emission

In Chapter 2 we found that the characteristic double peak feature of the HCO$^+$ $J = 4$–3 line could not be reproduced with an inclination below 70°. On the other hand, including a disk inclined by 40° into the model of Chapter 2 does not alter the fit to the single-dish lines (Fig. 4.10): the geometry and the velocity field of the material at scales smaller than ~300 AU does not influence the shape of these lines. This fit is not perfect though, as it still overestimates the red-shifted wing in the $J = 3$–2 line and the width of the $J = 1$–0 line slightly, but the quality of the fit is similar to that shown in Chapter 2.

We need to test how well this tilted disk model works with the line observations from the SMA. It was shown in Sect. 4.4 that the off-position spectra are weakly dependent on changes in the inclination and that the same is true when using the model where the disk is tilted with respect to the envelope. The cen-
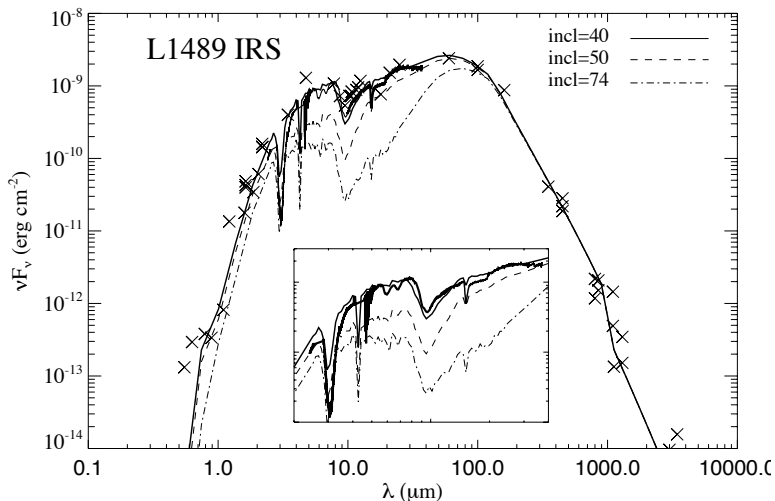
Figure 4.9: The model spectral energy distribution assuming inclinations of 40°
(full line) and 50° and 74° (broken lines) plotted on top of flux measurements
from the literature (marked by crosses) and the Spitzer/IRS spectrum from 2 – 40
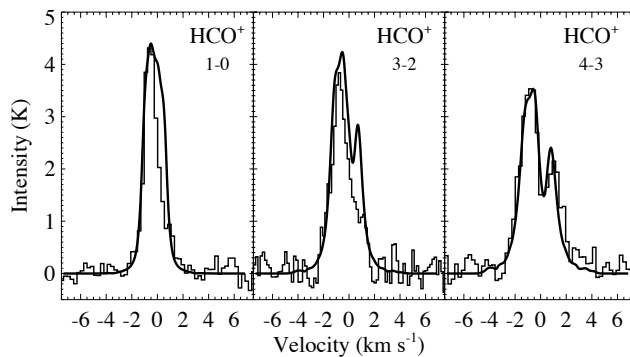microns (heavy black line).

Figure 4.10: Three transitions of HCO$^+$ observed by single-dish telescope (see
Chapter 2 for details) with our model superposed. The quality of the fit is compa-
rable to the fit in Chapter 2 although a disk model has now been included.
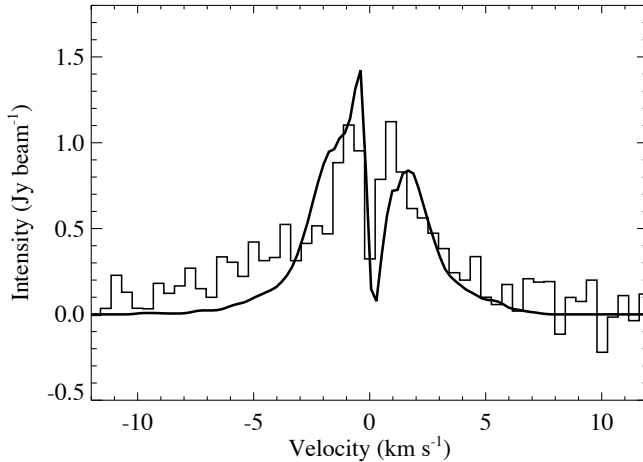
Figure 4.11: The SMA spectrum towards the center of L1489 IRS with our model, consisting of a disk which is inclined with respect to the envelope, superposed. As in Fig. 4.6, the model has been imaged with the (u, v)-spacings from the observations.

tral position, however, is seen in Fig. 4.11 to be very well reproduced in terms of line width and wing shape by this model. The model spectrum is slightly more asymmetric than the data, which means that the infall to rotation ratio is not quite correct on disk scales. The magnitude of the velocity field projected onto our line of sight is correct though, since the width of the line is well fit.

We also compared the averaged (u, v)–amplitudes to evaluate the quality of our model, similar to the procedure for the continuum. Fitting the (u, v)–amplitudes in this way tests whether the model produces the right amount of emission at every scale. The best fit is shown in Fig. 4.12. The zero-spacing flux is also shown in this plot, marked by the black triangle. This method has previously been used to study the abundance variations of given molecules in protostellar envelopes, in particular imaging directly where significant freeze-out occurs in protostellar envelopes (Jørgensen 2004; Jørgensen et al. 2005a). The model does a good job reproducing the observed HCO$^+$ brightness distribution on almost all scales with a constant abundance, except around 20–40 kλ where it overestimates the amount of observed flux. This correspond to a radius of about 1000 AU, which is well outside of the disk. On the other hand, single-dish observations of low-mass protostellar
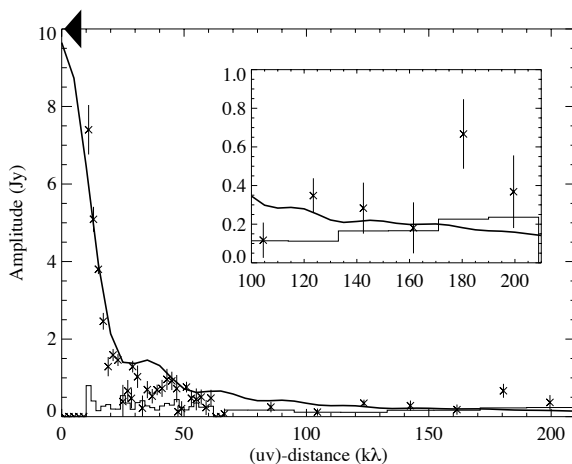
Figure 4.12: Similar to Fig. 4.8 but for the HCO$^+$ J = 3–2 measurements. The triangle marks the total flux obtained from the single-dish observations. The amplitudes have been averaged over ± 5 km s^{-1} relative to the systemic velocity. The histogram indicates the zero-signal expectation values. The insert is an enlargement of the longest baselines.

envelopes suggest that these are scales where significant freeze-out, in particular of CO, may occur at temperatures $\lesssim 20 - 30$ K, which, because of the gas-phase chemical relation between CO and HCO$^+$, also reflects directly in the observed distribution of HCO$^+$ (e.g., Jørgensen et al. 2004, 2005b). Despite this, the difference between the model prediction and observations is small with this constant abundance, suggesting that the amount of freeze-out is small in L1489 IRS. This is in agreement with the single-dish studies of Jørgensen et al. (2002, 2004, 2005b), who generally found little depletion in the envelopes of L1489 IRS and other Class I sources, in contrast to the more deeply embedded, Class 0, protostars.

The model parameter values obtained in this section, including values from Table 2.2, are summarized in Table 4.2. The best fit values that are derived in this chapter are tuned by hand rather than systematically optimized by a χ^2 minimization method. Therefore, we can only give an estimate on the uncertainties. However, Fig. 4.9 shows that the SED fit gets rapidly worse when changing the inclination, and given the strong dependence of the envelope inclination on the single-dish lines, we estimate that both angles are accurate to within 10°. For the disk mass and radius, the uncertainties on the parameter values are less well de-

Table 4.2: Model parameter values.

Envelope	Value
Outer radius[a]	2000 AU
Envelope mass[a]	0.093 $M_\odot$
Inclination[a,b]	74°
HCO^+ abundance[a]	3.0×10^{-9}

Disk	Value
Radius[b]	200 AU
Disk mass[b]	4×10^{-3} $M_\odot$
Inclination[b]	40°
Scale height[c]	z=0.25R
Central mass[a]	1.35 $M_\odot$
Central luminosity[c]	3.7 $L_\odot$
Distance[c]	140 pc

[a] Values from Chapter 2
[b] Fitted values
[c] Values adopted from the literature

fined, for reasons given in Sect. 4.4.1, but we estimate the accuracy to be within a factor of 2 for each of these parameters.

4.5 Discussion

It seems that depending on the physical scales that we probe, the solution favors a different inclination. When taking *all available* observations into account we need to introduce a model where the angular momentum vector of the disk is misaligned with the angular momentum vector of the (rotationally flattened) envelope. We adopt a two component model (illustrated in Fig. 4.13), disk and envelope, but in reality, the angular momentum axis may indeed be a continuous function of radius on the scales of the disk ($\lesssim$ a few hundred AU). The origin of such a misalignment can actually be explained in a simple way by considering the initial conditions of the collapse.

The state of a pre-stellar core before the gravitational collapse begins is typically described by a static sphere with a solid body rotation perturbation (Terebey
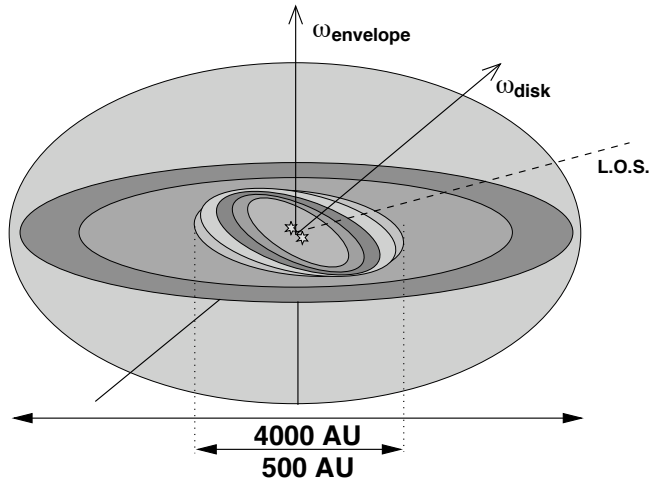
Figure 4.13: An (exaggerated) illustration of the proposed model where the angular momentum axis is changing with radius. The line of sight is illustrated by the dashed line.

et al. 1984). Due to strict angular momentum conservation, such a model would be perfectly aligned throughout the collapse and consequently disk formation models are often described numerically by axisymmetric representations (e.g., Yorke & Bodenheimer 1999).

However, there is no *a priori* reason why a pre-stellar core should rotate as a solid body. Of course, the cloud has an average angular momentum, which on a global scale determines the axis of rotation. The cloud does not collapse instantly to form a disk though, but rather from the inside and out, as described by Shu (1977), and therefore a shell of material from deep within the cloud, which may very well have an average angular momentum that is different from the global average, will collapse and form a disk before material from further out has had a chance to accrete. Actually, if the parental cloud is turbulent, it is to be expected that the accreting material has randomly oriented angular momentum and a misalignment of the angular momentum on different scales is more likely than a perfect alignment. In this way a system, similar to the model proposed to describe L1489 IRS in this chapter, can be formed.

To obtain a gradient in the angular momentum as initial condition for the collapse, one may consider a cloud that is not spherically symmetric or one that does not collapse around its geometrical center, but rather around an over dense

clump offset from the center. The former scenario may indeed be true for the case of L1489 IRS, which is seen to be dynamically connected to a neighboring cloud (which was also modeled in Chapter 2 to explain the excess of cold emission seen in some of the low-J lines). Actually, the uniformly weighted moment map (Fig. 4.2) shows significant asymmetry with a secondary emission peak to the north-west.

It is interesting to note that the HCO^+ emission from the SMA observations agrees very well with the near-infrared image (Fig. 4.3): the secondary peak, a few arc seconds northeast of the main continuum and HCO^+ peaks, nicely coincides with a bright spot in the scattered light image, and also the shape of the cavity towards the south follows the contours of the HCO^+ emission. The same details are not revealed in the naturally weighted SMA image, in which shorter baselines are given more weight. We thus conclude that by going to the extended SMA configuration, it is possible to probe structure in YSOs on the same scales as can be resolved by large near-infrared telescopes, such as the Hubble Space Telescope. The structure seen in both images, however, also emphasizes that for a fully self-consistent description of L1489 IRS, a global non-axisymmetric model has to be considered.

Another possible (non-exclusive) explanation of a misaligned disk would be that L1489 IRS formed as a triple stellar system and, due to gravitational inter-action, one of the stars was ejected. L1489 IRS would thus be a binary system, as suggested by Hogerheijde & Sandell (2000). The loss of angular momentum due to the ejection would result in a rearrangement of the remaining binary, which could "drag" the inner viscous disk along. Such a scenario has been investigated numerically by Larwood et al. (1996). In the case of L1489 IRS, it would have to be a very close binary with a separation of no more than a few AUs since the near-infrared scattered light image (Padgett et al. 1999) with a resolution of ~0.2″ (30 AU), does not reveal multiple sources. The ratio of binary separation to disk radius is therefore significantly lower than the cases investigated by Larwood et al. (1996) and it is therefore not clear whether similar effects could be present in L1489 IRS.

If indeed the system is binary, it would resolve the issue that we find a central mass of 1.35 $M_\odot$ while the luminosity is estimated to be 3.7 $L_\odot$ (Kenyon et al. 1993). A single young star that massive would require a much higher luminosity, but two stars of 0.6–0.7 $M_\odot$ would fit nicely with the estimated luminosity, since luminosity is not a linear function of mass for YSOs.

To test whether L1489 IRS is indeed a binary and to constrain the innermost disk geometry on AU scales, measurements of temporal variability in super high

resolution are needed. The timescale for variations of a possible binary is of the order of years, depending on the exact separation of the stars (assuming scales of 1 AU). Such observations would, for example, be feasible with ALMA.

4.6 Conclusion

In this chapter, we have presented high angular resolution interferometric observations of the low-mass Class I YSO L1489 IRS. The observations reveal a rotationally dominated, very structured central region with a radius of about 200–300 AU. We interpret this as a young Keplerian disk that is still deeply embedded in envelope material. This conclusion is supported by a convincing fit with a disk model to the SED.

We conclude further that the inclination of the disk is not aligned with the inclination of the flattened envelope structure, due to the possibility that L1489 IRS is a binary system and/or that the average angular momentum axis of the cloud is not aligned with the angular momentum axis of the dense core that originally collapsed to form the star(s) plus the disk.

We find that a disk with a mass of 4×10^{-3} M$_\odot$, a radius of 200 AU, and a pressure scale height of z=0.25R is consistent with both the SED and the HCO$^+$ observations. Only a small amount of chemical depletion of HCO$^+$ is allowed for, due to a slight over-estimate of the (u, v)–amplitudes at 20–40 kλ by our model, in agreement with the results from previous single-dish studies and the nature of L1489 IRS as a Class I YSO.

The combination of a detailed modeling of the SED with spatially resolved line observations, which contains information on the gas kinematics, appears to be a very efficient way of determining the properties of disks, especially embedded disks that are not directly observable.

References

Adams, F. C., Lada, C. J., & Shu, F. H. 1987, ApJ, 312, 788

Adams, F. C., Shu, F. H., & Lada, C. J. 1988, ApJ, 326, 865

Basu, S. 1998, ApJ, 509, 229

Boogert, A. C. A., Hogerheijde, M. R., & Blake, G. A. 2002, ApJ, 568, 761

Burrows, C. J., Stapelfeldt, K. R., Watson, A. M., et al. 1996, ApJ, 473, 437

Cassen, P. & Moosman, A. 1981, Icarus, 48, 353

Dullemond, C. P. & Dominik, C. 2004, A&A, 417, 159

Dullemond, C. P. & Turolla, R. 2000, A&A, 360, 1187

Eisner, J. A., Hillenbrand, L. A., Carpenter, J. M., & Wolf, S. 2005, ApJ, 635, 396

Hogerheijde, M. R. 2001, ApJ, 553, 618

Hogerheijde, M. R. & Sandell, G. 2000, ApJ, 534, 880

Hogerheijde, M. R. & van der Tak, F. F. S. 2000, A&A, 362, 697

Hogerheijde, M. R., van Dishoeck, E. F., Blake, G. A., & van Langevelde, H. J. 1997, ApJ, 489, 293

Jørgensen, J. K. 2004, A&A, 424, 589

Jørgensen, J. K., Bourke, T. L., Myers, P. C., et al. 2005a, ApJ, 632, 973

Jørgensen, J. K., Schöier, F. L., & van Dishoeck, E. F. 2002, A&A, 389, 908

Jørgensen, J. K., Schöier, F. L., & van Dishoeck, E. F. 2004, A&A, 416, 603

Jørgensen, J. K., Schöier, F. L., & van Dishoeck, E. F. 2005b, A&A, 435, 177

Kenyon, S. J., Calvet, N., & Hartmann, L. 1993, ApJ, 414, 676

Kessler-Silacci, J. E., Hillenbrand, L. A., Blake, G. A., & Meyer, M. R. 2005, ApJ, 622, 404

Lada, C. J. & Wilking, B. A. 1984, ApJ, 287, 610

Larwood, J. D., Nelson, R. P., Papaloizou, J. C. B., & Terquem, C. 1996, MNRAS, 282, 597

Lucas, P. W., Blundell, K. M., & Roche, P. F. 2000, MNRAS, 318, 526

Moriarty-Schieven, G. H., Wannier, P. G., Keene, J., & Tamura, M. 1994, ApJ, 436, 800

Motte, F. & André, P. 2001, A&A, 365, 440

Myers, P. C., Fuller, G. A., Mathieu, R. D., et al. 1987, ApJ, 319, 340

Ohashi, N., Hayashi, M., Kawabe, R., & Ishiguro, M. 1996, ApJ, 466, 317

Padgett, D. L., Brandner, W., Stapelfeldt, K. R., et al. 1999, AJ, 117, 1490

Park, S. & Kenyon, S. J. 2002, AJ, 123, 3370

Qi, C. 2006, The MIR Cookbook, The Submillimeter Array/Harvard-Smithsonian

Center for Astrophysics

Qi, C., Ho, P. T. P., Wilner, D. J., et al. 2004, ApJ, 616, L11

Reipurth, B., Jewitt, D., & Keil, K., eds. 2007, Protostars and Planets V (University of Arizona Press)

Rodríguez, L. F., D'Alessio, P., Wilner, D. J., et al. 1998, Nature, 395, 355

Saito, M., Kawabe, R., Kitamura, Y., & Sunada, K. 2001, ApJ, 547, 840

Sault, R. J., Teuben, P. J., & Wright, M. C. H. 1995, Astronomical Data Analysis Software and Systems IV, 77, 433

Schöier, F. L., van der Tak, F. F. S., van Dishoeck, E. F., & Black, J. H. 2005, A&A, 432, 369

Shu, F. H. 1977, ApJ, 214, 488

Terebey, S., Shu, F. H., & Cassen, P. 1984, ApJ, 286, 529

Thi, W. F., van Dishoeck, E. F., Blake, G. A., et al. 2001, ApJ, 561, 1074

Ulrich, R. K. 1976, ApJ, 210, 377

Whitney, B. A., Kenyon, S. J., & Gomez, M. 1997, ApJ, 485, 703

Yorke, H. W. & Bodenheimer, P. 1999, ApJ, 525, 330

Chapter 5

Time-dependent CO chemistry during the formation of protoplanetary disks

Abstract

Understanding the gas abundance distribution is essential when tracing star formation using molecular line observations. Variations in density and temperature conditions can cause gas to freeze-out onto dust grains, and this needs to be taken into account when modeling a collapsing molecular cloud. This study aims to provide a realistic estimate of the CO abundance distribution throughout the collapse of a molecular cloud. We derive abundance profiles and synthetic spectral lines that can be compared with observations.We use a two-dimensional hydrodynamical simulation of a collapsing cloud and subsequent formation of a protoplanetary disk as input to the chemical calculations. From the resulting abundances, synthetic spectra are calculated using a molecular excitation and radiation transfer code. We compare three different methods to calculate the abundance of CO. Our models also consider cosmic ray desorption and the effects of an increased CO binding energy. The resulting abundance profiles agree well with analytic approximations, and the corresponding line fluxes match the observational data. Our method to calculate abundances in hydrodynamical simulations should help comparisons with observations, and can easily be generalized to include gas-phase reaction networks.

Christian Brinch, Reinout J. van Weeren, and Michiel R. Hogerheijde

5.1 Introduction

The study of low-mass young stellar objects (YSOs), from early protostellar cores to T Tauri stars surrounded by disks, involves observations of either the thermal emission from dust grains or molecular line emission. While dust emission yields information about the temperature profile (e.g. Draine & Lee 1984), and, through measurements of the shape of the spectral energy distribution, the evolutionary stage (Lada & Wilking 1984; Adams et al. 1987), spectral lines are the only way to constrain the kinematical properties of YSOs. The interpretation of molecular lines is crucial to the understanding of protoplanetary disk formation and the distribution of angular momentum during these stages of star formation (Evans 1999). However, deriving the gas motion from spectral line profiles is complicated by degeneracies between the velocity field topology, inclination of the angular momentum axis, optical depth, and geometrical effects, as we saw already in Chapter 2.

In addition to these effects, molecular abundances can vary significant. The gas abundance is determined by the ongoing chemistry driven by the co-evolving density and temperature distributions, and to some extent also by the velocity field. The variation in molecular abundances throughout a YSO may have a huge impact on line profiles and therefore it is important to understand the chemistry in interpreting these line profiles. The effect of the chemistry is enhanced for observations of higher resolution. If observations are completed, however, at relatively low resolution ($\gtrsim 10''$), the emission is broadened over a significant area of the object and a single average value of abundance is adequate. However, at higher resolution, using submillimeter interferometry ($\sim 1''$), the emission is averaged over a smaller part of the object and variations in the abundance must be taken into account.

The problem in determining the abundance distribution was addressed before in the literature in the context of low-mass star formation. Lee et al. (2004) adopted a semi-analytical approach using a self-similar collapse of an isothermal sphere in which they followed "fluid-elements". The chemistry was followed in a series of Bonnor-Ebert spheres during the pre-stellar phase and in a self-similar inside-out collapse during the protostellar phase. This model provided a good analytical description of the early stages of star formation, but, lacking any rotational velocity, no disk was formed in this scenario. Aikawa et al. (2001, 2003, 2005) followed the chemical evolution of contracting pre-stellar clouds using an approach similar to Lee et al. (2004) but using an isothermal cloud collapse only. Their calculations considered only the early stages of the star formation process. Jørgensen et al. (2002, 2005) introduced the "drop model", where chemical de-

pletion occurs as a step function when certain temperature and density conditions of any underlying model are met. While this approach is simple yet quite successful, there may be cases where the abundance changes only gradually and a step function is no longer a good approximation. Doty et al. (2004) did a study of the chemical evolution of static YSO models, but aimed at more massive type objects. Recently, Tsamis et al. (2008) calculated the HCO^+, CS, and N_2H^+ abundances and spectra from a simulation of an inside-out collapsing core.

In this chapter we investigate the detailed evolution of the gas-phase and solid state abundance of CO in a collapsing, rotating core. We base our study on a numerical hydrodynamical simulation, where we follow the CO freeze-out and evaporation for a number of test particles that flow with the gas.

5.2 Tracing chemistry during disk formation

5.2.1 The physical model

Instead of using an analytic description of the gravitational collapse and subsequent disk formation, we use a grid-based two-dimensional axi-symmetric hydrodynamical scheme. The code used was described by Yorke & Bodenheimer (1999) and we adopt in particular the J-type model described in that paper.

The initial conditions of this model are a 1 $M_\odot$ isothermal sphere with a temperature of 10 K and a power-law density slope of $\rho \propto r^{-2}$. The cloud has an outer radius of 1×10^{15} m (6667 AU), and an initial solid-body rotational perturbation of 1×10^{-13} s^{-1}. The model evolves under the action of gravity, while the temperature is solved self-consistently using an approximate radiation transfer method. Angular momentum is transferred by artificial viscosity using an α-prescription (Shakura & Sunyaev 1973).

The age of the simulated system is described in terms of the initial free-fall timescale,

$$t_{ff} = \sqrt{\frac{\pi^2 R^3}{8GM}}, \tag{5.1}$$

where M is the mass of the cloud and R is the radius. For the initial conditions in our particular simulation one free-fall time scale is 1×10^5 yr. We set the duration of the simulation to be about 2.6 t_{ff} at which point the simulation terminates due to extreme velocities close to the center. Figure 5.1 shows four time snapshots at characteristic ages. We use the same four snapshots throughout this chapter, at times of 0.0, 0.5, 1.5, and 2.5 t_{ff} (with the exception of Fig. 5.1, where we use a
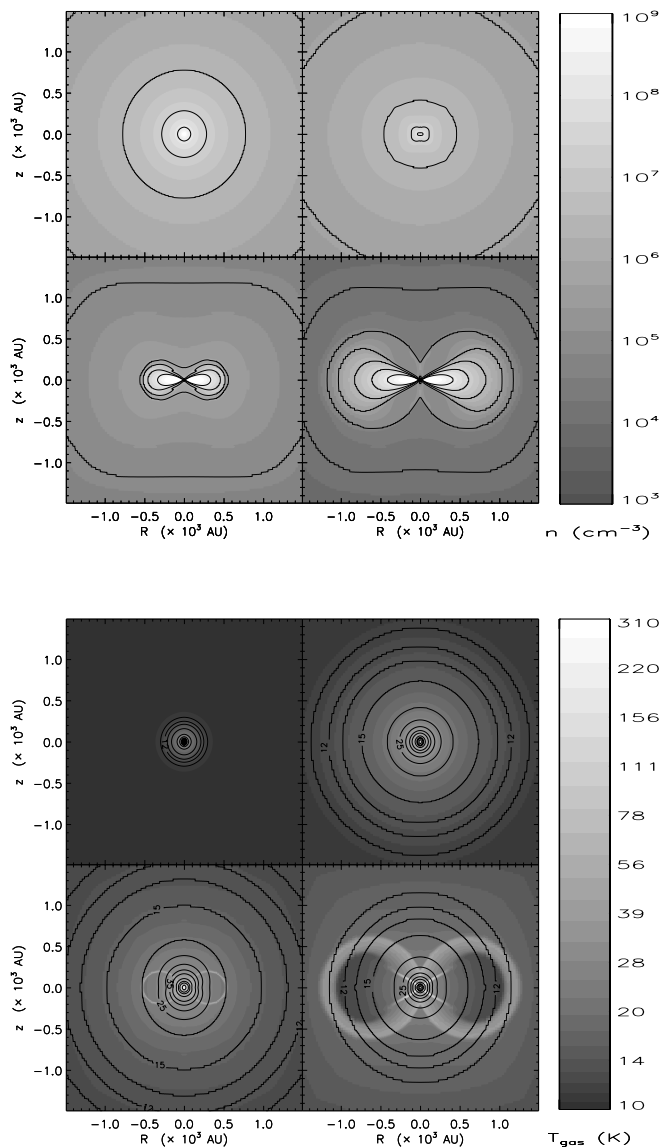
Figure 5.1: The density (upper panel) and temperature (lower panel) contours of four time snapshots of the hydrodynamical simulation. Time progresses from left to right, top to bottom at t = {0.0(6), 0.5, 1.5, 2.5} t_{ff}. In the lower panel, contour lines refer to the dust temperature, while the grey scale denote the gas temperature.
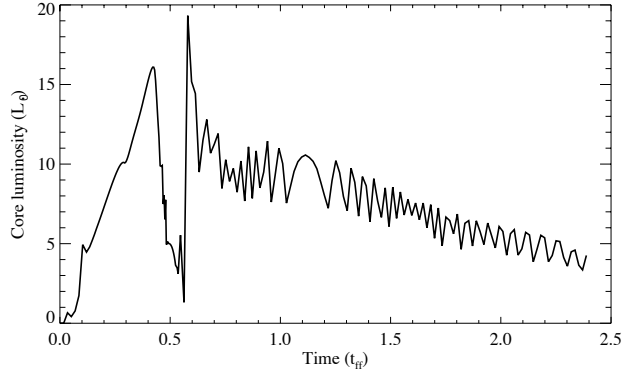
Figure 5.2: The time evolution in the luminosity of the central source in the hydrodynamical simulation. This figure compares with Fig. 7 in Yorke & Bodenheimer (1999).

few snapshots later than t = 0.0 to enable the temperature to evolve slightly from the isothermal initial condition).

The luminosity is given by the sum of the intrinsic stellar luminosity and the accretion luminosity

$$L = L_* + \frac{3}{4}\frac{GM_*\dot{M}}{R_*},$$
(5.2)

where M_* is the mass of the star, R_* is the radius of the star, and $\dot{M}$ is the mass flux onto the star. In Fig. 5.2, the total luminosity is plotted as a function of free-fall time. After an initial increase, the luminosity decline before increasing sharply again, and then continues to declines slowly for the remainder of the simulation. As described by Yorke & Bodenheimer (1999), the smooth increase and drop around 0.5 t_{ff} are controlled by the accretion luminosity, as low angular momentum material fall directly onto the star. The subsequent sharp increase in luminosity corresponds to the formation of an equilibrium disk and after then, the intrinsic stellar luminosity is dominated by the total luminosity.

The hydrodynamical simulation does not include any chemistry and we are therefore unable to relate the state of the molecules, whether in a gas phase or locked in an ice matrix, to the hydrodynamics. We determine the abundance by post-processing the result of the hydrodynamical calculations. We follow the chemistry by populating the computational domain of the first snapshot with trace

particles. These particles are massless and do not interact with each other in any way. The trace particles are positioned evenly in the radial direction and 9×10^5 particles are used. Every trace particle represents the local molecular environment and carries information about the state of the molecules (ice or gas). The particles are then allowed to follow the flow, predetermined by the hydrodynamical calculations, and the states of the particles is updated as temperature and density conditions change throughout the hydrodynamical simulation. Finally, the state of the trace particles are mapped back onto the hydro-grid at each output time step, so that a complete history from t=0.0 t_{ff} to t=2.5 t_{ff} of the CO abundance as function of R and z is linked to the density and temperature. Taking the CO distribution into account, we can use each of these time snapshots as input model for our two-dimensional line excitation and radiative transfer code *RATRAN* (Hogerheijde & van der Tak 2000) to predict line profiles of CO and its optically thin isotopologue $C^{18}O$.

Before proceeding with the freeze-out calculations, it is interesting to consider the dynamics of the trace particles to develop an understanding of the environments that the particles traverse. By a simple radial color coding of the particles, we can effectively visualize the flow within the hydrodynamical simulation and track how material is accreted onto the disk. Four snapshots of the particle distribution are shown in Fig. 5.3 where the shading of the particles refers to their initial distance from the center. The disk is seen to be layered vertically rather than radially, which is somewhat counterintuitive. The vertical layering occurs because material connects to the disk from above. As the disk spreads viscously due to conservation of angular momentum, a shock front propagates outwards, pushing aside infalling material. The only possible path for the particles is therefore upwards and over the disk lobe until they can rain down onto the disk at smaller radii. This rolling motion is also reflected in the strong vertical mixing inside the outer disk. However, this behavior may be an artifact of the two-dimensional nature of the hydrodynamical code. In a 3D simulation, particles should also dissipate in the azimuthal direction, which would probably change their motion.

5.2.2   Freeze-out and evaporation

Molecular gas abundances in general depend on reaction rates and phase transitions. However, under the physical conditions present in our model, only the latter has any significant impact on the CO abundance. The state of CO is governed by rate equations. The two main mechanisms are depletion, where gas phase molecules freeze-out onto grains, and desorption, where solid state molecules evaporate into the gas phase.
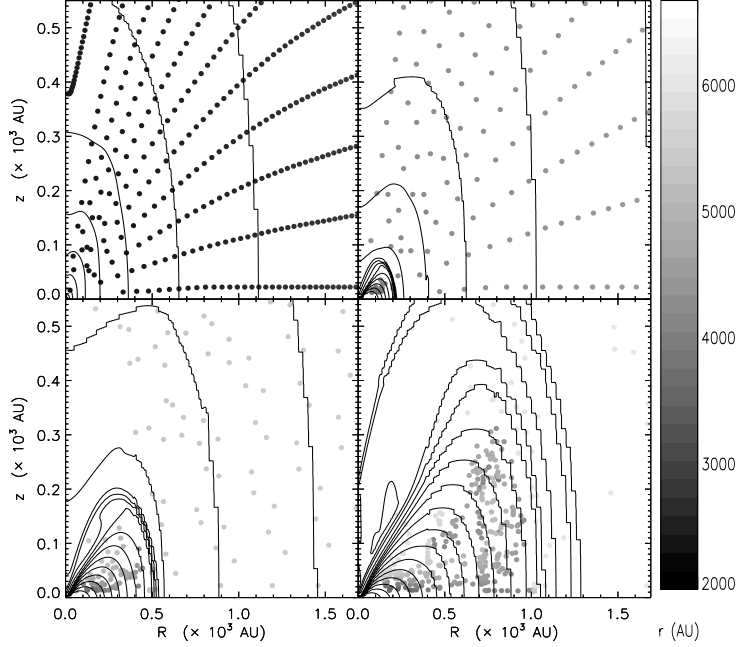
Figure 5.3: Trace particle motion in the hydrodynamical simulation. The particles are shaded according to their initial radial position. Contour lines describe the density. The vertical grey scale bar shows the particles initial distance from the center. The four panels (from the top-left to bottom-right) show the particle positions at t=0.0, 0.5, 1.5, and 2.5 t_{ff}.

The depletion rate λ used here is given by the equation (e.g. Charnley et al. 2001),

$$\lambda = \pi a^2 \sqrt{\frac{8kT_g}{\pi m_{CO}}} n_{\mathrm{grain}}, \tag{5.3}$$

where T_g is the gas temperature, m_{CO} is the mass of a CO molecule, and n_{grain} is the grain number density, assuming a grain abundance of 1.33×10^{-12} relative to the hydrogen nucleon density. We assume a mean grain size of $0.1 \mu m$. We also assume a sticking probability of unity. A similar equation can be written for the desorption of molecules. The thermal desorption rate is given by Watson &

Salpeter (1972),

$$\xi_{th} = \nu(X)e^{\left(\frac{-E_b(X)}{k_B T_d}\right)},$$ (5.4)

where k_B is the Boltzmann constant, T_d is the dust temperature, $\nu(X)$ is the vibrational frequency of X in its binding site (Hasegawa et al. 1992), and $E_b(X)$ is the binding energy of species X onto the dust grain. We assume a default binding energy of 960 K, but other values, corresponding to mantles that do not consist of pure CO ice, are explored in Sect. 5.3.4.

A second desorption mechanism that is taken into account is cosmic-ray induced desorption. This mechanism was first proposed by Watson & Salpeter (1972). Energetic nuclei might eject molecules from grain surfaces by either raising the temperature of the entire grain or by spot heating close to the impact site. The formulation of Hasegawa & Herbst (1993) is used to calculate the cosmic ray desorption rate,

$$\xi_{cr} = 3.16 \times 10^{-19}\xi_{th}\Big|_{T_d=70K}.$$ (5.5)

Cosmic ray desorption can be added to the thermal desorption, effectively preventing a depletion of 100% under any condition.

By considering the depletion and desorption rates and defining f_d to be the normalized fractional depletion, we can write an equation for f_d,

$$\frac{df_d(\mathbf{r}, t)}{dt} = \lambda(\mathbf{r}, t)f_d(\mathbf{r}, t) - \xi(\mathbf{r}, t)(1 - f_d(\mathbf{r}, t)),$$ (5.6)

in which we implicitly adopt the boundary condition that the sum of CO molecules in the solid state and gas phase is constant.

Equation 5.6 general and the rate functions can be changed readily to describe other reactions. van Weeren (2007) shows that in principle an entire set of these equations can be solved simultaneously using gas phase reaction rates such as the UMIST database (Woodall et al. 2007), although computational demand becomes an issue for a full chemical network.

5.3   Results

To obtain abundance distributions, we evaluate Eq. 5.6 using the gas temperature T_g, the dust temperature T_d, and the mass density, assuming that H_2 is the main mass reservoir and that the gas-to-dust ratio is 100:1, from the hydrodynamical

simulation. We assume that the cloud has been in hydrostatic equilibrium prior to collapse for 3×10^5 yr ($=1 \times 10^{13}$ s). The density profile before collapse is given by a spherical power-law of uniform temperature described in Sect. 5.2. Starting with a pure gas phase abundance of 2×10^{-4} CO molecules relative to H_2, we allow the abundance to evolve for 3×10^5 yr with a constant temperature of 10 K and a static density profile. The new CO abundance then serves as the initial condition for the collapse, i.e. the start of the hydrodynamical simulation, which defines t = 0. In the following, we present three different ways to obtain the abundance profiles.

5.3.1   Model 1: Drop abundance

This approach is denoted the drop abundance model, because it follows directly from the method presented by Jørgensen et al. (2005). In this approach, we do not solve Eq. 5.6, but consider the rate equations 5.3 and 5.4. The rate equations are inverted to obtain a characteristic timescale, and, at any given time in the simulation, this timescale is evaluated based on the current density and temperature conditions. If the freeze-out timescale is shorter than the evaporation time scale, the gas phase abundance drops to a preset level (which is sufficiently low, i.e. several orders of magnitude) but if the actual age of the cloud is shorter than the freeze-out timescale, the gas phase abundance is kept at its initial value. Using this approach, the resulting profile is a step function where all CO is either in the gas phase or in the solid state. The movement of the trace particles does not affect the result since the abundance is determined only from the current local conditions. By ensuring that the abundance decreases by only two or three orders of magnitude and not to zero, the effect of cosmic ray desorption is modeled implicitly, even though conditions for freeze-out are met.

The result is shown in Fig. 5.4. The top panel shows the radial abundance profile along the disk mid-plane (z=0), while the lower panel shows the two dimensional distribution. The result of this drop abundance approach supports the idea of an evolution in the CO abundances from a pre-stellar core to a Class I object, as proposed by Jørgensen et al. (2005). The maximum size of our depleted zone is ~6000 AU, just before the collapse sets in, and it then shrinks to ~500 AU (when averaged in radial and polar directions) as the cloud collapses and the disk is formed. The inner evaporated zone has a radius of ~1000 AU, in agreement with values derived in Jørgensen et al. (2005).
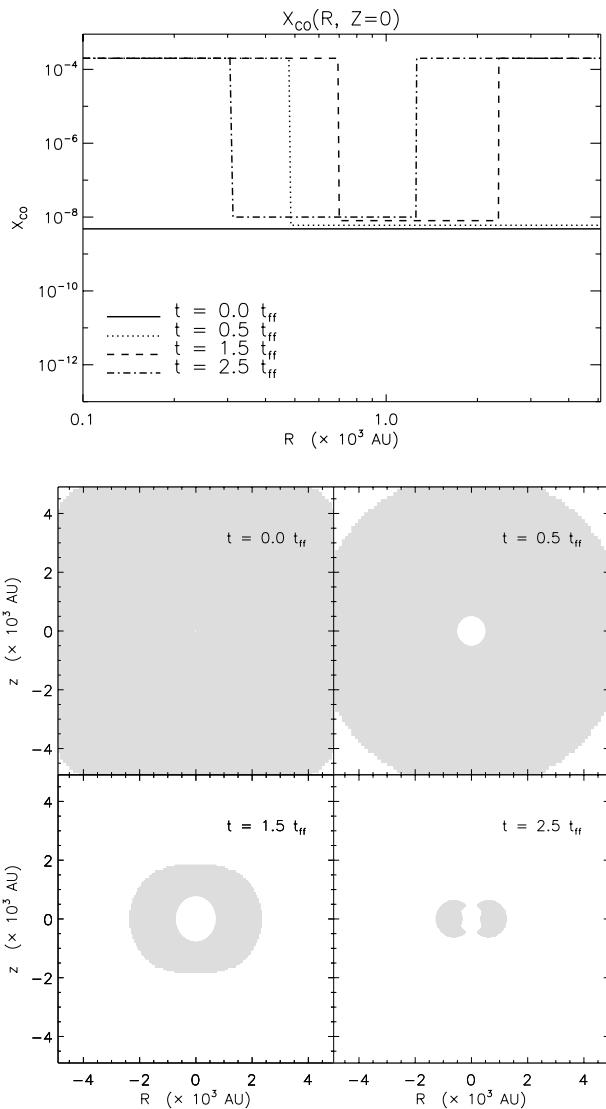
Figure 5.4: This figure shows the abundance distribution of Model 1. The top panel shows the radial abundance profile through the mid-plane of the disk. The bottom panel shows the spatial abundance distribution. The shaded area is where molecules are frozen out. The unit on the y-axis of the top panel is fractional abundance with respect to H_2.

5.3.2 Model 2: Variable freeze-out

The second method is similar to Model 1 except that instead of using timescales, we use the actual rate equations that allow the trace particles to be in a mixed state. The values for λ and ξ are calculated for all $\mathbf{r}$ using the current $n(\mathbf{r})$ and $T(\mathbf{r})$, and Eq. 5.6 is solved to obtain the fraction of gas phase CO to solid state CO for each trace particle position. In this model, we still do not consider the history of the trace particles and the motion of the particles is therefore irrelevant and the time dependence of ξ and λ in Eq. 5.6 becomes negligible. Plots of the abundance distributions are shown in Fig. 5.5. The profiles of Model 2 are similar to those from Model 1, except for the gradual change from pure gas phase to pure solid state. The inner edge in particular is described well by the step function of Model 1 because of the exponential factor in the evaporation, described by Eq. 5.4. The main difference between the two models is the outer edge, and in particular at earlier times, where the gradient is more shallow.

5.3.3 Model 3: Dynamical evolution

Our final model takes the motion of the trace particles and their chemical history into account. Freeze-out and evaporation rates are calculated dynamically for each time step and the composition of the particles is used as the initial conditions for Eq. 5.6. For example, the depletion in a certain area represented by a trace particle depends on where this particle has originated, which we know because the trace particles follow the flow calculated in the hydrodynamical simulation. Two trace particles may pass by the same region at the same time and experience the same desorption and depletion conditions. However, they may have originated in different areas; for example, one particle may have originated in a warmer region and the other may have travelled from a colder region, and they will then leave the location with different compositions.

Figure 5.6 shows the abundance distributions for this model. Surprisingly, the profiles do not differ significantly from those of Model 2. A difference only occurs when the dynamical timescale is comparable to the chemical timescale. In this case, a gas phase trace particle may move out of a depletion zone more rapidly than depletion can make any significant change to its composition, or vice versa. The evaporation front around the disk is also sharper with respect to Model 2, which causes Model 3 to appear almost like a step function in the final part of the simulation.
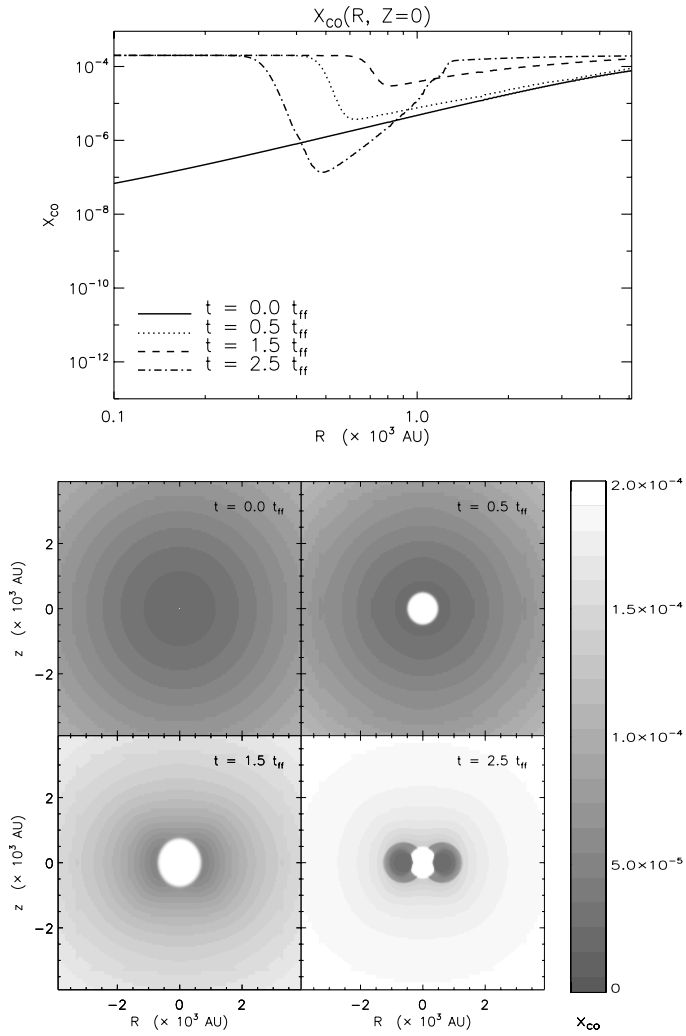
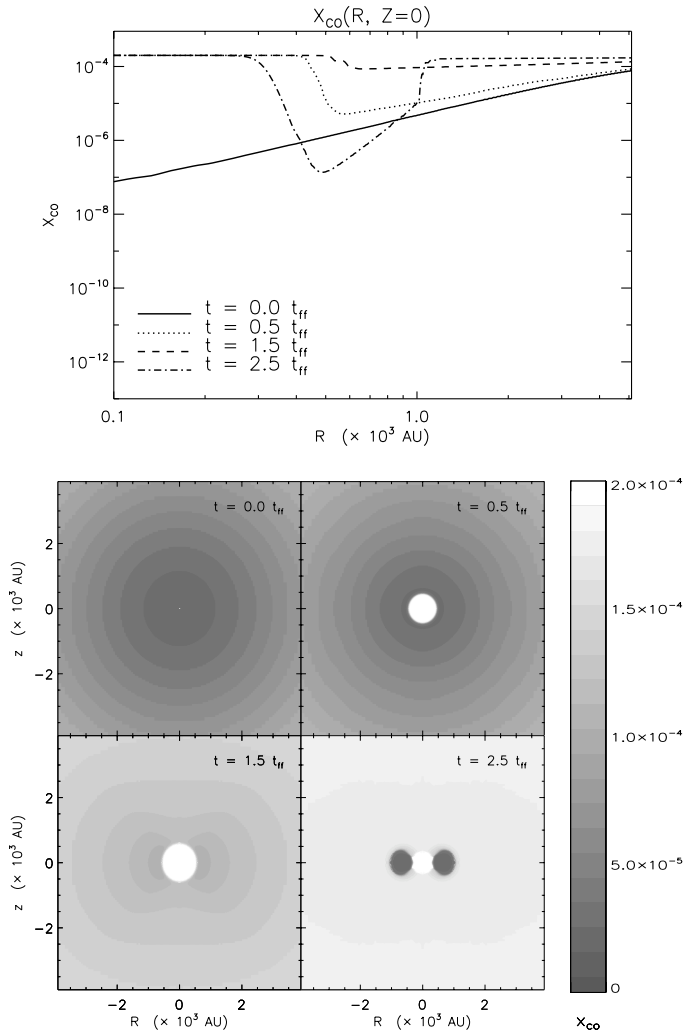Figure 5.5: Abundance distribution of Model 2. Otherwise identical to Fig. 5.4.

Figure 5.6: Abundance distribution of Model 3. Otherwise similar to Fig. 5.4.

5.3.4   Cosmic ray desorption and increased binding energy

We are now going to investigate the effects of excluding the cosmic ray desorption term (Eq. 5.5) to see what effect this mechanism has on the abundances. We also increase the CO binding energy E_b in Eq. 5.4 to emulate different ice mantle compositions. In the following, we use Model 3 as a template.

Cosmic ray desorption ensures that depletion can never reach 100% as long as cosmic rays are able to penetrate the cloud and remove molecules from the ice matrix. If no other desorption mechanisms are present, dark cold molecular clouds will have a high degree of depletion since thermal desorption is largely ineffective at low temperatures. However, Caselli et al. (1999) found no evidence for high depletion factors and therefore some other desorption mechanism (such as, for instance, cosmic ray desorption) must play a certain role in these environments. However, to observe exactly how much evaporation cosmic rays account for, we calculate Model 3 without the cosmic ray desorption term. Figure 5.7 shows these abundance distributions. The profiles are similar to Model 3, but the amount of depletion is, as expected, about three orders of magnitude higher.

Including cosmic ray desorption obviously has a significant impact on the amount of gas phase molecules in the cloud, raising the gas-phase abundance substantially. However, the effect of cosmic ray desorption can be balanced by a higher binding energy between the molecule and grain surface. For example, raising the binding energy from 960 K to 1740 K compensates almost entirely for the effect of cosmic ray desorption, when the depletion is averaged over the entire model (Figure 5.8).

An increased binding energy applies when the CO ice mantle is mixed with other species, typically water ice or NH_3 ice (Fraser et al. 2004). A spread in binding energies also occurs when the ice surfaces are not even, e.g. for differently layered ices, varying mantle thicknesses and rough surfaces. If the grains are more fractal, with cavities that can trap CO molecules, it becomes more difficult to desorb the molecules, which effectively raises the binding energy. Laboratory experiments of Collings et al. (2004) detected multiple peaks in the CO desorption spectrum, implying a range of binding energies. In Fig. 5.8, the innermost evaporation zone is smaller by a significant margin throughout the simulation, when the binding energy is increased, in comparison to when cosmic rays are not present; this implies that the two effects can be discriminated by high-resolution observations.
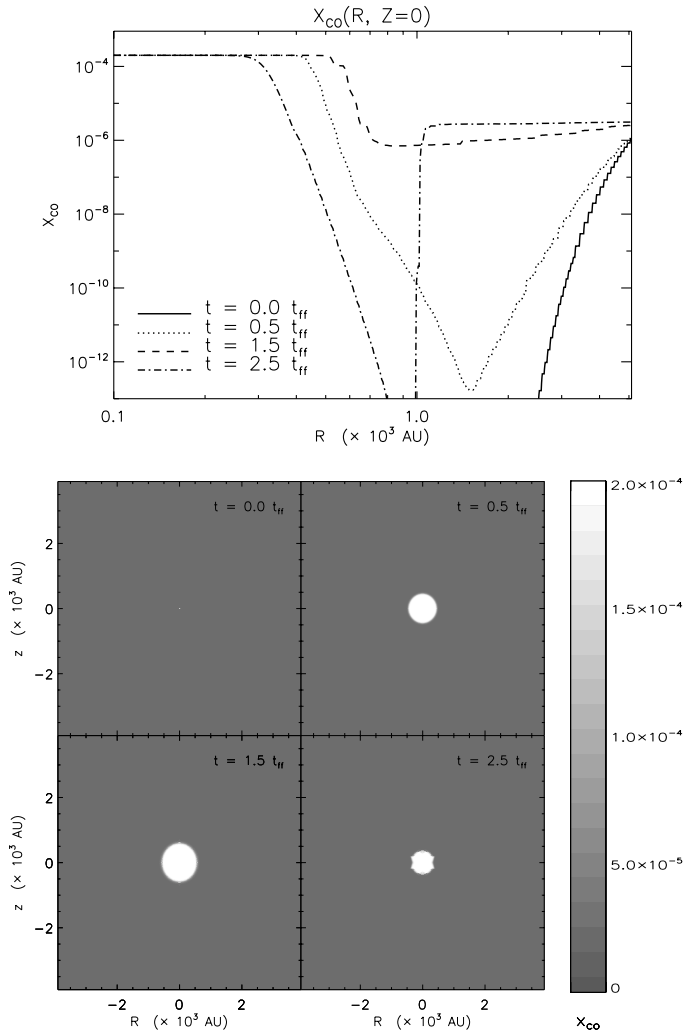
Figure 5.7: Abundance distribution of Model 3 without cosmic ray desorption and the default binding energy of 960 K. Otherwise similar to Fig. 5.4.
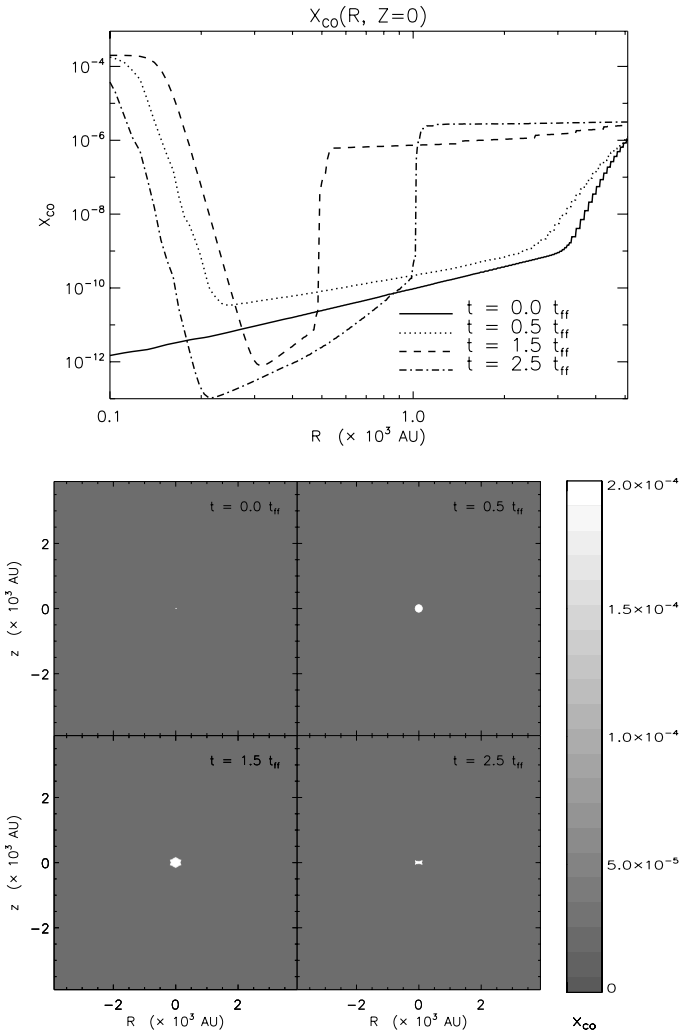
Figure 5.8: Abundance distribution of Model 3, including cosmic rays, but with a CO binding energy of 1740 K. Otherwise similar to Fig. 5.4.

5.3.5 Comparison to observations

We compare our results with observations of CO abundances and depletion factors. The fractional depletion f_d of CO for the various models are shown in Fig. 5.9. The highest depletion factors occur at the end of the pre-stellar core phase just before collapse. Observations show that depletion factors decrease with decreasing envelope mass (Jørgensen et al. 2002). We observe the depletion decrease after the core begins to collapse due to CO evaporation close to the protostar. At the same time, the envelope density decreases, which also lowers the global fractional depletion defined to be the ratio of the total number of gas phase CO molecules to H_2 molecules in the entire model.

Freeze-out in the disk is most pronounced for Model 3, which includes cosmic ray desorption and a high CO binding energy. The same model but with a binding energy of 960 K provides a low depletion factor at the onset of the collapse. Although low values of f_d have been measured (e.g. Bacmann et al. 2002), most observations point toward a higher value, $f_d \geq 10$, in pre-stellar cores (e.g. Crapsi et al. 2004; Bergin et al. 2002; Jessop & Ward-Thompson 2001). The low value of f_d that we find implies that either the binding energy is higher than 960 K or that we overestimate the cosmic ray desorption rate. Shen et al. (2004) demonstrated that the importance of cosmic ray heating was overestimated by previous authors. A third possibility is that CO can be converted into other species, resulting in a lower abundance, but since we only model CO we cannot quantify this effect.

As mentioned above, an observational correlation was found between the amount of depletion and envelope mass. The CO abundance declines when going from a pre-stellar core, through the Class 0 phase, to a Class I object. We compare our results with the data presented by Jørgensen et al. (2002), who derived global envelope abundances for 18 sources. Their result is shown in Fig. 5.10, where open symbols are Class I objects, closed diamonds are Class 0 objects, and the filled squares are pre-stellar cores. Superposed on the data are curves based on our models. In the linear approximation, our models follow the same trend. The observations show no evidence of freeze-out in the Class I objects but the number of sources of this type is small and the derived envelope masses and abundances are uncertain. We also expect some intrinsic scatter due to the unique environments and characteristics of each source. The drop abundance model and Model 3, including cosmic rays and a low binding energy, have too high gas-phase CO abundances (or too little depletion). Unfortunately, our simulation begins with only one solar mass and we are therefore unable to study the more massive Class 0 and pre-stellar cores.

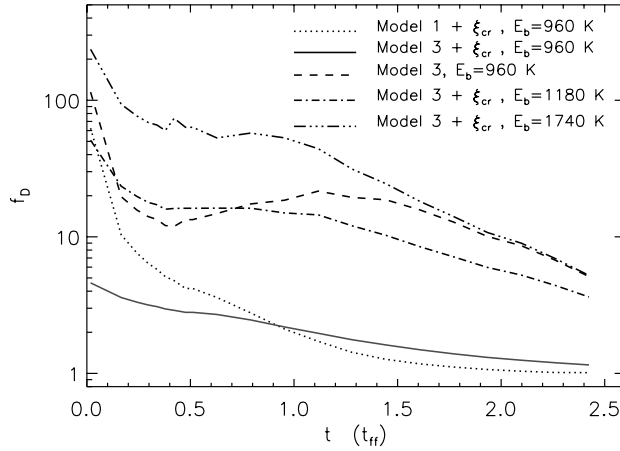We can also calculate gas column densities based on our abundance distribu-

Figure 5.9: The global fractional depletion in the various models. The small bump in the curves around 0.5 t_{ff} is due to a change in the luminosity output of the central source as the disk is formed.
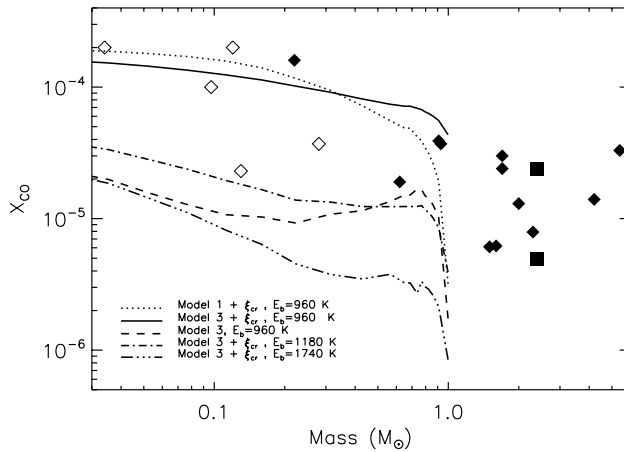

Figure 5.10: Abundance as a function of envelope mass. Also shown in this plot are data points taken from Jørgensen et al. (2002, 2005). The open symbols are Class I objects, the filled diamonds are Class 0 sources and the filled squares are pre-stellar cores.
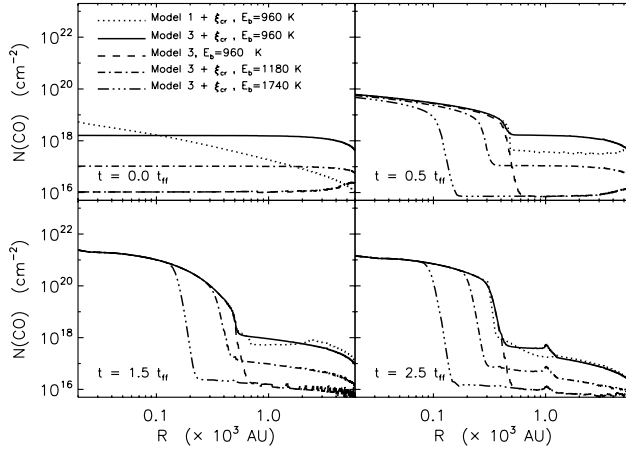
Figure 5.11: CO gas column densities of the models discussed in this chapter. These profiles are seen through a pencil beam, and need to be convolved with an appropriate beam in order to be directly compared to observations.

tion models. Vertically integrated column densities, $N_{CO} = \int n_{CO}(z)dz$, are shown at four different free-fall times in Fig. 5.11. The models differ mainly in the position of the evaporation front due to the different binding energies used. The column density profiles at t = 0 can be compared with those presented by Aikawa et al. (2001, 2003, 2005). Although our underlying density model is different, the column densities are comparable, differing by an order of magnitude or less. Aikawa et al. (2001) measured flat profiles toward the core center or slight drops in the column within ~5000 AU, which is similar to the results of our models. The only exception is our drop abundance model (Model 1), which has an increasing column density toward the center. The drop occurs at ~6000 AU, and within a 6000 AU radius we have a constant abundance. The n_{H_2} density decreases with the inverse square of the radius, which means that the column density of CO increases toward the core center. This disagrees with observations (e.g. Tafalla et al. 2004) where flat or decreasing integrated intensity profiles are found at core centers and can be interpreted as a drop in the column density.

At $t > 0$, column densities decrease by about three orders of magnitude from the center toward the freeze-out zone in the disk, comparable to Aikawa et al. (1996), although column densities in our results are in general more than one order of magnitude higher. This can be explained by the differences in the adopted disk
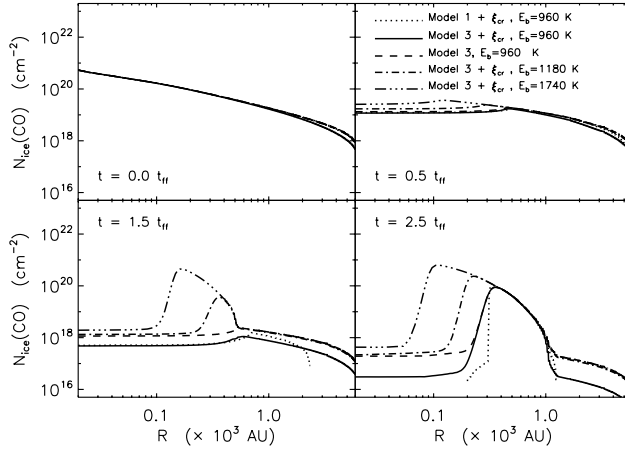
Figure 5.12: Same as Fig. 5.11 but for CO ice column densities.

masses. A typical value adopted for disk masses is 10^{-2} $M_\odot$, while the disk in our simulations increases to an unrealistically high mass of about 0.4 $M_\odot$. Our column density distributions are also more complicated because we do not use a simple analytic description of a non-evolving disk. Aikawa et al. (1996) measured drops in column density due to freeze-out in the disk around 200 – 300 AU, similar to our results for 100 – 500 AU, depending on the model used.

In a similar way, we can calculate the column densities for the CO bound to ice. Plots of the ice column densities are shown in Fig. 5.12. Before collapse, the column density of CO ice increases inwards due to the shorter freeze-out timescales. When the central temperature rises, the column density flattens and drops, while in the protoplanetary disk the column density increases sharply. Overall, the column density drops in the envelope because of the decreasing density (which also results in a lower freeze-out rate). It is difficult to compare these results with observations since cold (unrelated) clouds, where CO is frozen out, often are located in front of protostars. Observed column densities of CO ice are often approximately 10^{18} cm^{-2} (Pontoppidan 2006) in reasonable agreement with our results.

5.3.6 Emission lines

Simulated spectral lines are a direct way to test our models because they can be compared directly to observed spectra. As mentioned in Sect. 5.2, we use the

hydrodynamical time snapshots including the abundance distribution mapped onto the original grid as input models for our two-dimensional molecular excitation code *RATRAN*. This code solves the level population using an accelerated Monte Carlo method, which is then ray-traced to create frequency dependent intensity maps. After beam convolution, spectral profiles can be extracted from these and directly compared with observations. We add a mean field of 0.2 km s^{-1} to the snapshots during the radiation transfer calculations to emulate the presence of micro-turbulence.

An in-depth analysis of spectra based on the hydrodynamical simulation was already presented in Chapter 3 and only example spectra for the abundance models derived in this chapter are shown here. Figure 5.13 shows the CO $J = 3$–2 transition of the four time-snapshots used in previous figures. The top three panels correspond to the three abundance models including cosmic ray desorption, while the lower three panels show spectra based on Model 3 without cosmic ray desorption and with increased binding energies. Figure 5.14 has a similar layout, but for the less optically thick isotopologue C^{18}O. For comparison, CO and C^{18}O spectra, calculated with a constant abundance profile (X(CO)=2×10^{-4}) are shown in Fig. 5.15. All spectra are viewed at 90° inclination (edge-on; similar to the orientation of the model in Fig. 5.1), and they were convolved with a 10″ beam, a typical value for single-dish sub-millimeter telescopes. A distance of 140 pc (Taurus star forming region) is adopted. We use an isotopic ^{16}O:^{18}O ratio of 560 (Wilson & Rood 1994) to calculate all C^{18}O spectra.

We observe that the spectra in the top row of Fig. 5.13 are similar to each other and also to the constant abundance profiles in Fig. 5.15. The reason is that CO becomes optically thick before the abundance declines and is therefore independent of the underlying abundance model. Consequently, we are unable to use CO spectra to distinguish between the three models and cannot determine the depletion factor using CO. An exclusion of cosmic rays or increase in the binding energy lowers the intensity of the spectra, and in this case CO can be used to constrain the models.

The line profile of the earliest snapshot (the thinnest line) is observed to have a boxy shape with a flat line center. This is entirely due to the hydrodynamical model, which has not yet evolved from its initial isothermal state in the region where the line gets optically thick. Basically we probe the same temperature through a range of velocities, which produce the flat top. The line width in the earliest snapshot of Fig. 5.13 is also considerably narrower than for the other lines. This is because the velocities in the model have not yet had the time to increase from the initial solid body rotation speed.
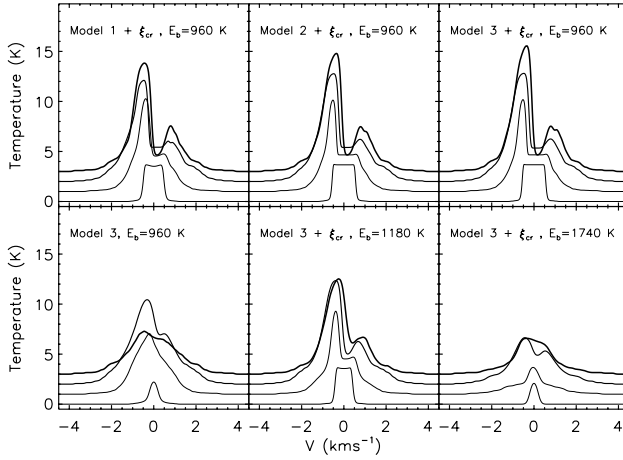
Figure 5.13: Time series of CO 3–2 spectra. The top three panels show the three different abundance models. The three lower panels show Model 3, including cosmic ray desorption using three different binding energies. Time is shown by increasing line thickness and the four lines correspond to the four adopted time snapshots (0.0, 0.5, 1.5, and 2.5 t_{ff}). Each line has been offset by 0.5 K.
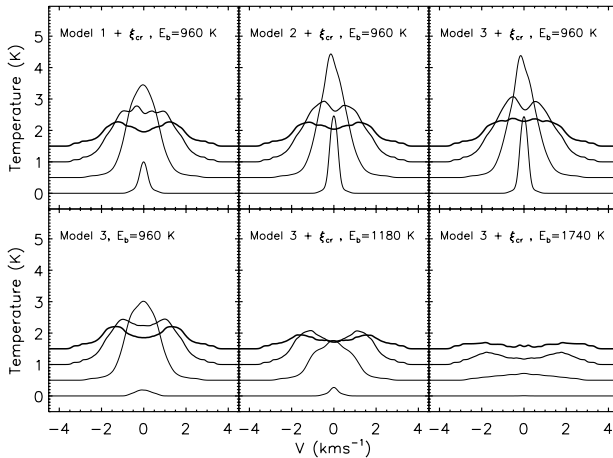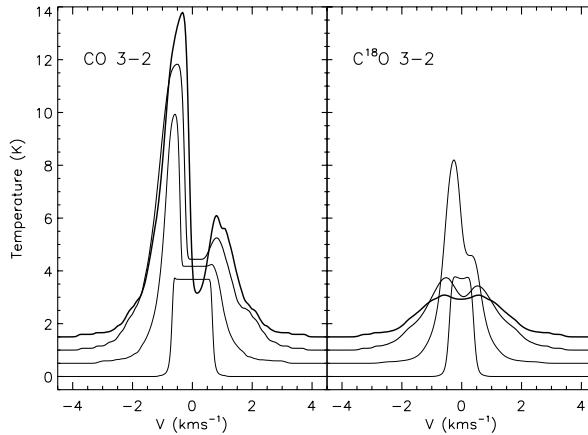

Figure 5.14: Similar to Fig. 5.13 but for $C^{18}O$ 3–2.

Figure 5.15: Time series of CO and $C^{18}O$ spectra with a constant abundance of 2×10^{-4}. Time is represented by increasing line thickness.

The $C^{18}O$ spectra however differ considerably from those derived for a constant abundance model. When the three abundance models are compared, they also differ, although to a lesser extent, from each other. This is because the lines are optically thin and a drop in abundance has a direct impact on the spectral line, no matter at what radius the drop occurs.

The spectra shown here all simulate single-dish measurements, where the emission of the source has been smeared out by a relatively large beam. If an interferometer is used instead, beam sizes smaller than 1″ can be achieved, which allows us to map the line-of-sight column densities. With these observations, it should be possible to map abundance distributions of optically thin species and constrain our models.

5.4   Discussion

The abundance profiles presented here depend on the adopted hydrodynamical model. While we believe that our results are general applicable, details, such as the precise timescale and absolute values of the fractional depletion, depend on the initial conditions of our simulations such as mass and angular momentum and the particular hydrodynamical scheme used.

A main concern of the hydrodynamical simulation is the internal radiation

transfer module used to calculate the temperature structure of the simulation. This is done with an approximate method known to overestimate the dust temperature by a few Kelvins compared with calculations by more accurate continuum radiation transfer codes (Visser, priv. comm.). While a few Kelvin may have little or no effect on the hydrodynamics and therefore the evolution of the cloud, it can certainly affect the evaporation front, which has a strong temperature dependence. This will alter the detailed behavior of the abundances, but it will not change the general trends discussed in this chapter.

Although we have considered only the CO gas-phase abundance, as mentioned in Sect. 5.2, our method can be easily extended to include other species and even surface reactions. However, attempting to calculate the entire chemical network is considerably more computationally demanding. Where the CO models can be completed in a few hours on a standard desktop computer using 9×10^5 trace particles, a test simulation with the entire chemical network indicated that it would take a factor of 100 longer to complete using a factor of 1000 fewer trace particles. Nevertheless, such large-scale chemical models present a powerful way to obtain realistic abundance profiles for hydrodynamical simulations which instruments such as the Atacama Large Millimeter Array (ALMA) will be able to test at high spatial resolution.

5.5   Conclusion

We have investigated different scenarios for the depletion of CO in a collapsing cloud. We have used a hydrodynamical code to describe the dynamical evolution of the cloud and the chemistry has been solved using a trace particle approach.

Of the various models shown in Sect. 5.3, the model which excludes cosmic ray desorption and those with higher binding energies provide the most extreme results. The drop abundance model provides a good approximation to Model 2 and 3. Therefore, if it is possible to describe observations, using a drop profile, as was achieved by Jørgensen et al. (2005), it should be possible to run a hydrodynamical simulation with customized initial conditions, so that it reproduces this profile and thereby putting an observational constraint on the hydrodynamics. In cases where an analytical model has been used, the drop abundance approximation has also proven to be good.

We furthermore conclude that the freeze-out chemistry has little effect on optically thick spectral lines, especially when observed at low resolution. It is not unreasonable to model these lines using a constant abundance model regardless of the depletion. However, we should be careful when using optically thin lines

to determine the average gas phase abundance that should be used in a constant abundance model, since the average abundances derived from these lines depend on the freeze-out chemistry. The maximum discrepancy between the flat abundance profile model (Fig. 5.15) and the freeze-out models shown in Fig. 5.14 is a factor of three in the integrated intensity. Such a change in the average abundance does not affect the optically thick lines a lot, so depending on the accuracy required, it may not be unreasonable to use a flat abundance distribution to model data in which freeze-out is present.

Finally, the effect of chemical depletion is enhanced considerably when the resolution of the observations increases, implying that it becomes more important to model the abundance profiles accurately. This will be particularly important for future ALMA observations, which will have a resolution of $\sim 0.01''$, for which the spatial detail will be significantly higher and precise abundance models will be crucial for the accurate interpretation of the data.

Acknowledgements

References

Adams, F. C., Lada, C. J., & Shu, F. H. 1987, ApJ, 312, 788

Aikawa, Y., Herbst, E., Roberts, H., & Caselli, P. 2005, ApJ, 620, 330

Aikawa, Y., Miyama, S. M., Nakano, T., & Umebayashi, T. 1996, ApJ, 467, 684

Aikawa, Y., Ohashi, N., & Herbst, E. 2003, ApJ, 593, 906

Aikawa, Y., Ohashi, N., Inutsuka, S.-i., Herbst, E., & Takakuwa, S. 2001, ApJ, 552, 639

Bacmann, A., Lefloch, B., Ceccarelli, C., et al. 2002, A&A, 389, L6

Bergin, E. A., Alves, J., Huard, T., & Lada, C. J. 2002, ApJ, 570, L101

Caselli, P., Walmsley, C. M., Tafalla, M., Dore, L., & Myers, P. C. 1999, ApJ, 523, L165

Charnley, S. B., Rodgers, S. D., & Ehrenfreund, P. 2001, A&A, 378, 1024

Collings, M. P., Anderson, M. A., Chen, R., et al. 2004, MNRAS, 354, 1133

Crapsi, A., Caselli, P., Walmsley, C. M., et al. 2004, A&A, 420, 957

Doty, S. D., van Dishoeck, E. F., & Tan, J. 2004, in Bulletin of the American Astronomical Society, Vol. 36, Bulletin of the American Astronomical Society, 1505

Draine, B. T. & Lee, H. M. 1984, ApJ, 285, 89

Evans, II, N. J. 1999, ARA&A, 37, 311

Fraser, H. J., Collings, M. P., Dever, J. W., & McCoustra, M. R. S. 2004, MNRAS, 353, 59

Hasegawa, T. I. & Herbst, E. 1993, MNRAS, 261, 83

Hasegawa, T. I., Herbst, E., & Leung, C. M. 1992, ApJS, 82, 167

Hogerheijde, M. R. & van der Tak, F. F. S. 2000, A&A, 362, 697

Jessop, N. E. & Ward-Thompson, D. 2001, MNRAS, 323, 1025

Jørgensen, J. K., Schöier, F. L., & van Dishoeck, E. F. 2002, A&A, 389, 908

Jørgensen, J. K., Schöier, F. L., & van Dishoeck, E. F. 2005, A&A, 435, 177

Lada, C. J. & Wilking, B. A. 1984, ApJ, 287, 610

Lee, J.-E., Bergin, E. A., & Evans, II, N. J. 2004, ApJ, 617, 360

Pontoppidan, K. M. 2006, A&A, 453, L47

Shakura, N. I. & Sunyaev, R. A. 1973, A&A, 24, 337

Shen, C. J., Greenberg, J. M., Schutte, W. A., & van Dishoeck, E. F. 2004, A&A, 415, 203

Tafalla, M., Myers, P. C., Caselli, P., & Walmsley, C. M. 2004, A&A, 416, 191

Tsamis, Y. G., Rawlings, J. M. C., Yates, J. A., & Viti, S. 2008, ArXiv e-prints, 803

van Weeren, R. J. 2007, Master's thesis, Leiden University

Watson, W. D. & Salpeter, E. E. 1972, ApJ, 175, 659

Wilson, T. L. & Rood, R. 1994, ARA&A, 32, 191

Woodall, J., Agúndez, M., Markwick-Kemper, A. J., & Millar, T. J. 2007, A&A, 466, 1197

Yorke, H. W. & Bodenheimer, P. 1999, ApJ, 525, 330

Chapter **6**

The kinematics of NGC1333-IRAS2A – a true Class 0 protostar

Abstract

Low-mass star formation is described by gravitational collapse of dense cores of gas and dust. At some point during the collapse, a disk is formed around the protostar and the disk will spin up and grow in size as the core contracts because of angular momentum conservation. The question is how early in the process the disk formation occurs. In this chapter we aim to characterize the kinematical state of a deeply embedded, Class 0 young stellar object, NGC1333–IRAS2A, based on high resolution interferometric observations of HCN and $H^{13}CN$ $J = 4$–3 from the Submillimeter Array, and test whether a circumstellar disk can be detected based on gas kinematic features. We adopt a physical and chemical model which has been shown to describe the object well and obtain a fit of a parameterized model of the velocity field, using a two-dimensional radiation transfer code. The parameterization and fit to the high resolution data make it possible to characterize the central dynamical mass and the ratio of infall velocity to rotation velocity. We find a large amount of infall and very little rotation on all scales. The central object has a relatively low mass of 0.25 $M_\odot$. Our best fit is consistent with both the interferometer data and single-dish observations of the same molecule. As a Class 0 object with a low stellar mass compared to the envelope mass, we conclude that NGC1333–IRAS2A is consistent with the theoretical prediction that Class 0 objects represent the very earliest stages of star formation. The large amount of infall relative to rotation also suggests that this is a young object. We do however find the need of a central compact component on scales < 100 AU based on the continuum data, which suggests that disk formation happens very shortly after the initial gravitational collapse. The data do not reveal a distinct velocity field for this 0.1 $M_\odot$ component.

Christian Brinch, Jes K. Jørgensen, and Michiel R. Hogerheijde
Submitted to Astronomy & Astrophysics

6.1 Introduction

An open question in the subject of low-mass star formation is how and when the velocity field of the molecular gas in the protostellar envelope changes from being dominated by radial infall to being dominated by Keplerian rotation. It is well known that in the early stages of star formation, gas falls toward the center as gravitational collapse sets in (Shu 1977). Cores, however, are known to carry a certain amount of rotational energy (Goodman et al. 1993), so as a core contracts, the net angular momentum spins it up, flattening the infalling material in the direction of the rotation axis (Cassen & Moosman 1981; Terebey et al. 1984; Adams et al. 1988; Basu 1998). After the main accretion phase, the envelope is gone and a planet forming disk with gas in Keplerian orbits is left. In chapter 3 we showed that the evolution of the velocity field, from the collapse phase to the disk phase, can be described by a single parameter, namely the radially averaged ratio of infall to rotation, which may be linked to the age of the protostar and can thus tell us about the evolutionary stage of the system.

Currently, the most widespread way to classify young stellar objects is through the classification scheme laid out by Lada & Wilking (1984) with the addition of the Class 0 by André et al. (1993). These classes are based on the shape of the spectral energy distribution with the addition that Class 0 objects are defined as protostars with $M_* < M_{env}$, which is equivalent to the original empirical definition of Class 0 objects as stars with a high submillimeter flux relative to their bolometric luminosity. Furthermore, for Class 0 objects, the mass of disks is usually thought to be much less than the mass of the envelope. The mass of the central object is not easily measured, but one way to estimate it is by determining the velocity field, since the magnitude of the velocity vectors are determined by the central mass. In this chapter, we study the kinematics of the deeply embedded NGC1333-IRAS2A protostar using subarcsecond resolution data from the Submillimeter Array (SMA) as well as detailed two-dimensional line radiative transfer modeling.

NGC1333-IRAS2 was first detected through IRAS observations by Jennings et al. (1987). Submillimeter continuum imaging has subsequently shown that it likely consists of three different objects, NGC1333-IRAS2A, -IRAS2B, and -IRAS2C, of which the two former are well isolated and detected at mid-IR wavelengths, e.g., with the Spitzer Space Telescope (Jørgensen et al. 2007b; Gutermuth et al. 2008). These sources also show compact emission in millimeter interferometric images (Looney et al. 2000; Jørgensen et al. 2004b). The third source, IRAS2C, shows relatively strong N_2H^+ emission possibly reflecting the absence of a central heating source (Jørgensen et al. 2004b). Modeling of the high angu-

lar resolution millimeter continuum observations (Looney et al. 2003; Jørgensen et al. 2004b) revealed the existence of a central compact continuum component in NGC1333-IRAS2A, likely reflecting the presence of a central circumstellar disk with a mass of $\sim 0.1 \, M_\odot$ (depending on the assumed dust temperature and opacity). NGC1333-IRAS2A was targeted as part of the PROSAC survey of Class 0 embedded protostars (Jørgensen et al. 2005b, 2007a). The 1″ resolution submillimeter continuum data (Jørgensen et al. 2005b) showed that the central compact component was resolved with a diameter of approximately 300 AU.

In this chapter we investigate the kinematical properties of IRAS2A using a global parameterization of the velocity field. We are particularly interested in the velocity structure on scales <100 AU, traced by the high resolution Submillimeter Array[1] data, where a circumstellar disk is thought to be present. The SMA instrument is ideal for this task because we can probe the warm, dense gas with high excitation lines in high resolution and thereby zoom in on the central parts of the object. We furthermore benefit from the fact that the interferometer is less sensitive to ambient cloud material.

6.2   Observations

Supplementing the SMA compact configuration data from 2004 October 17 (Jørgensen et al. 2005b), NGC1333-IRAS2A was observed in the extended configuration on 2006 January 8. The weather was good and stable during the observations with a sky opacity at 225 GHz of about 0.05. Seven of the eight SMA antennas were in the array at the time which together with the 2004 compact configuration data provide good (u, v)-coverage on baselines between 17 and 210 kλ with a few baselines at 232 to 264 kλ. The complex gains were calibrated by observations of the strong quasars 3c84 (2.2 Jy) and 3c111 (2.8 Jy) every 15 minutes.

The SMA correlator was configured with an identical setup to the compact configuration data from 2005 with 2 GHz bandwidth at 345 GHz (LSB) and 355 GHz (USB). For the lines predominantly discussed in this chapter, HCN and $H^{13}CN$ $J = 4-3$ at respectively 354.5055 and 343.3398 GHz, the spectral resolution was 0.15 km s^{-1} (HCN) and 0.30 km s^{-1} ($H^{13}CN$). With natural weighting the RMS is 0.225 (HCN) and 0.147 ($H^{13}CN$) Jy beam^{-1} in a 1 km s^{-1} wide channel with a beam size of 1.2″ × 0.8″. The initial calibration of the data was done with the SMA MIR package (Qi 2006) with additional image processing done using

---

[1] The Submillimeter Array is a joint project between the Smithsonian Astrophysical Observatory and the Academia Sinica Institute of Astronomy and Astrophysics and is funded by the Smithsonian Institution and the Academia Sinica.
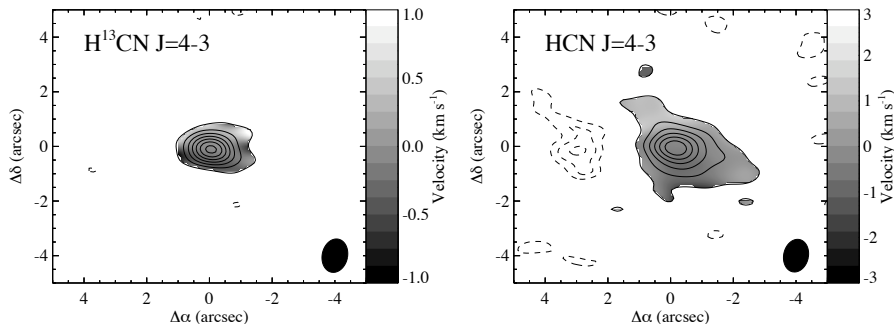
Figure 6.1: Zero (contours) and first (gray scale) moments of $H^{13}CN$ and HCN $J = 4$–3. Contour lines showing the integrated intensity begin at 3σ and increase by 3σ=2.3 Jy km s^{-1} ($H^{13}CN$) and 5.4 Jy km s^{-1} (HCN), respectively.

MIRIAD (Sault et al. 1995).

In addition to these data, we here use previously published single-dish data from the James Clerk Maxwell Telescope (Jørgensen et al. 2004b) as well as 3 mm interferometric observations from the BIMA array (Jørgensen et al. 2004a).

6.3   Results

The data have been inverted in order to reconstruct the emission distribution in the image plane, using the *invert, clean,* and *restore* routines of the MIRIAD software package. We use the natural weighting scheme during the *invert* procedure to optimize for signal-to-noise in the resulting image at a small cost of resolution. The zeroth and first moments of the image cubes, integrated intensity and velocity, respectively, have been plotted in Fig. 6.1 for both the $H^{13}CN$ line and HCN line. In this figure, the contour lines show the zeroth moment and the grey scale shows the first moment. The contours start at the three sigma level corresponding to 5.5 Jy beam^{-1} for HCN and 2.5 Jy beam^{-1} for $H^{13}CN$ and they increase linearly by three sigma in both panels. The emission is seen to be centrally peaked with only a bit of extended emission at the 3–6 σ level in HCN. This is in good agreement with the (u, v)-amplitude plots in Fig. 6.2 where HCN is seen to be resolved while $H^{13}CN$ is more compact.

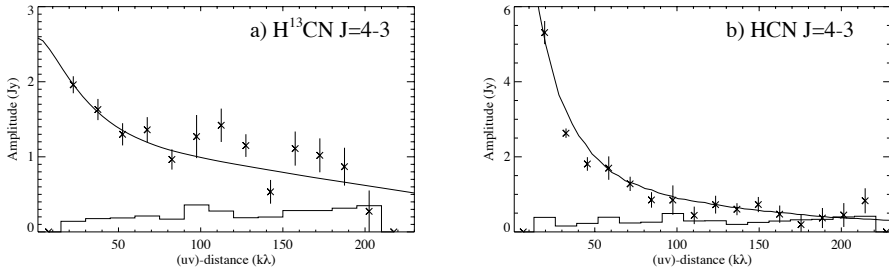When the two SMA tracks are combined we get a good (u, v)-coverage on

Figure 6.2: Averaged (u, v)-amplitudes over the velocity range of ± 3 km s^{-1} from the systemic velocity of H^{13}CN and HCN. The histogram is the expected amplitude if no signal was present. The solid line is our best fit model as discussed in Sect. 6.4.

baselines between 17 and 210 kλ. This is equivalent to emission on scales of 1.2″ to 14.8″ which, at the distance of NGC1333 (220 pc; Cernis 1990), corresponds to linear scales of 264 to 3300 AU. Some flux is also measured on scales between 232 and 264 kλ (216 to 238 AU), but at low signal-to-noise. Any emission on baselines shorter than 17 kλ is filtered out by the interferometer. Figure 6.2 shows the averaged (u, v)-amplitudes as a function of baseline between 0 and 210 kλ. In panel a) is shown the H^{13}CN $J = 4$–3 line. This panel shows that the emission on all scales up to 200 kλ is compact with only a hint of increased flux on scales below 50 kλ. The histogram indicates the expectation values if no signal were present and the full line is our best fit model, which we discuss in Sect. 6.4. Panel b) has a similar layout, but for the HCN $J = 4$–3 line. This emission is well resolved on scales below 80 kλ, but less resolved on scales above this distance. It is, however, clearly detected on all baselines with an almost constant signal-to-noise, even on the longest baselines.

Figure 6.3 show the three position-velocity (PV) diagrams of both H^{13}CN and HCN. The PV-diagrams show the emission contours along one spatial axis and a range in velocities. The three panels of Fig. 6.3 correspond to PV-diagrams along slices of different position angles. If a rotation axis is present, the PV-diagram along this axis should show no sign of rotation, whereas the PV-diagram along the perpendicular axis should. The three axes for which we show PV-diagrams are chosen so that one coincides with the direction of the velocity gradient seen in Fig. 6.1 (the same direction as the north-south outflow), one which is perpendicular to the previous one (coinciding with the east-west outflow), and one which is
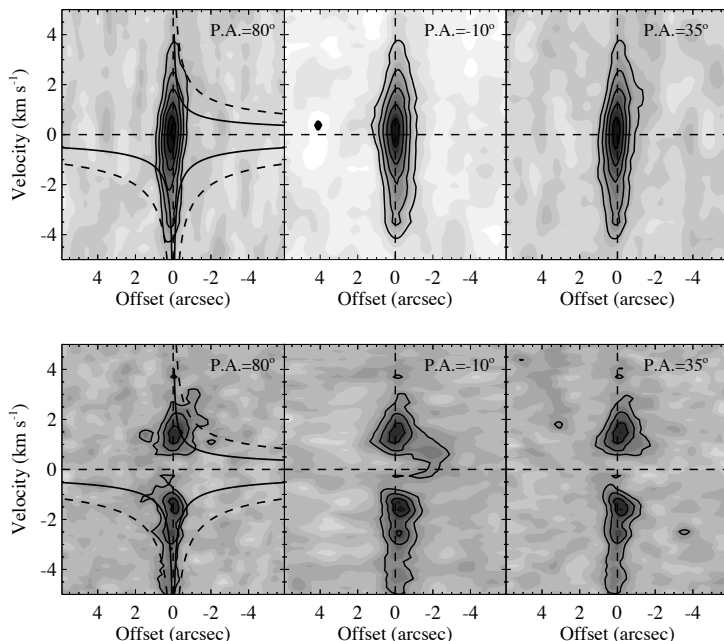
Figure 6.3: PV-diagrams of the combined SMA data sets of H^{13}CN J =4–3 and HCN J =4–3. The three panels correspond to slices along different position angle with PA=80° being the direction of the north-south outflow, PA=-10° the direction of the east-west outflow, and PA=35° the direction which lines up IRAS2B and IRAS2C. The PV-diagrams show little difference with changing position angle suggesting no preferred axis of rotation. In the leftmost panels are shown Keplerian rotation (top quadrants) and free-fall (bottom quadrants) profiles for M_*=0.3 M$_\odot$ (full line) and 1.0 M$_\odot$ (dashed line).

inclined with 45° with respect to the other two axis (coinciding with the direction toward IRAS2B and IRAS2C).

The first thing to notice is that the three panels are not very different from each other. There is no obvious rotation axis and with both peak intensities located exactly at zero off-set in all three panels, there is actually very little sign of the velocity gradient at all, except for small skew in the contours in the left-most panel of H^{13}CN and a bit of 3-6 σ emission at positive velocities in the center HCN panel. The black lines that are also plotted in Fig. 6.3 show Keplerian rotation profiles for a central mass of 0.3 M$_\odot$ (full line) and 1.0 M$_\odot$ (dashed line) in the first

quadrant. The curves in the two lower quadrants show free-fall velocity profiles for the corresponding central masses. Obviously, it is not possible to discriminate between rotation and infall by comparing the emission to these curves, because the emission is very compact, even for HCN. The emission contours are, however, more consistent with the 0.3 $M_{\odot}$ curves than with the 1.0 $M_{\odot}$ curves. The second thing to notice in the PV-diagrams is how fast the emission drops off along the spatial axis while the emission at small off-sets shows very broad lines. This is true for both HCN and H^{13}CN. It is therefore likely that the velocity gradient which is seen in the moment maps is due to the outflow rather than rotation. After all, this gradient does lie in the same direction as the outflow. These PV-diagrams also resemble the ones presented by Hogerheijde et al. (1998) for a number of known outflow sources.

6.4   Analysis

We describe the observed emission with the model for the density and temperature from Jørgensen et al. (2002), who derived this model from analysis of the continuum image of the source at 450 μm and 850 μm as well as at its broadband SED from 60 μm to 1.3 mm. The density is described by a power-law,

$$n(r) = 1.5 \times 10^6 \text{ cm}^{-3} (r/1000 \text{ AU})^{-1.8}, \tag{6.1}$$

while the temperature was calculated using a 1D continuum radiation transfer code as described by Jørgensen et al. (2002, see also Fig. 1f of Jørgensen et al. 2004a). The outer radius of the model is 1.2×10^4 AU. Jørgensen et al. (2004b) also modeled the chemical abundance profiles using the integrated intensity of the optically thin H^{13}CN single-dish lines. They found that to reproduce the line ratios, a model with a depletion zone is needed. The resulting HCN abundance profile reads,

$$X(\text{HCN}) = \left\{ \begin{array}{ll} 2 \times 10^{-8} & , n_{\text{H}_2} < 7 \times 10^4 \text{ cm}^{-3} \\ 2 \times 10^{-9} & , n_{\text{H}_2} > 7 \times 10^4 \text{ cm}^{-3} \end{array} \right. , \tag{6.2}$$

assuming an isotopic abundance ratio of ^{12}C/^{13}C = 70. We furthermore add a central compact component, in accordance to Jørgensen et al. (2005a) who found a need for an abundance increase near the center. We describe this component with a jump in the abundance within the radius above 90 K (~100 AU) to $X(\text{HCN}) = 7 \times 10^{-8}$.

The new addition to the model is a parameterization of the velocity field, which allows for both infall and rotation. This breaks the spherical symmetry

of the model, making it two-dimensional, although we keep the spherical description of the density and temperature. We follow the approach presented in Chapter 3 with a velocity field parameterized by two parameters,

$$\mathbf{v} = \begin{pmatrix} v_r \\ v_\phi \end{pmatrix} = \sqrt{\frac{GM_*}{r}} \begin{pmatrix} -\sqrt{2}\sin\alpha \\ \cos\alpha \end{pmatrix}, \tag{6.3}$$

with M_*, the mass of the central object, and the angle α as free parameter. The velocity parameterization is such that $\alpha = 0$ corresponds to Keplerian rotation and no infall, whereas $\alpha = \pi/2$ corresponds to free fall toward the center and no rotation. The use of this two-dimensional velocity field further introduces two free parameters, namely the inclination of the rotation axis with respect to the plane of the sky and the position angle of the rotation axis in the plane of the sky. We add a mean turbulent velocity field of 0.2 km s^{-1} to the model. While this parameter is somewhat degenerate with the central mass in the sense that it affects the line widths, it cannot account for the different line widths at different resolution. Only by letting the turbulent field vary across the model could we reproduce this effect. We have however chosen to use a constant turbulent field to keep the model simple, and a small change in its value does not affect our result significantly. For an in-depth discussion of turbulent line broadening we refer the reader to, e.g., Ward-Thompson & Buckley (2001).

We use the molecular excitation and radiation transfer code *RATRAN* (Hogerheijde & van der Tak 2000) to determine the level populations of the HCN molecule on a computational domain consisting of multiple nested regular grids. The grid resolves scales from 6 AU to 1.2×10^4 AU, which is about the highest dynamical range of scales we can resolve with *RATRAN* without loosing the gain of the accelerated lambda iteration (ALI) algorithm which makes the code feasible to run on a standard desktop computer. The resulting image cubes are afterward either convolved with the appropriate beam profiles for comparison to the single-dish lines or Fourier transformed for direct comparison to the visibility tables in the BIMA and SMA data sets.

6.4.1 Model fit

We run a grid of models in the parameter ranges $M_* \in \{0.0, 1.0\}$ and $\alpha \in \{0, \pi/2\}$ and we compare the single-dish spectra and PV-diagrams from the SMA data of H^{13}CN only. A χ^2-surface plot is shown in Fig. 6.4 for an inclination of 40°. We add the χ^2 value of the two single-dish transitions, calculated channel by channel on a velocity range from -4 to +4 km s^{-1}, to the χ^2 value of the PV-diagram, where
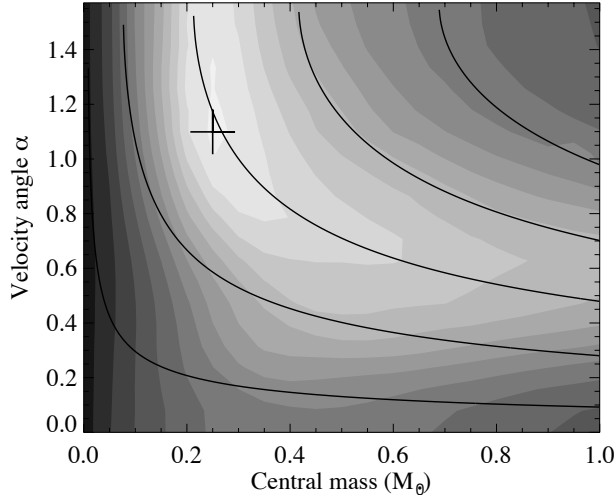
Figure 6.4: H^{13}CN χ^2 surface in the parameters M_* and α. The cross marks the minimum which lies at M_*=0.25 M$_\odot$ and α=1.10 with a χ^2 value of 3.71. The black lines are lines of constant accretion rate, with lines corresponding to 1, 3, 5, 7, and 9 $\times10^{-5}$ M$_\odot$ yr^{-1} going from the lowest line and up.

we compare pixels with a signal-to-noise better than three only. The χ^2 is seen to be minimized for parameter values of $M_* = 0.25$ M$_\odot$ and $\alpha = 1.10$, which we take to be our best fit model. We have chosen to adopt an inclination parameter value of 40°, because this parameter is not well-constrained by our fit. For any value below 40$^c irc$, we get an almost constant χ^2 value and only for values higher than 40° we see a systematic increase in the χ^2. The reason is that our best fit already favors an infall dominated model (i.e., almost spherical velocity field) and therefore the velocity field is mostly independent of the inclination. As we go toward models with more rotation, the fit rapidly deteriorates with increasing inclination, which only support the result that little rotation is present in IRAS2A. Similarly, the position angle is unconstrained for the same reasons, in full agreement with the PV-diagrams shown in Sect. 6.3. We have also plotted lines of constant mass accretion rate in Fig. 6.4. The accretion rate is calculated as

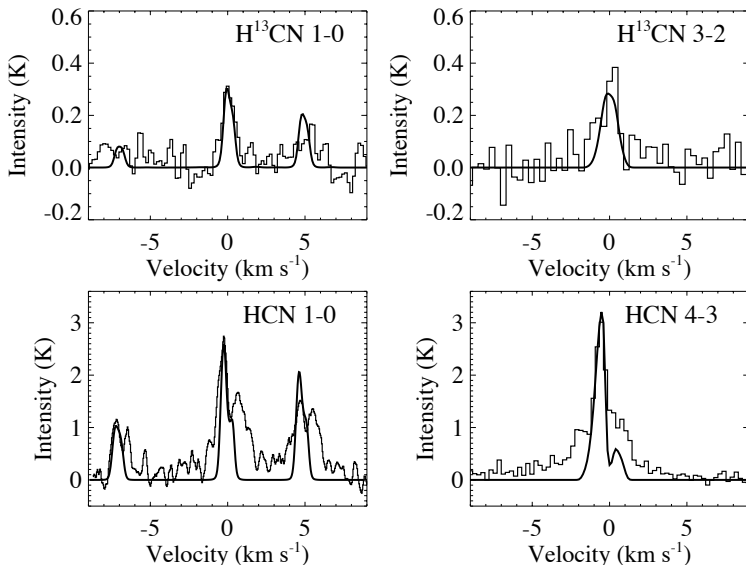$$\dot{M} = 4\pi r_0^2 \rho_0 \sqrt{\frac{2GM_*}{r_0}} \sin(\alpha) \tag{6.4}$$

135

Figure 6.5: Best model fit to the four single-dish transitions of HCN and H^{13}CN.

where ρ_0 is the mass density at the distance r_0. Our fit is seen to be consistent with a mass accretion rate of 5×10^{-5} M$_\odot$ yr^{-1}.

The first fit, shown in Fig. 6.5, is that of the single-dish lines H^{13}CN J =1–0, 3–2 and HCN J =1–0, 4–3. Being optically thin, the H^{13}CN lines are quite sensitive to the abundance profile and they constrain the radial variations well, as discussed by Jørgensen et al. (2005a). The single-dish lines fit well, and our best fit model automatically reproduces the (u, v)-amplitudes as well (Fig. 6.2, panel a). The J =1–0 lines show distinct hyperfine components. We model these components under the assumtion of LTE between the hyperfine levels. The hyperfine line ratios are also well reproduced. The HCN lines have a much more distinct profile and they are much more sensitive to the velocity parameters. However, the large optical thickness of HCN and the possible contamination of outflow emission in these lines make it difficult to assess the quality of our model (not the fit) on basis of these lines. This is the reason why we do not include the HCN lines in our χ^2 analysis. That said, our overall best fit model is also the model which gives the best fit to the HCN single-dish lines alone and it reproduces the (u, v)-amplitudes nicely. The fits to all four single-dish lines are shown in Fig. 6.5. Only the primary component of the H^{13}CN J=1–0 line is considered when calculating
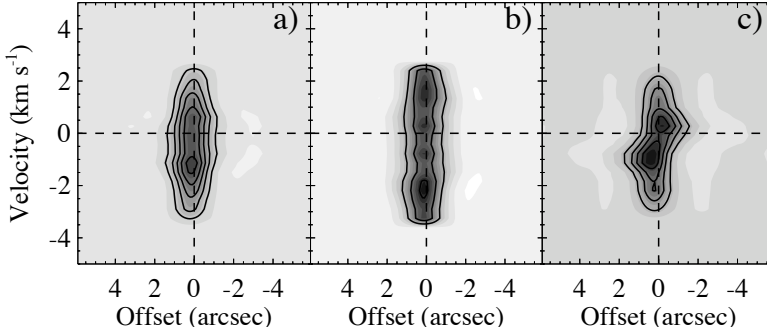
Figure 6.6: Model PV-diagrams of $H^{13}CN$ $J = 4$–3 at P.A=10°. **a)** Best fit model. **b)** High central mass model with M_*=1.0 $M_\odot$ and α=1.1. **c)** Strongly rotating model with M_*=0.25 and α=0.2. All three panels are directly comparable to the center top panel of Fig. 6.3.

the χ^2. However, our best fit model produces a reasonable fit to the hyperfine components, also for the HCN line.

Figure 6.6 shows the best fit $H^{13}CN$ model PV-diagram (panel a) as well as two other models for comparison, M_*=1.0 $M_\odot$ and α=1.1 (panel b) and M_*=0.25 $M_\odot$ and α=0.2 (panel c). The contour levels in these plots are set to the same values as the levels in Fig. 6.3 and so these plots are directly comparable to the center panel (PA=-10°) of that figure. The best fit model is seen to reproduce the features of the data well in terms of line intensities and emission distribution, while the model in panel b has too weak lines and the model in panel c shows a skewed emission distribution. The asymmetry seen in panel c is typical for a rotating velocity field and this feature is not seen at all in the data. Our best fit model also predicts the HCN $J = 4$–3 line and this is shown in Fig. 6.7, panel a. Panel b of this figure shows the residual when the model is subtracted from the data (center bottom panel of Fig. 6.3). A strong red-blue infall asymmetry is seen in the model spectra, with the blue peak very much overproduced and a lot of high (negative) velocity material not reproduced by our model. A likely explanation for the overproduction of the HCN emission is that our temperature model is slightly off. Another possibility is that the isotopic abundance ratio is lower than the canonical $^{12}C/^{13}C$ ratio of 70 by 20–30%.
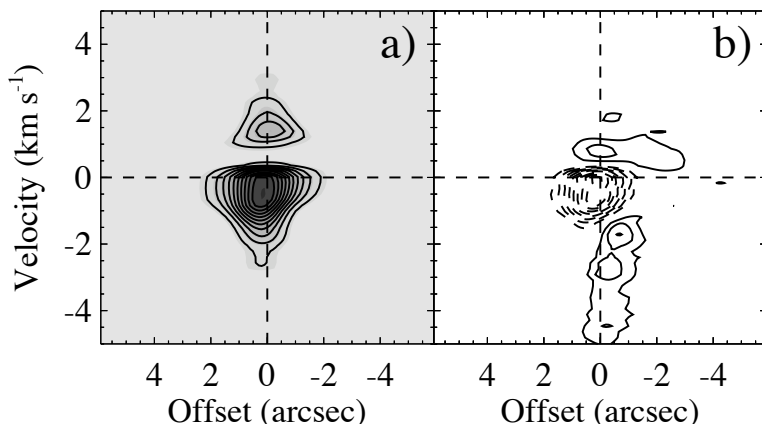
Figure 6.7: Fit to the SMA data of the HCN $J = 4$–3 line. **a)** shows our best fit model while **b)** shows the residual of the fit. Contour levels are the same as in Fig. 6.3.

6.4.2 Outflow

IRAS2A is known to drive two strong outflows, along axes that are almost perpendicular to each other. We do not model these outflows, and therefore we do not expect to reproduce features in the data that are associated with the outflows. As an optically thin line, we expect that $H^{13}CN$ is much less affected than HCN, and indeed only the single-dish HCN lines show broad wings with excess emission not accounted for by our model. Both the single-dish and the SMA HCN spectra are contaminated by outflow emission, and if we go to the BIMA observations of the low excitation line $J = 1$–0, it immediately becomes clear that care needs to be taken when modeling the HCN lines. Figure 6.8 shows the BIMA spectrum toward the center of the source. Two models are overplotted, the best fit with a solid line and a model with $M_* = 1.0$ $M_\odot$ using a dashed line style. The observed spectrum is extremely broad with wings extending all the way to ± 6 km s^{-1}. Our model does not reproduce these velocities, and indeed, even if we increase the mass significantly, the line width only increases a little.
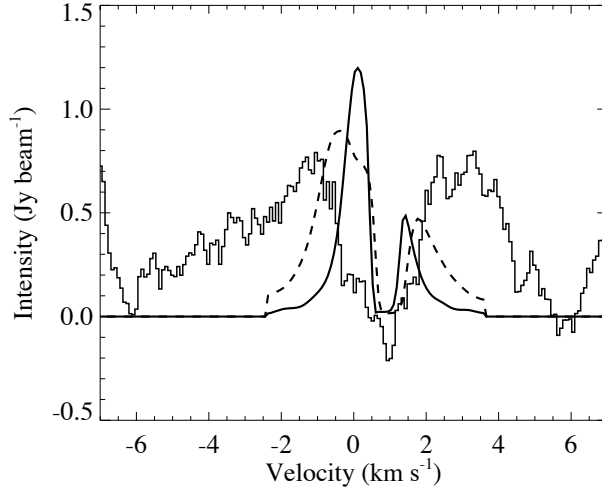
Figure 6.8: A HCN $J = 1$–0 spectrum toward the center of IRAS2A as observed by BIMA. Two models are overplotted; our best fit model in solid line style and a model with $M_* = 1.0$ M$_\odot$ in dashed line style. The truncation of the model line wings at 2.5 km s^{-1} is due to the finite pixel size of our grid.

6.5 Discussion

We determine the central mass of IRAS2A to be 0.25 M$_\odot$ with an uncertainty of ± 0.1 M$_\odot$. This value is considerably smaller than the mass of the envelope of 1.7 M$_\odot$ which is obtained by integrating Eq. 6.1. This makes IRAS2A a true Class 0 object as it falls in the definition of Class 0 where $M_* < M_{\mathrm{env}}$. Figure 6.4 shows that our best fit is consistent with a mass accretion rate of 5×10^{-5} M$_\odot$ yr^{-1}. This is a high rate and if the mass accretion rate has been constant, the current central mass would have been accreted in only 5×10^3 yr. However, the accretion rate has probably not been this high in the past or maybe most of the material does not accrete directly onto the star. IRAS2A has a bolometric luminosity estimated to be 20–25 L$_\odot$ and if we assume that this luminosity entirely originates from the accretion through the relation $L = GM_* \dot{M}/r$, the material needs to accrete at a radius of approximately 16–20 solar radii (0.07–0.09 AU), which is about a factor of 6–8 bigger than the estimated stellar radius of young protostars (Stahler 1988) and within the anticipated radius of a disk. From the earlier study of the SMA measurements of the continuum emission, we know that

a compact 0.1 M$_\odot$ component must be present, and this component must also have been built up by the accretion flow within the lifetime of the object. The fact that the material seems to accrete on very small radii suggests that this component is very small and this may explain why we do not see any rotation associated with this component in the data. But does it even make sense to interpret this component as a circumstellar disk given that its mass is almost equal to the stellar mass? One possible explanation of the absence of these velocities is that the disk lies exactly in the plane of the sky and we are viewing it face-on. This however, does not agree with the two outflows which both have components in the plane of the sky and makes it difficult to imagine how a face-on disk would be possible. Another possibility is that the compact component is not really a stable disk (yet?) but rather a pile up of low-angular momentum material very close to the star, which is still dominated by infall. Indeed, Chiang et al. (2008) showed that their high-resolution continuum observations of IRAS2A can be well described without a disk component, when using a magneto-dynamical envelope model rather than a power-law type model like the one used in this work. In any case, it is hard to imagine how a star of 0.25 M$_\odot$ can support such a relatively massive disk in stable rotation. Maybe this material represents the very earliest stages of disk formation? If this is true, given the almost equal mass of star and disk, it implies that the disk begins to form almost simultaneous with the star. It can be argued that it takes of the order of one rotation period to achieve stable rotation (Myers, *priv. comm.*). The rotation period at a radius of the SMA beam (0.5″=110 AU) is 2.3×10^3 yr. This is a lower limit because the central mass has most likely been lower in the past, and is comparable to the age derived above. The material may not have made a full rotation and spread out to form a Keplerian disk yet. Using this argument, Keplerian rotation should be detected in a 0.05″ beam, if the compact density component indeed represents a disk.

We conclude that IRAS2A is an example of a very young protostar based on our best fit velocity model, with both parameters pointing toward a young source. Its velocity field is characterized by a high degree of infall relative to rotation, which in comparison to the study of the velocity field in hydrodynamical simulations of star formation, that was discussed in chapter 3, suggests a young source. In that chapter it was shown that the α parameter evolves smoothly with time from a high value ($\pi/2$) to a low value (0.0) as a core collapses and a disk is formed. A study similar to this one was done in chapter 2 for another young star, L1489 IRS, classified as a Class I source. For this source, a disk was detected based on similar kinematical arguments as we use here, and for that source an α value of 0.26 was found. Based on the value of the α parameter alone, we

conclude that IRAS2A is a younger source than L1489 IRS, and this is entirely consistent with the general perception that Class 0 objects are younger than Class I objects.

6.6   Summary and outlook

In this chapter we have modeled the velocity field of the Class 0 young stellar object NGC1333–IRAS2A. We have constrained our model primarily by the PV-diagram of the H^{13}CN emission observed in very high resolution with the SMA. Despite our high resolution and good signal-to-noise ratio we find no evidence for any rotational motions on any scales, even though a very dense, compact component, interpreted as a disk, is needed on scales of < 100 AU to reproduce the (u, v)-amplitudes, seen in the continuum data.

Repeating this approach for a sample of protostars would allow statistical comparison of the velocity fields of these stars and maybe allow a new evolutionary classification based on α and M_*/M_{env}. This will only be possible when the Atacama Large Millimeter Array (ALMA) comes online, because ALMA will be able to do observations like the ones presented here in snapshot mode as opposed to a full night per source needed by the SMA. Furthermore, ALMA will allow us to zoom in on the very centermost parts of protostellar objects and tell us what happens to the velocity field as circumstellar disks form.

In this chapter we did not model the outflow emission that is clearly seen in the BIMA HCN J=1–0 line and also noticeable in the HCN single-dish lines. By using the SMA to observe high-excitation lines, we filter out a lot of the emission on large scale where we expect the outflow to be dominating the velocity field. Still, we do not fit the HCN J=4–3 line very well. This illustrates the need of good radiation transfer outflow models which can be used to investigate the interaction between accretion and outflows on very small scales.

References

Adams, F. C., Shu, F. H., & Lada, C. J. 1988, ApJ, 326, 865

André, P., Ward-Thompson, D., & Barsony, M. 1993, ApJ, 406, 122

Basu, S. 1998, ApJ, 509, 229

Cassen, P. & Moosman, A. 1981, Icarus, 48, 353

Cernis, K. 1990, Ap&SS, 166, 315

Chiang, H.-F., Looney, L. W., Tassis, K., Mundy, L. G., & Mouschovias, T. C. 2008, ApJ, 680, 474

Goodman, A. A., Benson, P. J., Fuller, G. A., & Myers, P. C. 1993, ApJ, 406, 528

Gutermuth, R. A., Myers, P. C., Megeath, S. T., et al. 2008, ApJ, 674, 336

Hogerheijde, M. R. & van der Tak, F. F. S. 2000, A&A, 362, 697

Hogerheijde, M. R., van Dishoeck, E. F., Blake, G. A., & van Langevelde, H. J. 1998, ApJ, 502, 315

Jennings, R. E., Cameron, D. H. M., Cudlip, W., & Hirst, C. J. 1987, MNRAS, 226, 461

Jørgensen, J. K., Bourke, T. L., Myers, P. C., et al. 2007a, ApJ, 659, 479

Jørgensen, J. K., Bourke, T. L., Myers, P. C., et al. 2005a, ApJ, 632, 973

Jørgensen, J. K., Hogerheijde, M. R., van Dishoeck, E. F., Blake, G. A., & Schöier, F. L. 2004a, A&A, 413, 993

Jørgensen, J. K., Johnstone, D., Kirk, H., & Myers, P. C. 2007b, ApJ, 656, 293

Jørgensen, J. K., Schöier, F. L., & van Dishoeck, E. F. 2002, A&A, 389, 908

Jørgensen, J. K., Schöier, F. L., & van Dishoeck, E. F. 2004b, A&A, 416, 603

Jørgensen, J. K., Schöier, F. L., & van Dishoeck, E. F. 2005b, A&A, 435, 177

Lada, C. J. & Wilking, B. A. 1984, ApJ, 287, 610

Looney, L. W., Mundy, L. G., & Welch, W. J. 2000, ApJ, 529, 477

Looney, L. W., Mundy, L. G., & Welch, W. J. 2003, ApJ, 592, 255

Qi, C. 2006, The MIR Cookbook, The Submillimeter Array/Harvard-Smithsonian Center for Astrophysics

Sault, R. J., Teuben, P. J., & Wright, M. C. H. 1995, Astronomical Data Analysis Software and Systems IV, 77, 433

Shu, F. H. 1977, ApJ, 214, 488

Stahler, S. W. 1988, ApJ, 332, 804

Terebey, S., Shu, F. H., & Cassen, P. 1984, ApJ, 286, 529

Ward-Thompson, D. & Buckley, H. D. 2001, MNRAS, 327, 955

Chapter 7

Advances in line radiation transfer modeling

7.1   Introduction

When interpreting astronomical emission line data originating from molecules that are not in thermodynamical equilibrium, it is essential for understanding the source to be able to successfully model the signal. In order to do so, the equations of radiation transport and the molecular excitation need to be solved. There are no general solutions to this problem, and therefore computational expensive numerical methods must be applied. Throughout this thesis, our main modeling tool has been the radiation transfer code *RATRAN* (Hogerheijde & van der Tak 2000), which we have used to simulate the radiation field in protostellar envelopes and disks. As a two-dimensional axis-symmetric code, *RATRAN* was originally developed to model envelopes with rotation and gaseous protoplanetary disks. At the time when *RATRAN* was written, the computers could converge on a solution to a relatively coarse model in hours. With present day computers, the same model converges in a matter of minutes. Hence, the level of detail in these models has increased accordingly. During the same period, observations of far higher resolution have become available, in particular with the first light of the Submillimeter Array in late 2003. In order to follow this advancement, our models are now reaching a level of complexity where CPU time is not the main bottle neck, but rather the basic design of the code itself. In this thesis we have encountered these limitation in Chapters 4 and 6.

There are three main short-comings of the current code: (i) It assumes cylindrical symmetry, effectively confining all structure to two dimensions. This became a problem in Chapter 4 where we found the need for two different rotation axes. (ii) Convergence becomes rapidly slower as the grid resolution is increased which severely limits the effective range of scales of the models. In Chapter 6 we had the need for a model with a radius of 12000 AU, resolved down to scales of

10 AU. This is a huge dynamic range of scales, which in Chapter 6 resulted in a very large number of grid cells and consequently a very slow convergence. (iii) Even with a low number of grid cells, molecules with a large number of transitions converge very slowly. In this thesis we have not dealt with computationally complex molecules, and therefore this has not been a serious issue here. The points (i) and (ii) are of course related in the sense that gridding in three dimensions requires n times more cells (where n is the average number of resolution elements per spatial direction) than the corresponding two-dimensional grid and since it follows trivially that more cells require more CPU time, point (ii) makes three-dimensional grids unfeasible. However, the loss of performance with increasing cell number is more severe than what this effect suggest for codes which use Accelerated Lambda Iteration (such as *RATRAN*). Above a certain number of grid cells, the acceleration is lost and thus convergence takes many more iterations than otherwise.

The third point becomes a problem because for molecules with a large number of transitions, e.g. H_2O, the Monte Carlo approach becomes ineffective even for a small number of cells and therefore high resolution grids are not feasible for these species. However, molecules with many possible transitions are typical very far from LTE and it is desirable not to have gradients in excitation conditions that are too large over the cells which calls for a finer grid (depending on the model). If we furthermore have depletion in certain regions, like the abundance distribution that we showed in Chapter 5, very strong density gradients are present in the model, which calls for higher grid resolution in the boundary regions. Finer grids means more cells and therefore the level population of these molecules are extremely hard to calculate using codes like *RATRAN*.

In this chapter we present a new code which improves on all of these three points. The code is based on *RATRAN*, but a whole new photon propagation algorithm and gridding method is implemented making the code significantly different from *RATRAN*. The code is highly optimized for speed and the user interface is completely reworked for a very flexible model setup.

7.2 Solution method

7.2.1 The molecular level population equilibrium

The problem of radiation transport is described by the equation,

$$\frac{dI_\nu}{ds} = -\alpha_\nu I_\nu + j_\nu. \tag{7.1}$$

For line radiation transfer, the emission and absorption coefficients j_ν and α_ν are determined from the Einstein coefficients, for transition between any two adjacent energy levels E_2 and E_1, through the relations,

$$j_{21} = \frac{\hbar\nu}{2}n_2A_{21}\phi(\nu),\tag{7.2}$$

$$\alpha_{21} = \frac{\hbar\nu}{2}\left(n_1B_{12} - n_2B_{21}\right)\phi(\nu),\tag{7.3}$$

where $h\nu = E_2 - E_1$. The frequency dependent velocity profile function ϕ is given by a Gaussian with a width determined by the local microturbulence.

Solving Eq. 7.1 for the intensity I_ν gives the local mean radiation field through an integral over all solid angles,

$$J_\nu = \frac{1}{4\pi}\int I_\nu d\Omega,\tag{7.4}$$

whereas the population of the l'th level n_l is given by,

$$n_l = \frac{\Sigma_{k>l}n_kA_{kl} + \Sigma_{k\neq l}n_k(B_{kl}J_\nu + C_{kl})}{\Sigma_{k<l}A_{lk} + \Sigma_{k\neq l}(B_{lk}J_\nu + C_{lk})},\tag{7.5}$$

in which we have included the molecule dependent collision rates C_{lk}. The level populations depends on J_ν which again depends on the level populations through j_ν and κ_ν, and thus a solution is obtained by iteratively solving Eq. 7.4 and 7.5 until an equilibrium between the radiation field and the level populations is reached.

7.2.2 Photon transport

In *RATRAN* and similar codes (e.g., *URANIA*, Pavlyuchenkov & Shustov 2004), the source model is laid out onto a grid of rectangular cells. Model properties such as density, temperature, molecular abundance, as well as the radiation field J_ν and the level populations n_i are taken to be constant over each cell. Photon packages are traced backwards in random directions from random points of absorption within a cell and Eq. 7.1 is integrated along the paths. Summing over all photons, the mean radiation field J_ν is obtained for the cell.

In our implementation, the source model is no longer mapped onto a regular grid of cells. Instead we use a set of points which represents the local environment (density, temperature, populations, etc.). The points are distributed in three-dimensional space rather than in a two-dimensional slice, and thus we are able to use three-dimensional source models whereas in *RATRAN*, even though

photons propagate in three-dimensional space, the source model needs to be rotational symmetric around the second axis and mirror symmetric around the first axis. Our points are placed at random throughout the entire computational domain, however with a probability that is weighed by a source model dependent function. In particular we adopt the approach of Ritzerveld & Icke (2006) which is briefly described in the following.

The Poisson point process gives the probability of finding k points within a subset V of the domain S of our source model,

$$P(k) = \frac{(\lambda|V|)^k e^{-\lambda|V|}}{k!}, \quad k = 0, 1, 2, \dots \tag{7.6}$$

λ is called the point intensity and can in general be a function defined on S. It is desirable to obtain a point distribution for which the gradient of the level populations between any two neighboring points becomes as small as possible. This is assured if the mean distance between neighboring points is inversely proportional to the local opacity which is true if $\lambda = c\, n^d$, where n is the density and d is the dimensionality of the source model, in our case 3. The proportionality factor c is a global constant, determined by the total number of points used to describe the source model.

The source model is randomly Nyquist sampled, using Eq. 7.6 to determine the local point density, in order to make sure that all relevant scales of the source model is appropriately described by the point distribution. Besides using this resulting set of points as basis for our computational grid, the obvious advantage of not having to construct a grid by hand, is that points can be added (or removed) dynamically by changing c and resample the source model. Figure 7.1 shows that the neighbor distance is proportional to the density over four orders of magnitude. The (arbitrary) offset between the density graph and the histogram scales with the total number of grid points.

The points are connected by Delaunay triangulation, using the public available *QHull* library (Barber et al. 1996). The transport itself goes along Delaunay lines only from one point to another, which makes integration of Eq. 7.1 particularly simple and very fast. In the three-dimensional Delaunay triangulation, the expectation value for the number of lines attached to a grid point is approximately 16 (Ritzerveld & Icke 2006) and the spatial sampling of J_ν is thus limited to this number of directions.

Figure 7.2 shows an example of a Delaunay grid based on a simple disk model. The grid shown here is the two-dimensional equivalent to the three-dimensional Delaunay grid used in our code. The point distribution is seen to follow the density contours closely and above the disk where density approaches zero, there are no
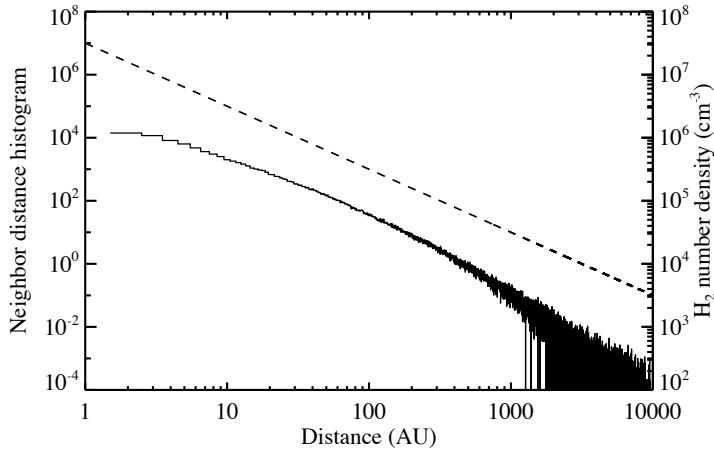
Figure 7.1: A histogram showing the distribution of neighbor distances from 1 AU to 10000 AU. This distribution scales very well with the number density, shown with a dashed line. To make this plot, the density model was sampled by 20000 points.

points. However, we still need to trace a number of photons along each Delaunay line, since we cannot conserve momentum stringently on this grid. In principle, a photon passing a grid point from a certain direction should continue to travel in the exact same direction. This is in general not possible due to the random orientation of the Delaunay lines, so instead we choose one of the two Delaunay lines that make the smallest angle with the incoming line. The outgoing line is picked at random, but weighed by the ratio of the two angles. The same procedure is used at all subsequent grid points (using the original momentum vector to determine the outgoing direction) until the photons escape the cloud. By sending a number of photons along each initial Delaunay line, we thus probe, not a single line of sight, but rather a cone, while still conserving momentum on average. The transport method is illustrated in Fig. 7.3 where the thickness of the connecting Delaunay lines are proportional to the probability of a photon traveling along that line if emitted in the direction indicated by the dashed line.

During gridding of our source model, we also distribute a number of points randomly on the surface of a sphere surrounding our model. These points are also Delaunay triangulated and connected to the grid points, but they do not represent
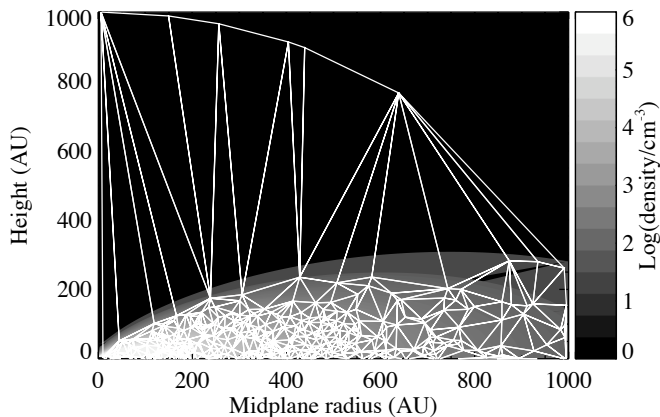
Figure 7.2: An example of the gridding used in our code. The underlying source model is a standard flat disk model and the grid consists of 200 points. For visualization purposes we show here a 2D version of the grid.

anything except the surface of our computational domain. Whenever a photon reaches one of these sink points, it is considered to have escaped the model and we add the CMB contribution before going on to trace the next photon.

Because of the relative low number of photons needed to probe the spatial directions, we can allow ourself to increase the number of photons used to sample the different frequencies, while we still maintain a low (initial) number of photons per grid point. When J_ν has been obtained for a grid point, the level populations are solved for, using the same Λ-iteration method as in *RATRAN* (see Hogerheijde & van der Tak 2000, for details on (Accelerated) Lambda Iteration). Three subsequent iterations of finding J_ν and solving for n_l are done, after which the variance of the three solutions is calculated. If the change in level populations between these iterations is smaller than some preset limit, the grid point is said to be converged. By looping through all grid points until all have converged, and increasing the number of photons in the unconverged points, we end up with a global solution with all grid points converged.
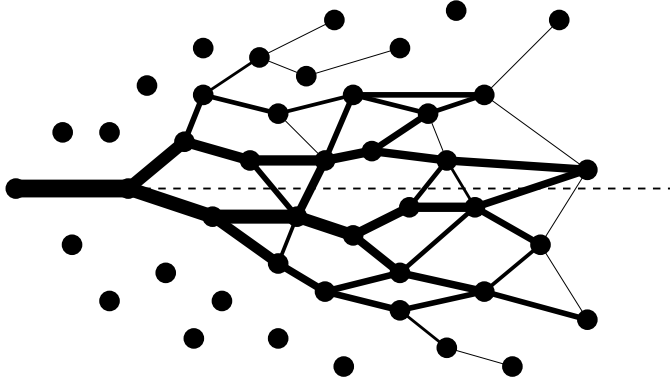
Figure 7.3: Illustration of the photon propagation. When a photon reaches a neighboring grid point, it chooses its new direction with a propability that is proportional to the angle between the new direction and the original direction (dashed line). In this figure, the lines represent possible photon paths and their thickness is proportional to the probability of a photon traveling along that particular Delaunay line. In this figure, the lines disappear below a certain probability threshold. The photons travel from left to right.

7.2.3 Raytracing

After population equilibrium has been reached, we raytrace lines of sight through the model in order to obtain an image cube of the radiation that escapes from the surface. For the raytracing we let the photons move in straight lines, rather than jumping from grid point to grid point. We therefore make use of the Voronoi diagram which corresponds to our Delaunay tessellation. The cells of the Voronoi diagram are connected to the vertex points of the Delaunay tessellation by definition: Given the i'th grid point P_i, the i'th Voronoi cell consists of all points $q \in (x, y, z)$ for which $|P_i - q| < |P_{j \neq i} - q|$ is true. The entire volume of the Voronoi cell is represented by the populations of the corresponding Delaunay point and so integration of Eq. 7.1 becomes a matter of stepping through the source model and figuring out in which Voronoi cell the photon is, which, from an algorithmic point of view, comes down to a simple sorting, not of thousands of cells, but only of, on average, 16 neighboring cells.

This is a very fast process compared to moving through a rectangular grid, but not as fast as moving along the Delaunay lines, which is why this transport method is not used when determining the level populations.

7.2.4 Interface

An important improvement to the code is a redesign of the user interface, for a flexible and very adaptable model input method. In a grid based code, the model needs to be mapped onto the regular grid, and this requires a lot of interpolation, with the added risk of introducing error by, for instance, not strictly conserving mass. Furthermore, since the model may originate from many different sources, e.g., analytical functions for the velocity, tabulated data for the temperature, output from another code for the density etc., several custom schemes need to be employed in order to map a single model onto the grid.

   In our implementation, the model is supplied through a number of subroutines. These subroutines are compiled and linked each time the code is invoked. The user has complete freedom to formulate the model within these subroutines as long as the physical property, e.g., the density, as a function of x, y, and z is returned. The simplest possibility is to give a functional expression, but more elaborate solutions, such as interpolating in a look-up table, are also possible. In principle, a function call to an external program can be given, so that, for example, the temperature could be calculated self-consistently on demand by a separate program. This last option could become interesting for future model work in the sense that it allows the user to link our code directly to another code (typically a hydrodynamical or chemistry code) and run the two simultaneously, sharing their output.

7.3 Performance

One of the main purposes with this code is to improve performance with respect to previously available codes. The aim is to make a code which is faster than *RATRAN*, while still providing consistent results, and which is fully three-dimensional.

   Figure 7.4 shows the performance of our code as well as the one-dimensional and two-dimensional versions of *RATRAN*. The model which is used in this test is a very simple, spherical power-law envelope in free fall

$$n(r) \quad = \quad 1 \times 10^6 \text{ cm}^{-3} (r/1000 \text{ AU})^{-1.5}, \tag{7.7}$$

$$t(r) \quad = \quad 20 \text{ K } (r/1000 \text{ AU})^{-0.4}, \tag{7.8}$$

$$v(r) \quad = \quad -\sqrt{\frac{2G \; 1.0 \text{ M}_\odot}{r}}. \tag{7.9}$$

The test in Fig. 7.4 is for CO which is an computationally "easy" molecule (i.e., it
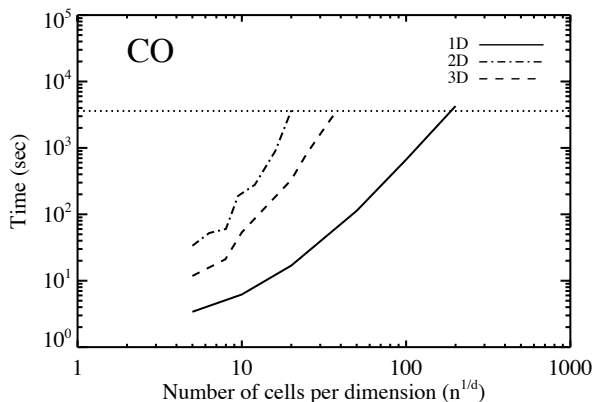
Figure 7.4: The performance of the code described in this paper along with that of 1D and 2D *RATRAN*, for a simple model with increasing grid resolution. The horizontal dotted line marks 1 hour of running time.

has a small number of transitions per level). The figure shows the number of grid cells used to describe the source model per dimension (grid points in the case of our code) versus the time it takes to converge on a solution. All tests shown here have been made on the same standard desktop computer. Our code is seen to be faster than two-dimensional *RATRAN* for the entire range of grid resolutions that was tested. We increased the number of grid cells/points until the model would run for more than 1 hour, marked by the dotted line at 3600 seconds. We cannot compete with the one-dimensional code which is seen to be much faster than both the two-dimensional code and our code.

More interesting is the case of H_2O, which is a notorious "difficult" molecule to calculate because of the many possible and closely spaced transitions between its levels. The result of this benchmark is shown in Fig. 7.5. In this figure it is seen that the convergence takes much longer than for CO for all three codes. Especially the two-dimensional version of *RATRAN* shows a much steeper relation between grid resolution and convergence time. The three-dimensional code also shows slow-down with respect to the CO calculations, but the slope of the relation is much more shallow than for the two-dimensional code, which means that water models of a reasonable resolution can be calculated in minutes with our code, as opposed to hours with the two-dimensional code.

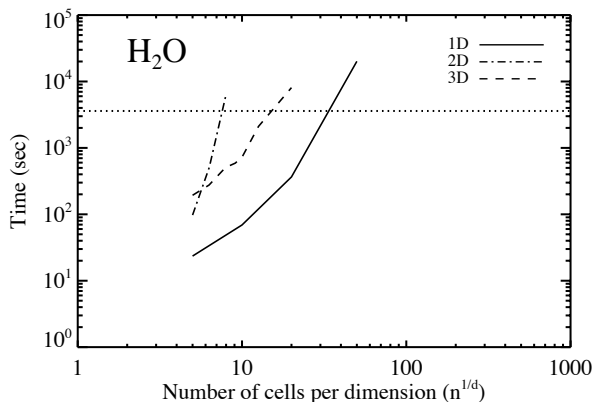It should be noted though that if the source model is intrinsically one-dimen-

Figure 7.5: Similar to Fig. 7.4 but for the water molecule.

sional, it should certainly be calculated with the one-dimensional code rather than by our three-dimensional code. However, if any asymmetries exists in the source model, either in the density distribution or the velocity field, it will be faster to use our code.

7.4 Examples

Here we present three examples that illustrate the capabilities of our code. These examples are not necessarily physical, but are meant as demonstrations of the code. In the following we assume a source distance of 140 pc when we talk about the resolution in the images.

7.4.1 Comparison to *RATRAN*

In this first example we show that our code produces a result which is similar to the solution of *RATRAN* for a model which can also be calculated by a two-dimensional code. We use the same simple setup as in our benchmark tests (Sect. 7.3) to calculate a CO image. In Fig. 7.6 a single spectrum is shown, taken toward the center of the model at three different resolutions as calculated by *RATRAN* and by our code. The resolutions used are 10″, 1″, and 0.1″. In all three cases the spectra are seen to match well, except for the fact that in the unconvolved (pixel resolution) case, the spectra begin to show pixelization. The discrepancy
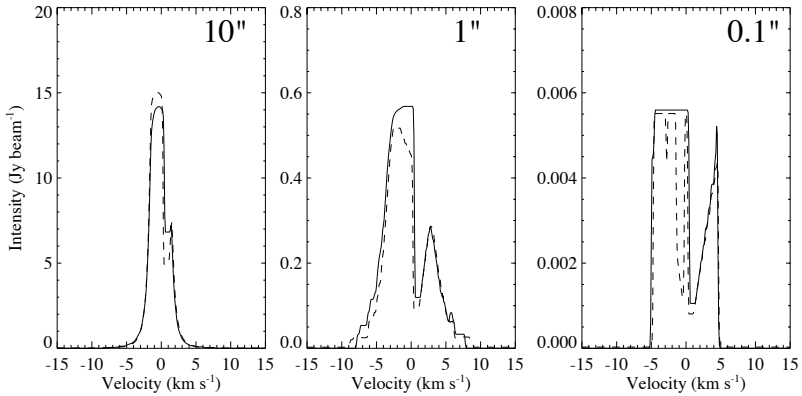
Figure 7.6: CO *J*=1–0 spectra of a simple infalling envelope model. In each panel the corresponding *RATRAN* spectrum is plotted on top of the spectrum made with the code presented in this chapter. The result from our code is shown in dashed linestyle.

which is seen in a few of the channels is mainly due to the difficulties in conserving mass properly when mapping a spherical profile onto a regular grid.

A more robust way to compare the solutions of the two codes is to compare the actual level populations. This is best done by plotting the radial excitation temperature, defined as

$$\frac{n_u}{n_l} = \frac{g_u}{g_l} \exp\left(-\frac{\Delta E}{k_B T_{ex}}\right) \tag{7.10}$$

where n_u and n_l are the upper and lower level populations of two adjacent levels, g_u and g_l the corresponding statistical weights and ΔE the energy difference between the levels. The excitation temperature as a function of radius of the first four transitions of CO is plotted in Fig. 7.7. In this figure we used the one-dimensional version of *RATRAN* for increased resolution, but still the thin curve is seen to be more step-like than the thick line, calculated with our code. Apart from that, the two curves are perfectly similar.
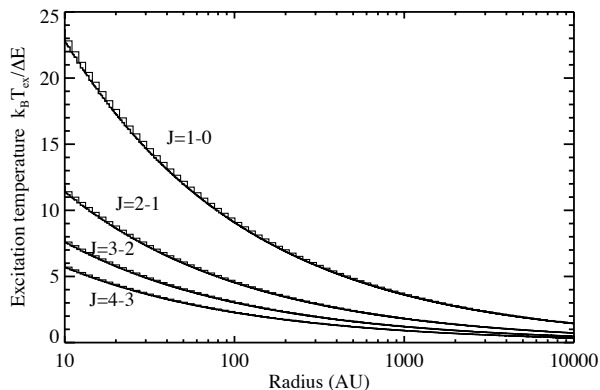
Figure 7.7: The excitation temperature of the first 4 transitions of CO (from the top curve and down). The thick line is the excitation temperature calculated by the code presented here whereas the thin, slightly boxy curve is calculated by the one-dimensional version of *RATRAN*. Apart from the lower resolution of *RATRAN*, the curves are indistinguishable.

7.4.2 Misaligned disk/envelope system

The second example is a model which is intrinsically three dimensional. The model used here is similar to the model of L1489 IRS presented in Chapter 4, where a disk is rotating around a different axis than the rotation axis of the enve-lope. This example demonstrates that such geometries can be distinguished from axi-symmetric models.

The model has two components, a disk and a shell structured envelope. The envelope is rotating and infalling while the disk is in pure Keplerian motion. The rotation axis of the two components is misaligned by 45°. The envelope is de-scribed by a power-law and is spherically symmetric. The H_2 number density is parameterized by

$$n(r) = 10^6 \text{ cm}^{-3} \left(\frac{r}{1000 \text{ AU}} \right)^{-2}, \tag{7.11}$$

with an inner radius of 400 AU and an outer radius of 3000 AU, resulting in a mass of 0.25 $M_\odot$. The temperature is defined similarly,

$$T(r) = 20 \text{ K} \left(\frac{r}{1000 \text{ AU}} \right)^{-0.4}. \tag{7.12}$$

154

This temperature description also applies within the 400 AU radius. Within the radius of 400 AU the density profile is described by a parameterized disk,

$$n(r, \theta) = 2.5 \times 10^{24} \text{ cm}^{-2} \left(\frac{r}{1 \text{ AU}}\right)^{-1} \frac{1}{\sqrt{2\pi}H_0} e^{-\frac{1}{2}\left(\frac{r \cos(\theta)}{H_0}\right)^2}, \qquad (7.13)$$

with a scale height $H_0 = 0.25r$ resulting in a disk mass of 0.01 $M_\odot$. The velocity field is parameterized as

$$v_\phi \cos(\alpha) = -\frac{v_r}{\sqrt{2}} \sin(\alpha) = \sqrt{\frac{GM}{r}}, \qquad (7.14)$$

where M is the central mass for which we use 1 $M_\odot$ and α is set to 0.2 in the envelope and 0.0 in the disk. Tilting the disk with respect to the envelope will result in a discontinuity in the density and velocity fields, but we will assume that the effects of this is negligible. Figure 7.8 shows four different realizations of this model. The left column shows a plot of the density profile cross section with an arrow indicating the axes of rotation. The right column shows the corresponding integrated emission maps as calculated by our code. These maps represent emission of HCO$^+$ J =1–0 and they have been convolved by an 0.7″ Gaussian in order to reproduce the typical submillimeter interferometer resolution.

In the two situations shown in Fig. 7.8 (A and B), the rotation axis of the disk and of the envelope is aligned. In panel B, this axis is inclined by 45° towards the observer. These two situations are axi-symmetric, and can therefore also be reproduced by *RATRAN*. In panels C and D (Fig. 7.8), the rotation axis of the disk is offset from that of the envelope by 45°. In panel C, the system is viewed from the side, whereas in panel D, the disk is inclined towards the observer. These two situations are not reproduceable by two-dimensional codes, since the geometry of this model is intrinsically three-dimensional. The changing disk geometry is clearly observable in the image maps. Each of the models were computed, including raytracing, within an hour on a standard laptop computer, using 10^4 grids points.

7.4.3   Complex structured disks

In the third example we consider a gaseous protoplanetary disk with a density perturbation in the azimuthal direction, in particular, a spiral density wave. This example is constructed specifically to demonstrate the code and the particular setup that we use is very artificial. However, the young stellar object AB Auriga shows sign of a spiral pattern in its disk (Fukagawa et al. 2004, and others). In
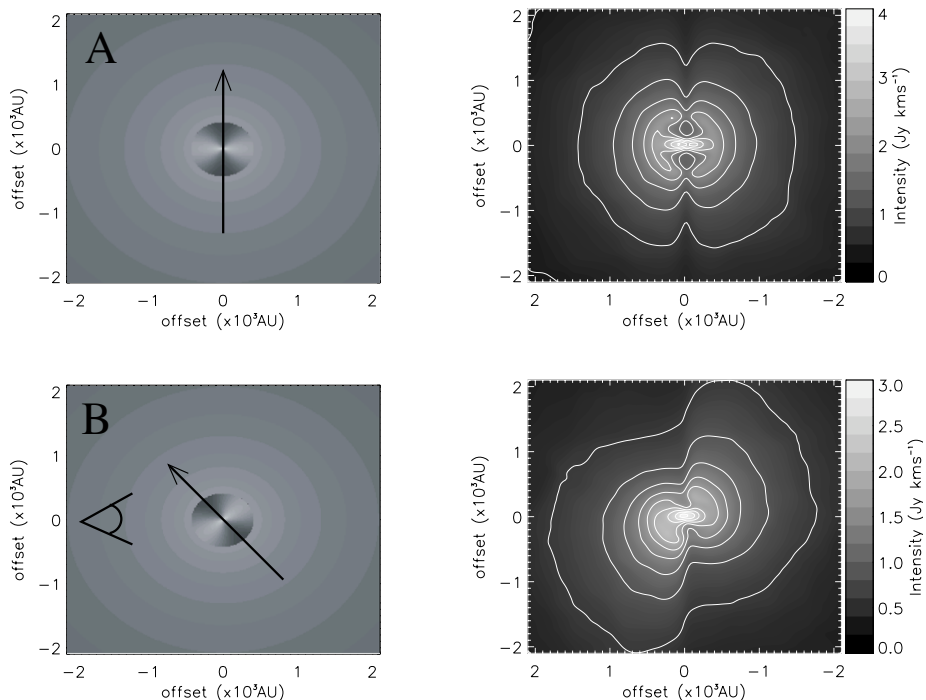
Figure 7.8: The model described in Sect. 7.4.2. The left column shows the density model as well as the rotation axis and viewing angle. The right column shows the intensity distribution of HCO$^+$ J =1–0 line emission as calculated by our code. This figure is continued on the following page.

general, protoplanetary disks are known to have density structure, such as holes and gaps and with the increased resolution of ALMA, it might be possible to image such structure in the future. The radial and vertical structure of the disk used here is similar to the disk described in Eq. 7.13. The velocity field is kept fully Keplerian, with no components in the radial and vertical directions. For the density spiral wave we modify Eq. 7.13, using the analytic description of Cox & Gómez (2002) for a logarithmic spiral with a pitch angle δ,

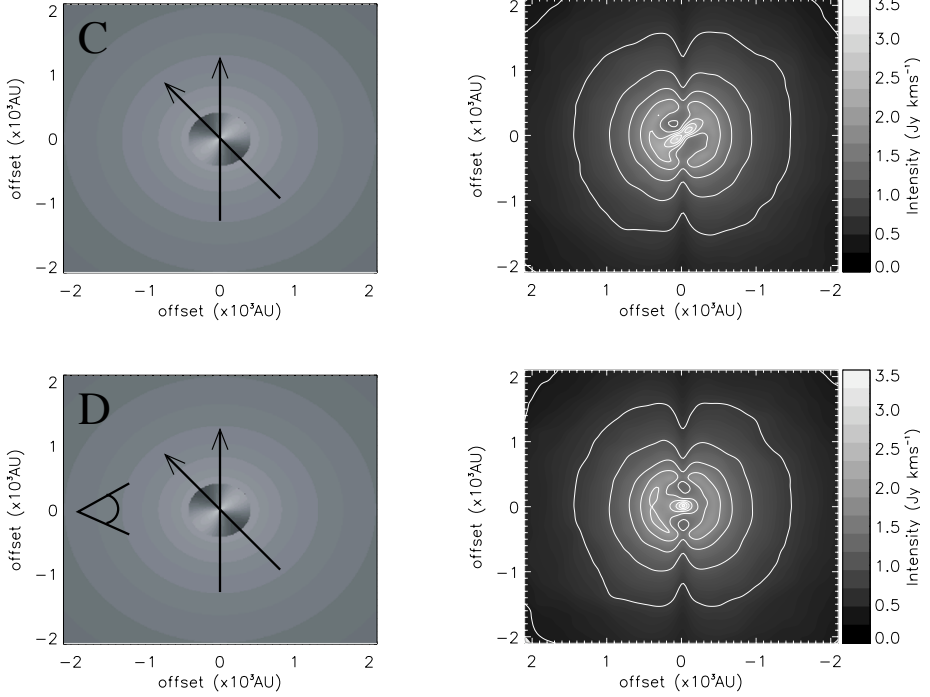$$n(r, \theta, \phi) = n_{disk}(r, \theta)D \cos(\gamma), \tag{7.15}$$

Figure 7.8: Continued from previous page, now for models with different disk and envelope rotation axes.

where

$$\gamma = N\left(\phi - \frac{\ln(r/r_0)}{\tan(\delta)}\right). \tag{7.16}$$

We have chosen a pitch angle $\delta = 0.3$ and the number of spiral arms $N = 2$. The coefficient D is chosen so that the overall disk mass is 0.25 $M_\odot$. In a real science case, a molecular transition with a critical density that falls right in between the peaks of the density perturbation would be needed in order to detect it observationally. Here we have adjusted the density contrast so that the maximum and minimum values for the density wave falls on either side of the critical density for HCO$^+$ J =1–0 in order to make the spiral pattern visible in the figure. The contrast is several orders of magnitude.

Figure 7.9 shows a face-on view of the integrated intensity of this model. The
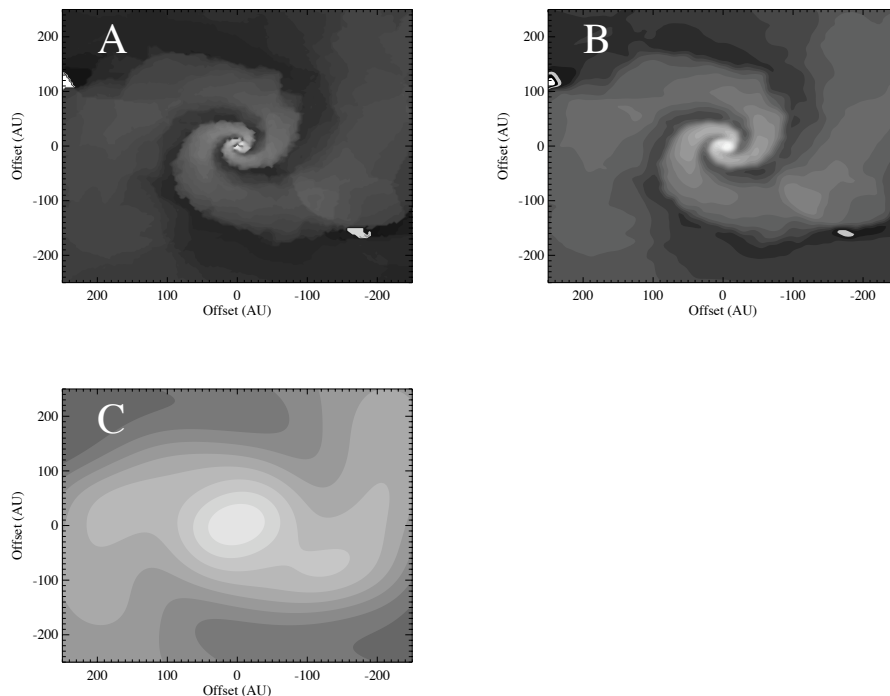
Figure 7.9: The emission signature of a spiral density wave in a face-on disk. The resolution of the three images is **a)** 0.02″, **b)** 0.07″, and **c)** 0.7″.

three panels correspond to three different resolutions, unconvolved (pixel limited, 0.02″), highest ALMA resolution (0.07″) and highest SMA resolution (0.7″).

7.5 Outlook

While the code presented in this chapter is already capable of producing images and spectra which are almost indistinguishable from the corresponding results of *RATRAN*, our code still needs proper testing before it can be applied to real science problems. Some features still needs to be implemented, such as secondary collision partners, separate gas and dust temperatures, proper treatment of lines with hyperfine structure, etc., and additional code optimization needs to be done in order gain full advantage of our method. However, as we have shown in this

chapter, the main code framework is in place and it is working well. With the coming of the Herschel Space Observatory which will observe many H_2O and OH transitions in the far-infrared, and ALMA, which will reach an unprecedented resolution in the submillimeter wavelength regime, codes like the one presented here are certainly going to be needed in order to interpret the observations which these instruments will provide. The main advantage of this code compared to other line radiation transfer codes is faster convergence and a more flexible model input method for high dimensional models. While this code is not the first to use Delaunay lines for photon transport, it is the first one to solve molecular excitation and level population on random triangulated grids.

References

Barber, C. B., Dobkin, D. P., & Huhdanpaa, H. 1996, ACM Trans. Math. Softw., 22, 469

Cox, D. P. & Gómez, G. C. 2002, ApJS, 142, 261

Fukagawa, M., Hayashi, M., Tamura, M., et al. 2004, ApJ, 605, L53

Hogerheijde, M. R. & van der Tak, F. F. S. 2000, A&A, 362, 697

Pavlyuchenkov, Y. N. & Shustov, B. M. 2004, Astronomy Reports, 48, 315

Ritzerveld, J. & Icke, V. 2006, Phys. Rev. E, 74, 026704

Nederlandse samenvatting

Stervorming

Dit proefschrift gaat over de beweging van moleculair gas tijdens de verschillende fasen van stervorming. Sterren vormen uit donkere nevels, gigantische interstellaire wolken die bestaan uit gas en stof. Deze wolken bevatten genoeg materiaal voor honderden, soms wel duizenden sterren. Soms wordt een gebied in een van deze wolken onstabiel en de zwaartekracht zorgt ervoor dat het gas en stof samentrekken. Dit is de eerste fase van stervorming. Figuur 8.1 toont een illustratie van een gebied van een interstellaire wolk (paneel a) dat instort onder de zwaartekracht (paneel b). Als het gas instort, wordt de dichtheid een miljoenkeer hoger en uiteindelijk wordt de dichtheid hoog genoeg dat een ster ontstaat. Niet al het gas eindigt in de ster. Het gas draagt, als het in de wolk zit, een hoeveelheid impulsmoment, omdat de wolk langzaam roteert. Elke interstellaire wolk roteert, al is het slechts zeer lichtjes, en deze rotatie wordt overgebracht op het instortende gas. Als het gas instort, wordt de afmeting van de baan kleiner en de rotatiesnelheid groter. Dit resulteert in een middelpuntvliedende kracht in het vlak van de rotatie. Loodrecht op dit vlak is geen middelpuntvliedende kracht en daarom stort het gas in in deze richting sneller in. Door deze asymmetrie wordt een roterende schijf gevormd (Fig. 8.1, paneel c en d). Dit wordt een protoplanetaire schijf genoemd. De protoplanetaire schijf wordt verwarmd door de onlangs gevormde ster en chemische reacties tussen de moleculen beginnen. Ondertussen begint het stof samen te klonteren en grotere deeltjes worden gevormd, zoals kleine stenen en rotsen. Dit is het eerste stadium van planeetvorming, en wanneer de stenen groeien, helpt de zwaartekracht om meer stof en ook gas te verzamelen. Na ongeveer een miljoen jaar vervaagt de schijf en blijft een planeetsysteem achter. De vragen die in dit proefschrift worden behandeld, gaan over hoe het gas wordt vervoerd van de wolk naar de schijf en op welke tijdschaal dit gebeurt.
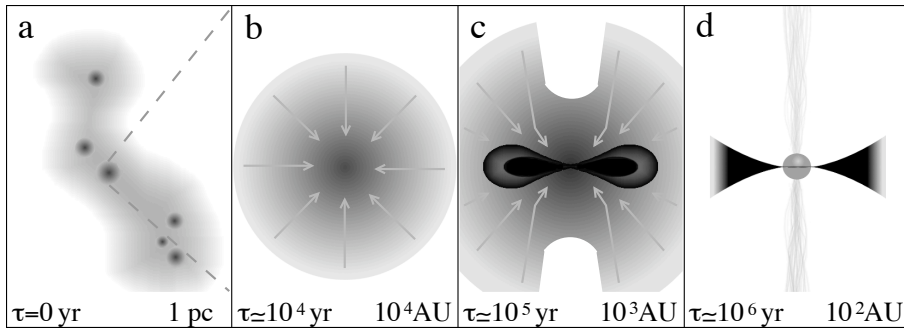
Figure 8.1: Een illustratie van stervorming. De panelen worden beschreven in de tekst. De tijdschaal en grootteschaal is aangegeven in elk paneel. 1 AU = 1 Astronomische eenheid = 1 maal de afstand tussen de aarde en de zon $\approx 1.5 \times 10^{11}$ meter. 1 pc = 1 parsec $\approx 10^5$ AU.

De kinematica van het gas rond protosterren

In het beeld beschreven zoals hierboven, begint het gas op een baan naar het centrum en eindigt het op een cirkelbaan vergelijkbaar met planeetbanen. Niet al het gas eindigt in de schijf; een deel wordt opgenomen in de ster. Dit betekent dat als de wolk instort, de massa van de ster groter wordt. Dit gebeurt op dezelfde tijdschaal als de vorming van de schijf en het snelheidsveld verandert van invallend naar roterend. Een hydrodynamische simulatie van stervorming voorspelt de ontwikkeling van de stermassa en de gemiddelde richting van de gasstroom van een typische protoster (Figur 8.2). Als deze simulatie stervorming goed beschrijft, dan kan de leeftijd van de protoster worden afgeleid door de massa en het snelheidsveld te meten.

Het probleem is, dat het niet mogelijk is om de stermassa en het snelheidsveld direct te meten. Deze grootheden, echter, beïnvloeden de vorm van de profielen van de emissielijnen van de gasmoleculen. Door een wiskundig model te bouwen kunnen lijnprofielen van dit model worden berekend en kunnen deze worden vergeleken met waarnemingen. Als zij overeenkomen, is het model waarschijnlijk goed. Op deze manier kan kennis over de kinematische eigenschappen van protosterren en hun schijven en omhulsels worden verkregen en daardoor het is mogelijk om hen in een evolutionaire context te plaatsen.
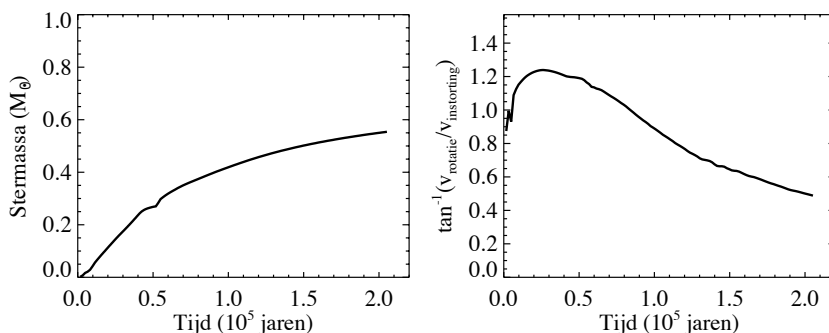
Figure 8.2: In het linker paneel wordt de stermassa als functie van tijd getoond. Het rechter paneel toont de samenstelling van het snelheidsveld als functie van tijd. Beide panelen tonen resultaten van een hydrodynamische simulatie van stervorming.

Dit proefschrift

Na een korte inleiding in hoofdstuk 1, beschrijft hoofdstuk 2 een model dat van de jonge ster L1489 IRS is ontwikkeld. Het model bestaat uit eenvoudige parametrisatie van de moleculaire dichtheid, de temperatuur en de snelheid. De nieuwe twee-parameter-beschrijving van de snelheid, die in dit hoofdstuk geïntroduceerd wordt, wordt ook gebruikt in de hoofdstukken 3–5. Het model wordt vergeleken met waarnemingen van de James Clerk Maxwell Telescope en het Onsala Space Observatory en parameterwaarden van het beste model worden verkregen. Deze parameters beschrijven een gasomhulsel dat is afgeplat en veel rotatie heeft. Deze hoge rotatiesnelheid suggereert dat een protoplanetaire schijf zich in het omhulsel bevindt die niet direct wordt waargenomen.

Hoofdstuk 3 is een theoretische evaluatie van het snelheidsmodel dat in hoofdstuk 2 is geïntroduceerd. Het doel is het model tegen een bekende snelheidsverdeling te testen en een maat te geven voor de beschrijving van het daadwerkelijke snelheidsveld van een jonge ster door de beste reproductie van de data. In dit hoofdstuk wordt een hydrodynamische simulatie van ster- en schijfvorming gebruikt en deze simulatie levert een tijdopgelost snelheidsveld en temperatuur- en dichtheidsverdeling. Waarnemingen worden samengevoegd en gemodelleerd met ons snelheidsmodel en het resultaat is een bijna lineaire evolutie in de parameters die als een kinematische klok kan worden.

In hoofdstuk 4 keren wij terug naar L1489 IRS, waarin nieuwe waarnemingen van de Submillimeter Array worden besproken. Deze waarnemingen zijn gedaan met hoge resolutie waardoor meer detail zichtbaar wordt. Vervolgens worden zij vergeleken met een nieuw model dat een protoplanetaire schijf binnen het gasomhulsel heeft. Daarnaast worden ook infra-rood waarnemingen gebruikt voor de vergelijking. Het verrassende resultaat van dit hoofdstuk is dat de schijf een andere rotatie-as heeft dan het omhulsel en dit betekent dat de schijf dynamisch verschillend van het omhulsel moet zijn.

Hoofdstuk 5 is nog een studie van de hydrodynamische simulatie van hoofdstuk 3. Als het gas ineenstort onder de zwaartekracht, veranderen de temperatuur en de dichtheid en kunnen de moleculen als ijslagen op het stof bevriezen. Als de moleculen vastgevroren zijn, wordt er geen straling uitgezonden en daarom is het belangrijk om deze gebieden te kennen. Wij gebruiken onze hydrodynamische simulatie om koolstofmonoxide te volgen en wij berekenen spectra om het effect van deze zogenaamde "freeze-out" te zien.

Hoofdstuk 6 is een studie van een andere jonge ster, NGC1333–IRAS2A. Net als in hoofdstuk 2 en 4 bouwen we een model op basis van de snelheidsbeschrijving van hoofdstuk 3, maar deze keer introduceren we het "freeze-out" model zoals in hoofdstuk 5 werd besproken. IRAS2A is een echte jonge protoster en in tegengesteling tot L1489 IRS heeft het geen rotatie, maar alleen beweging naar het centrum. Dit komt overeen met de belangrijkste stelling van dit proefschrift, dat als protosterren evolueren, het snelheidsveld van radiaal naar roterend verandert.

Het laatste hoofdstuk beschrijft een nieuw computerprogramma om stralingstransport te berekenen. Dit programma is ontwikkeld om spectra sneller te berekenen. Deze nieuwe methode zal verder ontwikkeld worden om data van toekomstige telescopen te analyseren en de werkbaarheid van het concept aan te tonen. De belangrijkste verbetering is dat dit stralingstransportprogramma driedimensionale modellen kan berekenen, sneller dan andere stralingstransportprogramma.

Curriculum vitae

I was born on October 13 in the year 1977 on the Copenhagen West-side, where I grew up in the suburb Glostrup. From an early age I was very fascinated by the, at that time, relatively new concept of tabletop computers. Still unaware of science as a possible profession, I was convinced, during most of my childhood, that my future would unfold as a computer programmer, which ironically turned out to be almost true. After finishing primary school in 1993, I attended high-school, the Sankt Annæ Gymnasium in Copenhagen. During my last year in high-school I decided that physics, rater than computer science would be my topic at the university so after I graduated from high-school in 1996, I enrolled the following year at the University of Copenhagen where I studied physics and astronomy at the Niels Bohr Institute. In 2001 I received my bachelors degree (B.Sc) and my master degree (M.Sc) in 2004. At that point, my main interests lay in gravitational physics, cosmology, and relativity theory which led to my master thesis on the topic of the gravitational wave signal from merging supermassive black holes. This thesis was supervised by Prof. Dr. Jens Hjorth.

Later in 2004 I decided to switch topic by going to Leiden University and study star formation and astrochemistry for my Ph.D project under the supervision of Dr. Michiel Hogerheijde. My project in Leiden gave me the opportunity to become a real astronomer as I went to the James Clerk Maxwell Telescope and the Submillimeter Array to carry out observations for the first time. I also got the chance to present my work at international conferences, most notably Protostars and Planets V in Hawaii in 2005. In addition, I have been on several working visits to the Institut d'Astrophysique de Paris and at the Argelander-Institut für Astronomie in Bonn, at which places I have also presented colloquia.

Following my graduation from Leiden University, I will move to the University of Bonn where I will take up a post-doc position under Prof. Dr. Frank Bertoldi for the ALMA Regional Centre node.

Acknowledgements

During the last decade, a surprisingly large number of Danish astronomers have travelled to Leiden to work on Ph.D. projects at the Leiden Observatory. In a way, Leiden University has always been a target of opportunity for Danish scholars and with that in mind, coming to Leiden, and living up to the reputation of my fellow Danish predecessors, was certainly intimidating to me at first. I guess the fact that this book has been finished after four years of work means that I did not fail miserably and I owe this to a number of people who have helped me and supported me throughout this period. For that, I would like to express my gratitude.

In particular, I would like to acknowledge the following persons: My collaborators at the IAP for their hospitality and for providing excellent accommodation in the center of Paris on short notice, Vincent for enthusiastic Mac support, Jes and Suzanne for letting me crash in their guest room on several occasion, Herma and Dave for correcting my Dutch writings, Jesper and Mette-Pernille for letting me crash on their couch and for helping me settle in the beginning, the ever-changing Danish/Swedish enclave for the extravagant biannual lunch parties, and, not least, all my colleagues at the Observatory for a professional, friendly and productive work environment. To my good friend and colleague, Jes Jørgensen: Your e-mail on that spring day in 2004 made me very happy!

Finally, I owe everything to my wife, Tonie, for deciding to come along with me to The Netherlands, leaving friends, family and job behind, and for her endless support of everything that I do – Jeg kunne ikke have gjort det uden dig!